REVIEW

Check for updates

Tailoring interfacial energetics in perovskite/silicon tandem solar cells: the converging roles of self-assembled monolayers and dipolar interlayers

Vidya Sudhakaran Menon and Ananthanarayanan Krishnamoorthy (ID) *

Perovskite/silicon tandem solar cells have emerged as a groundbreaking advancement in photovoltaic technology, presenting a viable route to exceed the efficiency ceiling imposed on conventional single-junction silicon devices. At the heart of this innovation lies the perovskite top cell, whose interfacial properties critically govern tandem performance, influencing carrier extraction, recombination dynamics, and long-term stability. Yet, complex interfacial interactions with charge transport layers often introduce challenges such as defect-induced recombination, energy level misalignment, and environmental degradation. This review surveys recent advances in interface engineering for perovskite top cells, focusing on self-assembled monolayers (SAMs) and dipole-tailored interlayers in both single-junction and tandem configurations. We first establish foundational energy alignment concepts – vacuum level shifts, Fermi level pinning, interfacial dipoles, and band bending to frame the electronic landscape at interfaces. The review then explores strategies including molecular dipole tuning, surface passivation, and chemical bonding modulation. This work uniquely integrates molecular-scale design into device performance and critically compares SAMs and dipolar layers with conventional methods. Finally, we highlight key challenges in scalability, industrial compatibility, and operational durability. By aligning molecular design with practical implementation, this review offers guiding principles for advancing interface chemistry in efficient, stable, and commercially viable tandem solar cells.

Broader context

The extraordinary rise of perovskite solar cells (PSCs) has positioned them as strong contenders for low-cost, high-efficiency photovoltaics. Yet, interfacial instabilities and energy level misalignments continue to hamper their commercial translation. Interface engineering, particularly *via* self-assembled monolayers and dipole-modulating layers, offers a powerful means to tailor interfacial energetics, improve charge extraction, and suppress recombination. This review addresses a critical gap by synthesizing the fundamental concepts and practical implementations of such interfacial strategies across PSC architectures. Beyond cataloguing materials and performance metrics, it deciphers the underlying physical and chemical principles—such as dipole-induced vacuum level shifts and passivation-driven defect mitigation—that govern device behaviour. In doing so, it bridges molecular design with the photovoltaic function. By providing this mechanistic perspective, the review not only informs material selection and device architecture but also charts a coherent path toward scalable, stable, and high-efficiency perovskite photovoltaics. The review is particularly valuable to researchers seeking to rationally design interfacial layers that go beyond empirical trial-and-error approaches.

1. Introduction

Utilizing solar energy is undoubtedly one of the most promising methods for providing the globe with sustainable, clean, and economical energy. Solar photovoltaics (PV) is the most frequently used solar power technology in use today and a top contender for terawatt-scale, carbon-free electricity generation by the middle of the century. With strong policy support, declining levelized costs, and increasing deployment at utility and residential scales, solar PV has emerged as a cornerstone of

Organic and Perovskite Photovoltaics Laboratory (OPPV), Department of Chemistry, SRM Institute of Science and Technology, Kattankulathur, Tamil Nadu, India, 603203. E-mail: ananthak@srmist.edu.in; kananthaz@gmail.com

sustainable energy strategies across the globe.[1] In recent years, the price tag of PV systems has substantially diminished, while installations have proliferated, rendering PV economically competitive with traditional energy sources. With declining prices, wholesale and retail grid parity is anticipated to be achieved in the majority of countries within a few years. Currently, crystalline silicon is unequivocally the leading photovoltaic technology, commanding about 90% of the global market share. It affords leverage over alternative PV systems due to its use of a photoactive absorber that is stable, abundant, non-toxic, and extensively explored. In 1999, Green and colleagues at the University of New South Wales (UNSW) set a milestone by achieving a 25% power conversion efficiency (PCE) for c-Si solar cells, a record that stood until 2014.[2,3] Fast

forward to the present, research cell efficiencies are hovering around 27%, with the latest certified records from LONGi showing 27.3% for silicon heterostructures (HIT) and 27.09% for heterojunction back contact solar cells.[4,5] Given the theoretical limit of 29.4% for crystalline silicon cells, further performance improvements are expected to be minimal. Despite this, the dominant segment of the photovoltaic market remains centered on single-junction silicon solar cells, which, by their nature, face inherent limitations in their ability to convert solar energy into electrical power.

Silicon, with its optical band gap of 1.12 eV, has a cutoff wavelength for light absorption at about 1160 nm – an excellent match for converting solar energy into electricity using a single semiconductor absorber. This band gap aligns closely with the solar spectrum, making silicon an ideal material for PV applications. According to the Shockley–Queisser theory, a semi-infinite silicon solar cell, under ideal conditions and limited only by radiative recombination, can theoretically achieve a maximum conversion efficiency of 33.5% at 25 °C.[6,7] However, silicon due to its indirect band gap exhibits both advantages and challenges. On one hand, radiative recombination is less efficient, which allows photogenerated charge carriers to have longer lifetimes in high-quality materials. On the other hand, Auger recombination – a process where recombination energy is transferred to another charge carrier and lost as heat becomes the primary intrinsic loss mechanism. Also, silicon's indirect band gap results in a lower absorption coefficient, particularly near the band gap, which contributes to intrinsic losses such as transparency to sub-bandgap photons and thermalization losses from high-energy photons.[8] These factors collectively cap its intrinsic efficiency limits at 29.4%, as demonstrated through detailed empirical modelling.[9] Despite this, silicon wafers as thin as 100–150 μm can achieve effective light absorption thanks to innovative optical design strategies.[10] Techniques like rear surface mirrors, antireflection coatings, and surface texturing work together to trap and utilize light, even extending into the infrared region of the solar spectrum. These approaches highlight silicon's adaptability and its continued dominance in photovoltaic technology.

In the last decade, the manufacturing cost of mainstream PV modules has decreased substantially. In utility-scale photovoltaic installations, module costs now account for less than half of the total system expenditure, with the remaining 'balance of system' (BOS) costs largely dependent on the physical footprint of the array rather than its energy yield. Consequently, the most effective strategy to further reduce the levelized cost of electricity (LCOE) is to enhance the power output per unit area – achievable by employing multijunction tandem architectures that combine absorber layers with complementary bandgaps, known as tandem solar cells (TSCs). In TSCs, the incident solar spectrum is shared between two sub-cells connected in series.[11] The top cell uses a photoactive material with a larger bandgap, while the bottom cell employs an absorber with a smaller bandgap. The advantage of this approach lies in the high-bandgap material minimizing thermalization losses, while the lower-bandgap cell efficiently captures unabsorbed light from the top cell, thereby reducing sub-bandgap losses. Crystalline silicon solar cells serve as an optimal low bandgap bottom cell for such TSC architecture owing to its appropriate bandgap of 1.1 eV, elevated open-circuit voltage (V_{OC}) reaching 750 mV, cost-effective production stemming from market prevalence, and excellent efficiency.[12] While first-generation PV technology can serve as a good option for the bottom cell in TSCs, emerging technologies like perovskite solar cells (PSCs) offer the potential for affordable tandem systems with higher efficiency and lower costs. Fig. 1 illustrates the efficiency evolution of perovskite/silicon (c-Si) TSCs over time, highlighting major technological advancements.

In less than ten years, PSCs have transitioned from a laboratory curiosity to a mature photovoltaic technology with demonstrated operational viability, whereas previous PV systems like silicon and organic solar cells (OSCs) took 15–42 years to do so. Perovskite single junctions have verified efficiencies as high as 27.3% (device level; active area <1cm²) whereas tandem configurations with c-Si have achieved

Vidya Sudhakaran Menon

Dr Vidya S. Menon received her PhD in Chemistry from the SRM Institute of Science and Technology, India, where she specialized in the development of inorganic charge transport layers and interface engineering strategies for perovskite solar cells. Her research spans semiconductor physics, surface modification, and energy level alignment, with a strong focus on defect passivation and interfacial energetics in perovskite-based photovoltaics. Dr Menon's interdisciplinary background bridges chemistry, materials science, and device engineering. Her current interests include tandem solar cell architectures and advanced spectroscopic characterization of hybrid materials.

Ananthanarayanan Krishnamoorthy

Dr Ananthanarayanan Krishnamoorthy is currently a Research Associate Professor of Chemistry and the Head of the Organic and Perovskite Photovoltaics group at the SRM Institute of Science and Technology (SRMIST). Previously, he was a Senior Research Scientist and Group Head at the Solar Energy Research Institute of Singapore (SERIS). His research interests include all aspects of the fundamental understanding of photovoltaic devices and upscaling of organic solar cells and perovskite solar cells.
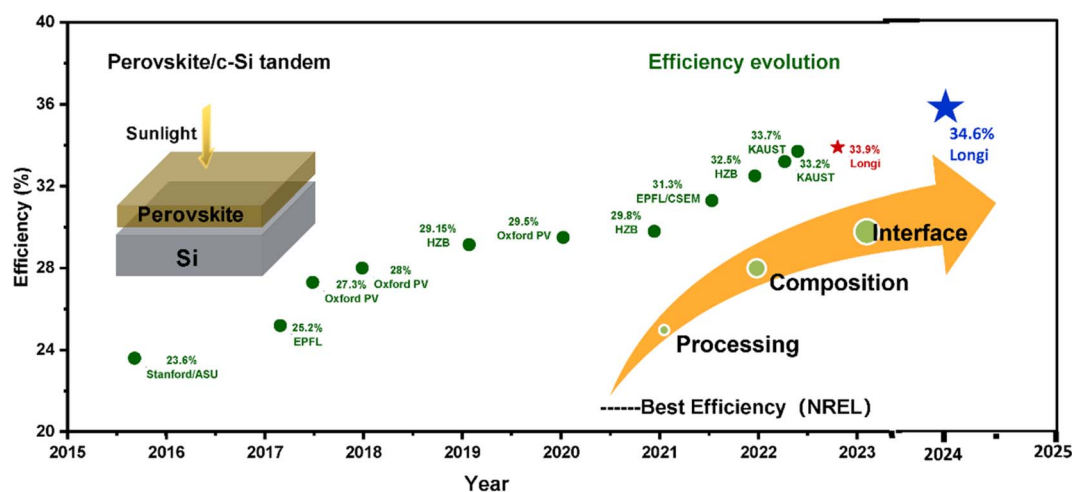
Fig. 1 Efficiency evolution of perovskite/silicon tandem solar cells (2016–2025), highlighting certified PCE milestones from key institutions. The schematic illustrates the tandem architecture, with efficiency gains attributed to advances in processing, composition, and interface engineering. Modified and adapted from ref. 13, under a Creative Commons CC BY 4.0 license.

efficiencies of 34.85% (active area – 1 cm^2) and that with CIGS has reached 24.2% (active area – 1.05 cm^2), demonstrating exceptional potential to advance solar energy technologies.[14] Perovskite photovoltaics have become a focal point of research since their emergence in 2009, when their light-absorbing capabilities were first recognized. These materials have enabled silicon-based solar cells to surpass their single-junction efficiency limits, solidifying their role as ideal candidates for tandem architectures. Perovskites offer a unique combination of properties including high photoconversion efficiencies, sharp optical absorption edges, and a tunable bandgap ranging from 1.4 to 2.3 eV making them especially suited for integration as top cells.[8,15] Their ability to be processed at low temperatures (100–150 °C) from inexpensive, earth-abundant precursors further enhances compatibility with silicon bottom cells and large-scale manufacturing. Moreover, perovskites display notable defect tolerance, long carrier diffusion lengths, and the potential for photon recycling, collectively supporting their rapid evolution toward commercial viability.[16]

The exceptional performance of perovskites as light-absorbing layers, however, relies heavily on the dynamics at their interfaces, which serve as critical junctures for charge separation, transport, and collection. Unlike organic semiconductors, where exciton-dominated recombination dynamics prevail, perovskites operate under the free-carrier model, resembling heterojunction solar cells.[17] When two semiconductors form direct contact, free carriers diffuse across the interface, aligning the Fermi levels and creating a charge-depletion region with an inherent electric field. This electric field, disrupted by photon absorption, drives charge extraction and transport processes. However, the success of this mechanism is highly contingent on interfacial quality. Photoinduced carriers must traverse these interfaces, which are prone to recombination losses due to defects and unfavorable charge distributions. In planar p–i–n PSCs, for instance, charge

extraction occurs at the perovskite/ETL (ETL: electron transport layer) and HTL/perovskite (HTL: hole transport layer) interfaces, making these regions particularly susceptible to efficiency losses. The complexity of the device escalates with the number of interfaces, especially in the case of multijunction photovoltaic devices. This establishes strict criteria for interface design and the evaluation of their characteristics. In thin-film photovoltaic devices, non-radiative recombination of charge carriers predominantly facilitated by defect states constitutes the
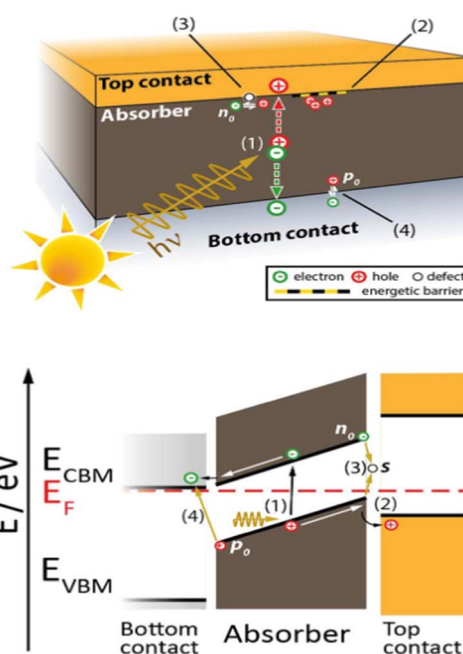

Fig. 2 Schematic illustration of interface-related loss mechanisms in a simplified photovoltaic device. Reproduced with permission from ref. 18, Copyright © 2018, American Chemical Society.

primary loss mechanism, largely stemming from disruptions in crystal periodicity at material interfaces as depicted in Fig. 2.

This concept is clearly illustrated by the crystalline quality of the absorber layer in thin-film silicon solar cells. In devices based on c-Si, photogenerated charge carriers exhibit lifetimes on the order of milliseconds much longer than the microsecond-scale time it takes for these carriers to diffuse to the interface with the charge transport layers (CTLs).[19] As a result, bulk recombination is nominal compared to the pronounced recombination occurring at the interfaces, making interfacial properties the primary determinant of device performance. Thus, while advancements in perovskite film quality and device architecture have propelled the performance of perovskite based TSCs to impressive heights, it is clear that interface engineering remains a pivotal, yet underexplored avenue for further optimizing both efficiency and stability of such tandem architectures.

This review offers a distinctive and comprehensive analysis of interface engineering strategies in perovskite/silicon TSCs, addressing the critical challenge of interface stability and reactivity, that often leads to mismatched photocurrents between the perovskite top cell and the silicon bottom cell. In Section 2, we take a step back to explore how these tandem architectures evolved, uncovering the breakthroughs that have shaped their performance so far. Moving into Section 3, we tackle the big question: why is interface engineering such a game-changer for these devices? Here, we break down the unique challenges faced by perovskite top cells that make or break their performance. Section 4 offers a structured journey through the interface landscape: from a broad overview of strategies proven in single-junction PSCs to a focused chronicle of SAMs as interfacial game-changers and ultimately to the energetics of chemically tailored semiconductor surfaces driving next-generation performance. Expanding further, Section 5 dives deeper into the interface engineering toolbox by

dissecting the complementary roles of SAMs and dipole-oriented interlayers and then extends the discussion to real-world tandem architectures unpacking how these molecular layers are being tailored to meet the demands of both all-perovskite tandems and perovskite–silicon hybrids. Building on this, in Section 6, we zoom out to address real-world hurdles, from scaling up these techniques to making them compatible with industrial processes and ensuring long-term stability under stress. Finally, Section 7 synthesizes the conceptual and practical threads woven throughout this review, examining how SAMs and dipole-tailored interlayers despite their transformative promise must evolve beyond their current limitations to meet the demanding realities of scalable, stable tandem photovoltaics. This final section frames SAMs and dipolar layers not just as current enablers of high-efficiency PSCs, but as future molecular platforms poised for reinvention where advanced design tools, hybrid materials, and cross-disciplinary collaboration must converge to overcome the scaling and stability challenges that lie ahead (Fig. 3).

2. Genesis of perovskite/silicon TSCs

The journey of perovskite solar cells (PSCs) began with their roots in dye-sensitized solar cells (DSSCs). In a groundbreaking discovery in 2009, Miyasaka et al. introduced $MAPbX_3$ perovskite as a novel organic–inorganic hybrid semiconductor, achieving an initial power conversion efficiency (PCE) of 3–4% within a liquid-based DSSC framework.[20] This breakthrough paved the way for transformative advancements, including the creation of non-sensitization PSCs by Snaith et al. and the stabilization of perovskites in polar solvents by Park et al., which further propelled the technology forward.[21,22] The remarkable properties of lead halide perovskites, such as their long carrier diffusion lengths and exceptional carrier mobility, redefined device architectures and revolutionized the understanding of PSC operation. These innovations catalysed an unprecedented surge in PCE, now attaining 27.3%, enabled by cost-effective and simple solution processing techniques.[14] This rapid evolution has positioned PSCs as a disruptive force, poised to not only compete with, but potentially surpass existing photovoltaic technologies, capturing widespread interest across the scientific community.

The remarkable optoelectronic properties of halide perovskites, rooted in the precise energy level alignment of their valence and conduction bands, have been a key driving force behind the intense interest they have generated within the scientific community. In a typical lead iodide-based perovskite, the electronic energy levels originate from the hybridization of lead (Pb) 6p and 6s orbitals with the 5p and 5s orbitals of iodine (I). Due to the alignment of the crystal momentum vectors of the valence band (VB) and conduction band (CB), and with the Fermi level positioned between the VB maximum and CB minimum, lead halide perovskites exhibit the characteristics of a direct band gap, non-degenerate semiconductor. The valence band maximum (VBM) is primarily influenced by halogen p-states, while the conduction band minimum (CBM) is primarily governed by lead p-orbitals. Such alignment of energy
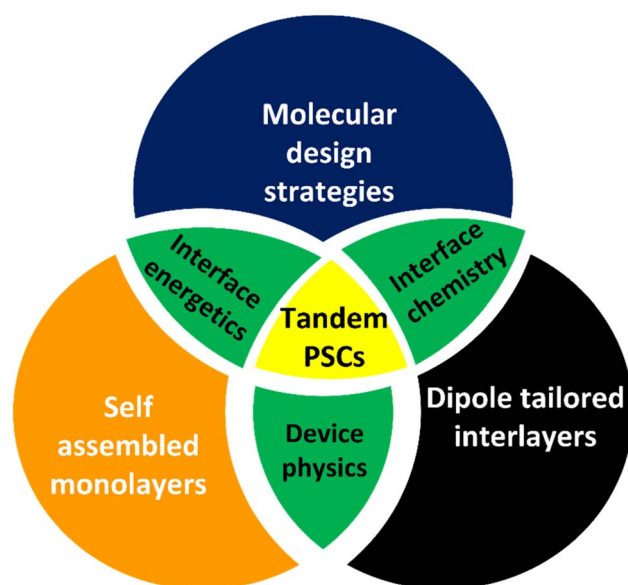

Fig. 3 Highlights of the principal topics examined in this review.

levels in perovskite allows for a direct band gap p–p electronic transition, resulting in an impressive optical absorption coefficient of approximately 10^5 cm^{-1}. In 2014, De Wolf *et al.* utilized photocurrent spectroscopy to reveal that perovskites, unlike other widely used photovoltaic materials such as GaAs, CdTe, and CIGS, exhibit a sharp optical absorption edge, a high absorption coefficient, and minimal sub-bandgap absorption.[8] Remarkably, CH$_3$NH$_3$PbI$_3$ demonstrated an Urbach energy on par with monocrystalline direct-bandgap semiconductors like GaAs, renowned for their exceptional electrical quality. In contrast, crystalline silicon (c-Si) shares a similar absorption spectrum pattern but, due to its indirect bandgap, requires phonon assistance for photon absorption. This leads to a markedly lower absorption coefficient and limits its efficiency. As a result, while perovskite layers of only a few nanometres of thickness can absorb photons effectively, silicon requires wafer thicknesses in the micrometre range to achieve the same level of absorption, highlighting the superior photon harvesting capabilities of perovskites. Consequently, perovskite materials swiftly sparked considerable interest for their potential in multijunction solar cells, captivating researchers and industry experts alike with their unique properties and promising ability to enhance the efficiency of solar energy conversion. Fig. 4 provides a schematic representation of molecular orbital energy levels of prototypical MAPbI$_3$ perovskite and a comparison of its absorption coefficients with that of various light absorbers.

In their pioneering paper, Miyasaka[20] and his team had already demonstrated that perovskites possess high bandgaps, excellent photovoltage, and tunable bandgaps ranging from 1.5 to 2.1 eV. Subsequent advancements in planar thin-film solid-state architectures, along with the adoption of vacuum-based deposition methods, reinforced the promise of perovskite technology as a viable complement to silicon in cost-effective

TSCs. At the close of 2014, the first reports of semi-transparent PSCs and mechanically stacked tandem cells emerged, with Löper *et al.* and Bailie *et al.* demonstrating impressive efficiencies of 13.4% and 17% for 4T tandems, respectively.[24,25] Löper and his team initially used sputtered indium tin oxide (ITO) for the transparent electrode, but its suboptimal properties, due to high-temperature treatment, hindered the perovskite layer. They later resolved this by using indium zinc oxide (IZO), which can be used as-deposited, offering high carrier mobility and low sheet resistance. Meanwhile, Bailie *et al.* used silver nanowire mesh transferred onto the perovskite stack, achieving high transparency and low sheet resistance, though the mechanical transfer process still posed reproducibility challenges. Shortly thereafter, Bailie's team collaborated with Buonassisi and co-workers to create the first perovskite/Si monolithic TSC, using the same silver nanowire electrode.[26] By combining a mesoscopic perovskite top cell with a Si homojunction bottom cell and a silicon tunnel junction, they achieved a 13.7% efficient tandem, although the performance was limited by parasitic absorption in the CTLs, resulting in a modest V_{OC} of 1.58 V.

In late 2015, Albrecht *et al.* achieved a milestone by utilizing a Si-heterojunction as the bottom sub-cell in a monolithic tandem architecture, achieving a notable PCE of 18.1%.[27] This success was driven by the cell's strong near-infrared response and high voltage output of 1.78 V. Additionally, they pioneered the use of a low-temperature planar PSC, featuring an atomic layer deposited (ALD) SnO$_2$ electron transport layer (ETL). Heterojunction Si cells have since become the go-to choice for bottom cells in laboratory experiments, largely because of the accessibility of indium tin oxide (ITO) for seamless integration with top and bottom cells, combined with their proven ability to deliver high open-circuit voltages and impressive efficiency. Few
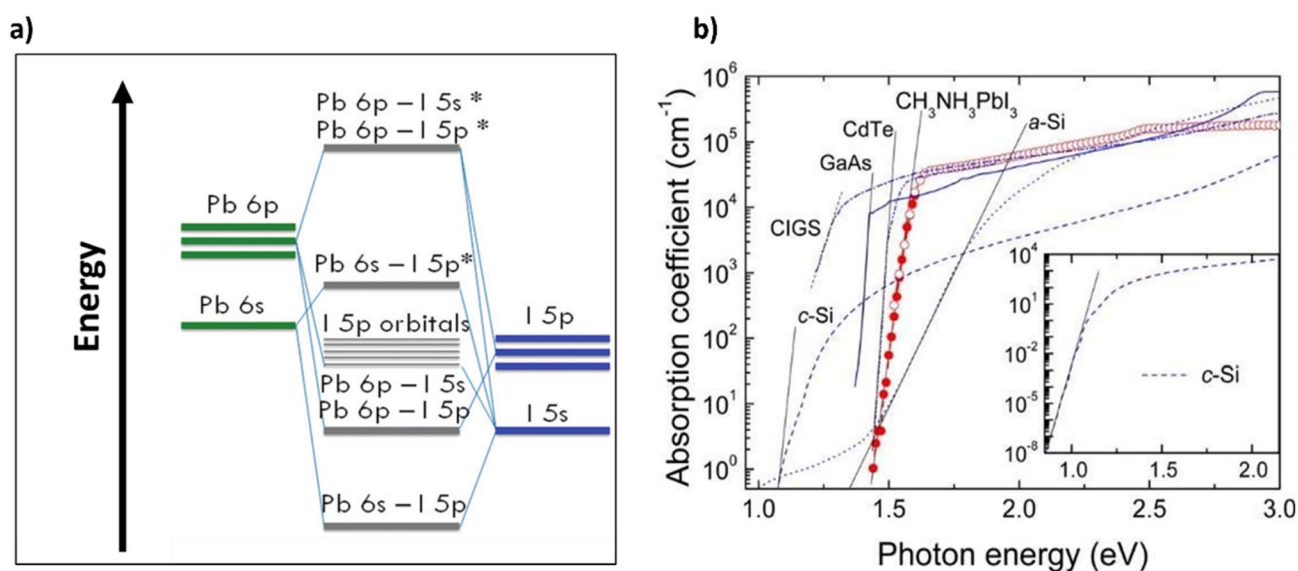

Fig. 4 (a) Schematic depiction of the molecular orbital energy levels of MAPbI$_3$ perovskite; reproduced with permission from ref. 23 Copyright 2015, Royal Society of Chemistry; (b) absorption coefficient comparison between MAPbI$_3$ and other representative light-harvesting materials. Reproduced with permission from ref. 8 Copyright 2014, American Chemical Society.

months apart, Werner *et al.* raised the monolithic tandem efficiency to 21.2% by incorporating a PC fullerene-based planar perovskite top cell and an IZO recombination layer.[28] However, the bottom cell current was limited due to the use of a double-sided polished silicon wafer. In August 2016, the same group addressed this limitation by introducing rear-side textured silicon wafers, leading to a 20.5% efficiency on a 1.4 cm² monolithic tandem cell, a notable improvement over previous devices with smaller areas of less than 0.3 cm².[29] Fig. 5 depicts the layer architecture and material choices in n–i–p and p–i–n perovskite/silicon tandems, highlighting interface strategies and bottom cell variations.

While the photovoltaic community focused on optimizing c-Si solar cells to enhance tandem efficiency, material chemists shifted their attention onto emerging perovskite materials. Unlike c-Si, perovskites offer a distinct advantage – their optical bandgap can be precisely modulated through compositional engineering, enabling optimal band alignment for high-efficiency tandem photovoltaic applications. Such tunability of the band gap in perovskite materials arises from modifications in the density of states (DOS), which are affected by changes in the X–Pb–X bond geometry and dimensions resulting from the

inclusion of various cations and anions.[31] Notably, the A-site cation in the ABX_3 perovskite structure does not directly impact the band gap. Instead, the band gap is primarily determined by interactions between the s and p orbitals of the B-site cation and the p orbitals of the halide anions. Additionally, the absolute energy of the halide p orbitals plays a critical role; higher p orbital energy levels elevate the VBM and reduce the band gap. Furthermore, stronger orbital overlap between metal cations and halide anions (I, Br, Cl, and F) leads to a narrower band gap.[32–34]

Methylammonium lead iodide ($MAPbI_3$) was the most widely adopted perovskite composition, possessing a bandgap of approximately 1.55 eV, which falls short of the optimal 1.73 eV bandgap required for the top cell in monolithic silicon-based tandem configurations. While $MAPbI_3$-based top cells were effective in early proof-of-concept tandem devices, surpassing the efficiency limit of single-junction silicon cells particularly in monolithic tandem architectures necessitated top cells with a bandgap elevated by roughly 0.2 eV. Building on this understanding, various strategies were explored to modulate the perovskite band gap, with halide composition engineering emerging as one of the most effective approaches. Mixed halide
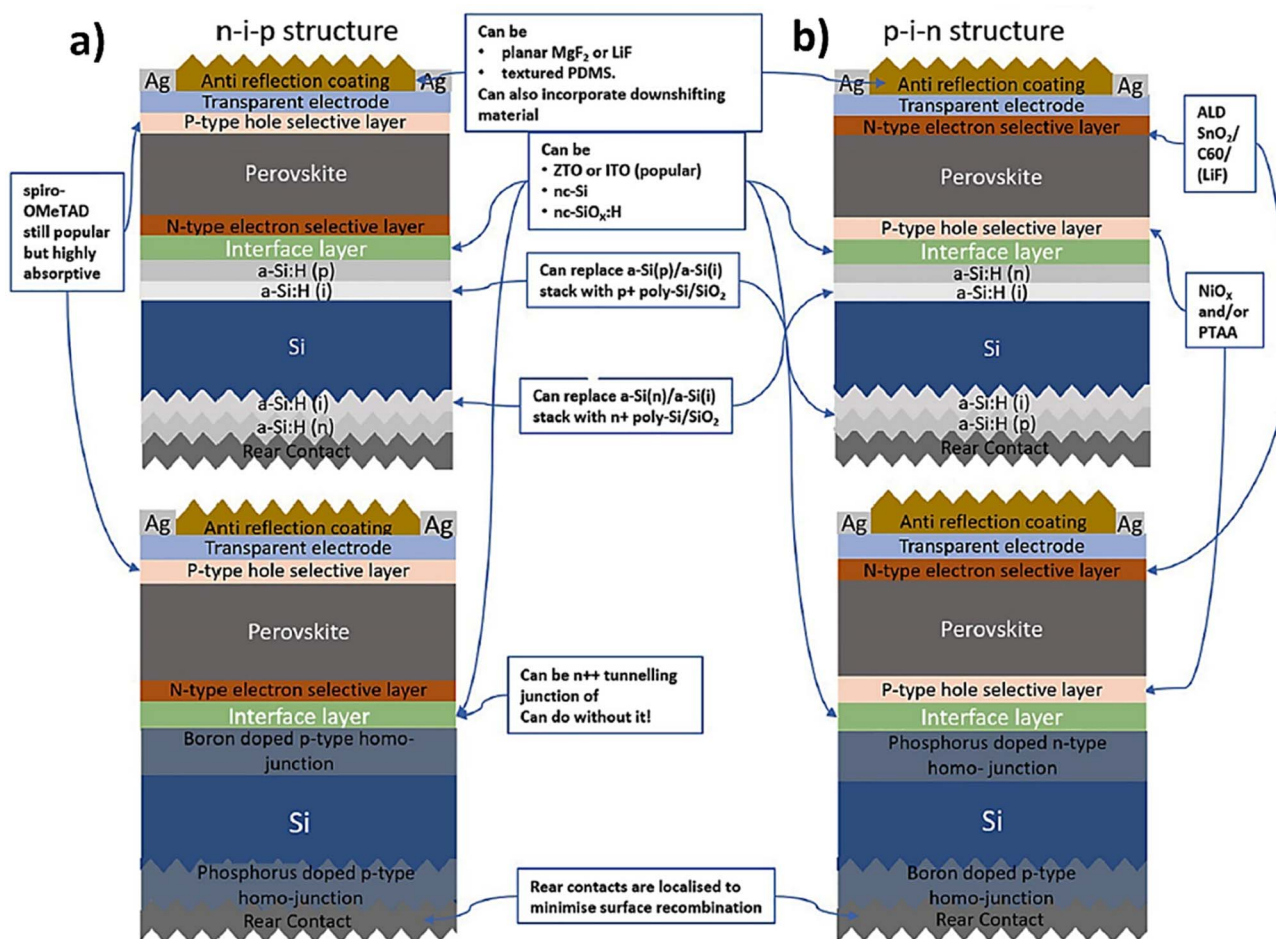

Fig. 5 Structural comparison of (a) n–i–p and (b) p–i–n perovskite/Si tandem cell architectures, highlighting the distinction between homo-junction and heterojunction Si bottom cells. Reproduced from ref. 30 under a Creative Commons CC BY 4.0 license.

perovskites, particularly I/Br compositions, were widely employed in tandem solar cells to achieve an optimal band gap for efficient charge extraction. These mixed I/Br perovskites exhibited higher charge-carrier mobility (exceeding ~1 cm^2 V^{-1} s^{-1}) compared to pure iodide-based counterparts.[11] Additionally, an increased bromide content enhanced the perovskite's stability against degradation under high ambient humidity, further improving their viability for photovoltaic applications.[35] However, the inherent instability of mixed-halide perovskites remains a critical limitation, as these materials undergo photoinduced phase segregation, compromising their long-term performance.

A noteworthy breakthrough in enhancing phase stability was achieved by incorporating cesium (Cs) and formamidinium (FA) cations, by either partially or fully substituting methylammonium (MA). McMeekin et al. demonstrated that a Cs–FA double-cation perovskite could achieve a bandgap of approximately 1.74 eV, making it an ideal candidate for top-cell absorbers in tandem configurations.[36] Notably, perovskite compositions such as $FA_{0.83}Cs_{0.17}Pb(I_{0.6}Br_{0.4})_3$ with a 1.74 eV bandgap have yielded solar cells with efficiencies reaching 17%, alongside a V_{OC} of 1.2 V, nearing the theoretical maximum of 1.42 V. Unger et al. conducted a comparative analysis of reported data on PSCs with bandgaps ranging from 1.2 to 2.2 eV and observed that the measured V_{OC} generally displayed a monotonic bandgap increase up to approximately 1.7 eV as shown in Fig. 6.[37] However, for bandgaps exceeding this threshold, considerable deviations were noted, which were attributed to light-induced phase separation, also known as the Hoke effect, leading to a reduction in V_{OC}.

The loss in V_{OC} relative to the bandgap consists of two primary components: (i) radiative losses, which arise from unavoidable radiative recombination of free charge carriers, governed by the Shockley–Queisser (SQ) limit and (ii) non-radiative losses, primarily caused by trap-assisted recombination occurring both in the perovskite bulk and at internal interfaces.[38] While the SQ limit defines the theoretical maximum V_{OC} for a given bandgap, non-radiative recombination reduces the experimentally measured V_{OC}, often substantially below this limit.[39] It is generally observed that the highest PCEs, above 20%, are achieved only when V_{OC} remains close to the SQ limit, with PCEs exceeding 22% primarily observed in $FAPbI_3$ based compositions possessing bandgaps of approximately 1.5 eV or lower.[40] However, for bandgaps optimized for tandem top-cell applications, reported V_{OC} values remain well below 90% of the SQ limit, indicating relatively greater voltage losses compared to other bandgap compositions. This poses a fundamental limitation for perovskite-based tandem solar cells. To mitigate these non-radiative losses and enhance V_{OC}, further optimization of perovskite compositions is essential.

Additionally, charge-selective layers must be carefully tuned to ensure proper energy level alignment with these optimized perovskites, further minimizing recombination losses and improving overall tandem device performance. An increase in the bandgap generally results in an upward shift of the conduction band energy. Consequently, Lin et al. demonstrated that optimizing the energy level alignment of the ETL effectively enhances the V_{OC} leading to improved device performance. By implementing such modifications, PSCs with a bandgap of 1.71 eV achieved PCEs of up to 18.5%.[41] While energy level alignment within the perovskite absorber and CTLs plays a crucial role in improving V_{OC}, tandem device performance also heavily depends on mitigating optical and electrical losses at the interface between the perovskite top cell and the silicon bottom cell. The nascent phase of perovskite/Si tandem research saw much attention being focussed on developing efficient interfacial layers (ILs) between the perovskite top cell and silicon bottom cell to mitigate the critical issue of parasitic absorption and other optical losses. Initial studies zeroed in on fine-tuning the thickness of the ITO interfacial layer, shifting
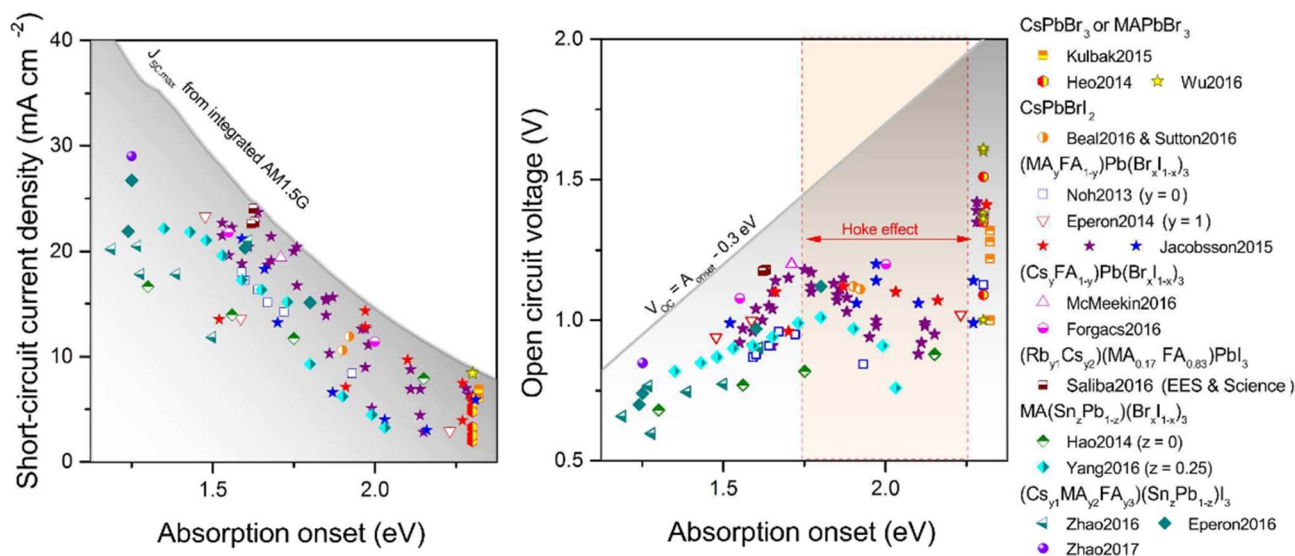

Fig. 6 Experimental J_{SC} values as a function of the perovskite absorber bandgap (E_g) benchmarked against the theoretical radiative limit (left). Correlation between V_{OC} and E_g (right). Reproduced with permission from ref. 37 Copyright 2017, Royal Society of Chemistry.

from the previously common 40–120 nm range down to a much slimmer 10–20 nm range for better performance.[42–45] Alternative ILs such as nanocrystalline SiO_2, Si and zinc tin oxide proved to be not only effective but, in some cases, even superior in terms of their optical performance. Later on, Zheng *et al.* and Shen *et al.* made breakthroughs by showing that transparent conductive oxides (TCOs) like ITO are not essential for connecting the top and bottom cells in perovskite–Si homojunction tandems.[46,47] Their research demonstrated that solution-processed SnO_2 and TiO_2, when deposited *via* ALD, can effectively serve as ETLs for the perovskite top cell and recombination layers at the perovskite–Si interface. In fact, Zheng *et al.* found that their TCO-free tandem designs are ideal for large-area cells, exhibiting a tightly controlled fill factor distribution.[47] This is attributed to the reduced lateral conductivity of the SnO_2 layer, which minimizes unwanted shunting effects that would otherwise typically occur when using TCOs.

While the quest for efficient ILs was ongoing, parallel studies were also being carried out to optimise the ideal architecture of the perovskite top cell. The n–i–p configuration emerged as the preferred architecture in the early stages of tandem cell development. This structure was based on the well-established fabrication process for PSCs, where an ETL (*e.g.*, TiO_2 or SnO_2) was applied first, followed by the deposition of HTLs, such as spiro-OMeTAD, after the perovskite layer. However, spiro-OMeTAD introduced challenges due to its high parasitic absorption. Furthermore, the use of MoO_3, which was necessary to protect both spiro-OMeTAD and the layers beneath it from sputtering during the deposition of the top TCO, led to Fresnel reflection and subsequent optical losses.[47] To address this, efforts were made to replace the spiro-OMeTAD layer with a less absorptive alternative, but progress in this area remained limited. Consequently, attention shifted to the inverted planar configuration (p–i–n), which not only overcame the drawbacks of the conventional planar structure but also offered inherent advantages, such as ease of fabrication and compatibility with low temperature processing, offering remarkable potential for tandem PV applications. In 2017, Bush *et al.* reported the first tandem cell with inverted planar configuration, achieving a notable J_{SC} of 18.1 mA cm^{-2} and a certified efficiency of 23.6%.[48] In such devices, the HTL, which is deposited prior to the perovskite absorber, typically consisted of materials like NiO_x or poly[bis(4-phenyl)(2,4,6-trimethylphenyl)-amine] (PTAA) while the ETL, positioned above the perovskite absorber, generally included components such as $(LiF)/C_{60}$ or ALD SnO_2.[49–53]

These remarkable strides made in compositional engineering, interface optimization, and device architecture have collectively propelled perovskite–silicon tandem solar cells toward unprecedented efficiencies. However, despite these advancements, achieving further performance improvements and long-term operational stability remains closely tied to the meticulous design and control of interfaces within the perovskite top cell. These interfacial issues, particularly those related to energy level alignment, defect passivation, and charge extraction, have emerged as critical bottlenecks. A focused exploration of these interface challenges is therefore essential

to realize the next leap in tandem solar cell performance, as discussed in the following section.

3. Interface challenges in perovskite top cells

PSCs have a complex architecture with four key interfaces: perovskite/ETL, perovskite/HTL, ETL/cathode, and HTL/anode as illustrated in Fig. 7. These interfaces, along with interfacial materials, play a crucial role in governing the electronic properties and operational stability of PSCs. Since charge extraction occurs at these interfaces, they are particularly prone to recombination losses due to interfacial defects and charge accumulation.[54] Additionally, factors such as energy barriers, defect states, ion migration within the perovskite and CTLs, and charge accumulation at the perovskite/transport layer interfaces considerably impact charge collection efficiency and contribute to performance instabilities, including hysteresis and the light soaking effect.[55] These interfacial processes directly modulate the built-in potential, either enhancing or limiting the V_{OC} of the device.

Independent of their specific architecture, PSCs contain two primary interfaces between the perovskite absorber and CTLs: the buried interface and the top surface/interface. Additionally, polycrystalline perovskite films, typically obtained *via* solution processing, exhibit considerable structural disorder at grain boundaries, which can be considered a third type of interface.[56] The performance metrics of PSCs, including J_{SC}, FF, and V_{OC}, are strongly influenced by defect-induced recombination occurring either within the bulk or at these interfaces.[57,58] The performance of PSCs, particularly in tandem configurations, is heavily influenced by the quality of the interfaces between the perovskite top cell and the underlying layers, such as the charge transport materials and the silicon bottom cell.[59] As the efficiency of these devices increases, interface-related issues become more pronounced, with charge recombination, parasitic absorption, and energy level misalignment emerging as critical factors that limit device performance. The successful
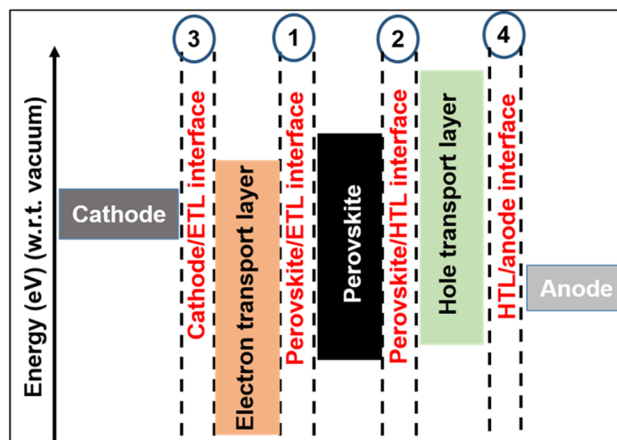
Fig. 7 Interfaces and their corresponding energy level alignment in PSCs.

integration of perovskite top cells in tandem architectures requires not only optimizing the properties of individual materials but also ensuring seamless interactions between them. Hence, a deeper understanding of these interface challenges is essential for enhancing the stability, efficiency, and scalability of perovskite-based tandem solar cells and for overcoming the fundamental barriers that currently hinder their commercial viability.

3.1. Interface recombination: a major challenge in PSCs

3.1.1 Quantitative insights into surface recombination.

A deeper understanding of these interfacial losses necessitates a quantitative approach, particularly through surface recombination models. To better understand this challenge, the surface recombination current J_S of electrons at a hole contact is expressed as

$$J_S = qSn_0 e^{\frac{\Delta E_F}{k_B}} T \qquad (1)$$

where q is the electron charge, S is the surface recombination velocity, n_0 is the equilibrium electron density at the hole contact, ΔE_F is the quasi-Fermi level splitting, and $k_B T$ is the thermal energy.[60] This equation highlights how J_S scales with the surface recombination velocity and the charge carrier density at the interface. The surface recombination velocity (S) is dictated by the density of surface defects, which serve as recombination centers, while n_0 depends on the built-in electric field and the potential drop at the electrodes. A stronger built-in field reduces n_0, thereby lowering the recombination current. This relationship underscores the critical role of interface engineering in minimizing recombination losses. By designing defect-free interfaces and optimizing band alignment to enhance the built-in field, the recombination current can be reduced, markedly improving the efficiency and performance of thin-film photovoltaic devices.

While interfacial recombination is a key limitation in single-junction PSCs, tandem architectures present an even greater challenge due to the presence of multiple stacked interfaces. In such systems, efficient charge transport demands precise interface engineering across both the perovskite top cell and the underlying bottom sub-cell, making interfacial design even more critical. Any mismatch in energy level alignment, charge extraction inefficiencies, or interfacial defects can severely impact V_{OC} and overall PCE.[61] Therefore, optimizing these interfaces *via* efficient defect passivation strategies is paramount to minimizing non-radiative recombination losses, ensuring efficient carrier transport, and stabilizing device performance under operational conditions. As tandem architectures continue to evolve, it becomes increasingly evident that managing interfacial quality is not merely advantageous but essential for unlocking their full potential. A deep understanding of the nature, origin, and behavior of defects at perovskite interfaces is crucial for devising effective passivation strategies. In this context, investigating the types and dynamics of defect formation at perovskite interfaces provides valuable insights into mitigating recombination losses and enhancing device efficiency. The following section delves into the mechanisms of defect formation at these critical interfaces.

3.1.2 Defect mediated recombination at the interface.

While p–i–n PSCs offer advantages in terms of fabrication flexibility, achieving optimal device performance in this architecture remained a considerable challenge when compared to their n–i–p planar counterparts. The underwhelming PCEs of inverted PSCs can largely be blamed on non-radiative recombination of photogenerated charge carriers – a persistent issue that has resisted numerous solutions. Fundamentally, a solar cell's photo-voltage hinges on the separation of electron (E_{Fn}) and hole (E_{Fp}) quasi-Fermi levels within the photoactive layer, which, in turn, depends on the charge carrier density and bandgap of the absorber.[62] Non-radiative recombination disrupts this delicate balance, undermining charge buildup and dragging down the device's photo-voltage. Adding to the challenge are crystallographic defects like point defects and grain boundaries at the surface and interfaces, which serve as prime culprits for these undesirable recombination processes. Beyond limiting photo-voltage, these defect sites also accelerate device degradation, making them easy targets for environmental factors to initiate damage.[63] In addition to this, trap states located at the surface and interfaces of perovskite can result in the build-up of charges and losses in the device due to recombination. The presence of trapped charge carriers introduces extra non-radiative recombination pathways, leading to a noticeable drop in the overall efficiency of the device, especially in the V_{OC} of solar cells.[64] Fig. 8 illustrates the various recombination pathways commonly observed in photovoltaic devices.

That said, it is imperative to note that perovskites are a class of defect tolerant semiconductors unlike conventional semiconductors like Si or GaAs. The majority of defects present in them are shallow defect states closer to the band edges and therefore are benign in nature. Hence, rather than the bulk, it is critical that the attention be focussed on the interface between the perovskite absorber and the adjacent CTLs.[66] These interfaces often dictate overall device quality, serving as the decisive factor that separates high-performing devices from their less efficient counterparts. The following section delves into the mechanisms of defect formation at these critical interfaces.

3.1.3 Defect formation at perovskite interfaces.

Interface defects are particularly susceptible to formation during crystal growth and post-treatment processes, making their passivation a key focus for improving PSC performance. In an ideal perovskite crystal, atomic positions remain fixed; however, under practical conditions, deviations arise due to processing variations, leading to defect formation.[67] Four major categories of interfacial defects have been identified as major contributors to non-radiative recombination:

(i) intrinsic point defects, including antisite, vacancy, and interstitial defects, which introduce transition levels within the bandgap and contribute to shallow-level recombination when located near the valence or conduction band;[68]

(ii) two-dimensional (2D) extended defects, such as grain boundaries and surface defects;
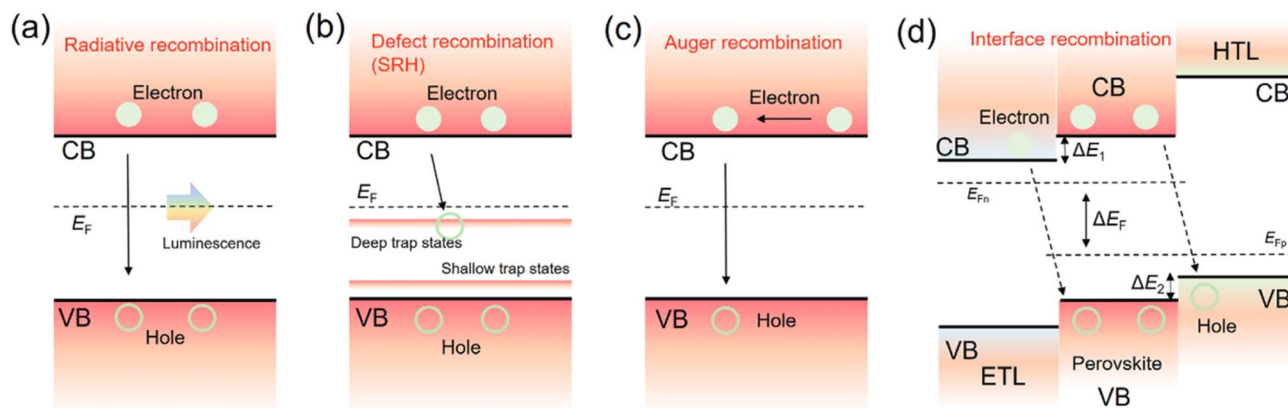
Fig. 8 Overview of key carrier recombination pathways in solar cells: (a) radiative recombination, (b) Shockley–Read–Hall (defect-mediated) recombination, (c) Auger recombination, and (d) interface recombination. Reproduced with permission from ref. 65, Copyright 2023 Wiley-VCH GmbH.

(iii) three-dimensional (3D) defects, including lead clusters; and

(iv) highly mobile charged point defects, which, due to the ionic nature of perovskites, can migrate to interfaces under an electric field, affecting photovoltaic performance and long-term stability.[64]

Fig. 9 illustrates the common structural defects observed in perovskite materials, including vacancies, interstitials, anti-site defects, and grain boundaries, shown relative to the ideal crystal lattice.

Thermal degradation and non-stoichiometry-related defects are frequently identified as the primary sources of charge traps in PSCs. Methylammonium lead iodide films have been observed to decompose at temperatures as low as 105–150 °C, leading to the formation of undercoordinated halide vacancies and Pb^{2+} defect states. These defects, existing as dangling bonds, serve as dominant charge trap sites, particularly at the absorber/CTL interfaces. Under forward bias, these traps become occupied, whereas under short-circuit conditions, they discharge further, modifying the interfacial band structure. Consequently, a depletion region forms at the ETL/perovskite and HTL/perovskite junctions, impeding efficient charge extraction and thereby limiting photovoltaic efficiency, particularly under a forward scan.[66]
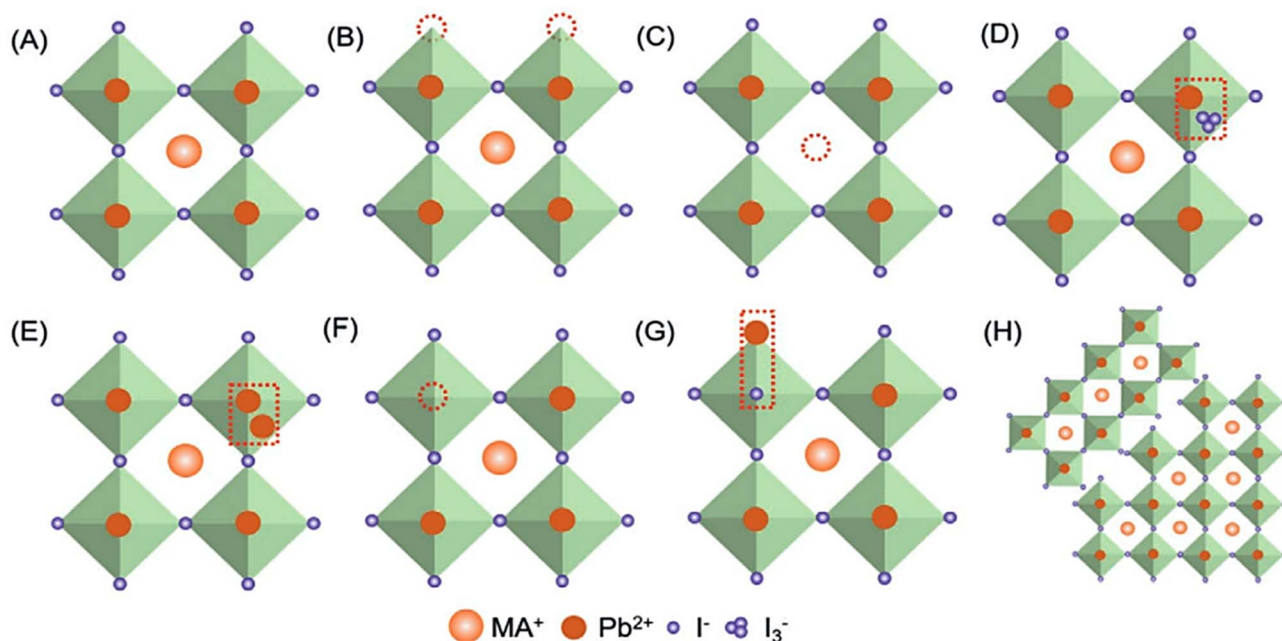

Fig. 9 Representative defect types in perovskite solar cells. (A) Ideal crystal structure, (B) iodide vacancy, (C) methylammonium (MA^+) vacancy, (D) triiodide (I_3^-) interstitial, (E) lead (Pb^{2+}) interstitial, (F) lead vacancy, (G) Pb–I anti-site defect, and (H) grain boundary. Reproduced with permission from ref. 69 Copyright 2021 Wiley-VCH GmbH.

This brings us to the second critical challenge at the interface: improper energy level alignment. As previously discussed, surface recombination is highly influenced by the built-in electric field at the perovskite/CTL interfaces. The strength and direction of this field determine the efficiency with which charge carriers are extracted and transported across the device.[60] However, when energy levels between the perovskite and charge transport layers are not properly aligned, it can exacerbate charge accumulation, reverse flow, or recombination at the interface, further degrading device performance. Such misalignments not only hinder charge extraction but also disrupt the internal electric fields necessary to drive efficient charge separation. Therefore, addressing energy level alignment is crucial for optimizing charge transport and minimizing recombination losses, setting the stage for the next discussion on strategies to achieve proper interface energy level matching.

3.2. Energy level offsets: a key bottleneck in PSC interfaces

3.2.1 Electronic energy level landscape at semiconductor interfaces. Processes involving transfer of electronic charges, such as injection of holes or electrons, are determined by the configuration of critical electronic energy levels of two semiconductors in contact, which in turn affect device properties.[70] Two energy levels serve as crucial points of reference for the electronic level's position, namely the Fermi level and vacuum level (E_{VAC}). The Fermi level (E_F) is the energy level at which the likelihood of an electronic state being occupied is half or, in other words, it is the highest occupied electronic state when the temperature is zero kelvin. E_F intersects the conduction band within a metal, delineating the boundary between filled and empty states. The Fermi level (E_F) of an intrinsic semiconductor is positioned inside the band gap. E_{VAC} denotes the minimum energy an electron needs to overcome the solid's surface and move into the vacuum. Instead of representing the absolute vacuum level, E_{VAC} represents the local vacuum level, influenced by attracting and repulsive forces such as electrostatic dipoles near the surface.[71] The position of E_{VAC} is substantially influenced by the electrostatic energy landscape and composition at the surface. Since the position of E_{VAC} is intricately shaped by the electrostatic environment and surface composition, the work function (Φ) defined as the energy difference between E_{VAC} and E_F ($\Phi = E_{VAC} - E_F$) serves as a sensitive indicator of the surface electronics. When an interface is formed by bringing together two surfaces into proximity, the work function (WF) of two isolated surfaces can be employed to estimate the energy level alignment and anticipate the direction of charge transfer.[72]

When discussing interfaces in PSCs, electronic transport is mainly due to electrons at the CB edge and holes at the VB edge, provided defect-level-assisted transport is disregarded. Therefore, understanding the location of the E_F in the band gap of a semiconductor and the relationship between the band edges, Fermi level, and vacuum level is crucial. At this juncture, it is important to turn our attention to two more additional energy quantities: electron affinity (EA), which is a measure of the difference in energy between the vacuum level and CB minimum, and the ionization energy (IE), which is defined as
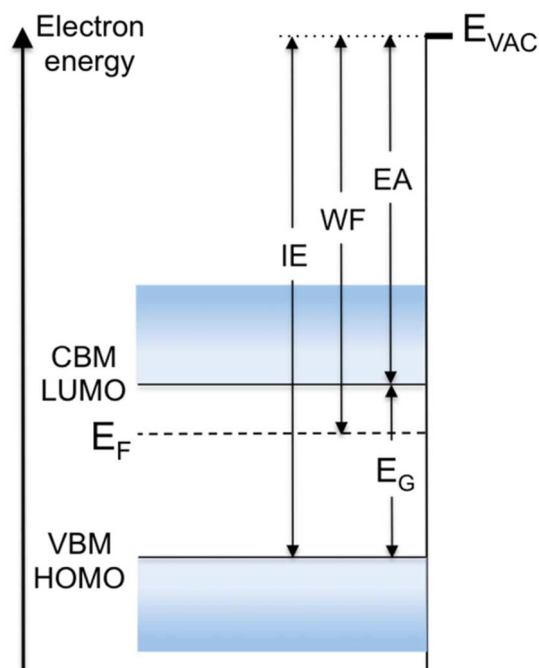

Fig. 10 Semiconductor's energy diagram showing flat bands on the surface. Vacuum level E_{VAC}, WF, energy gap E_G, ionization energy IE, band edges (CBM/LUMO and VBM/HOMO), and electron affinity EA are defined. Images reproduced with permission from ref. 73, Copyright 2015. Royal Society of Chemistry.

the energy difference between the vacuum level and VB maximum.[73] These energy quantities can generally be regarded as the minimal energy released by acquiring a free electron from a vacuum or the minimum energy needed to remove a surface-bound valence electron, respectively. The energy level diagram of a typical semiconductor is shown in Fig. 10.

3.2.2 Band edges and barriers: the interfacial physics of semiconductors. From a broader perspective, classical thin-film semiconductor devices are intricate assemblies comprising a network of interfaces: metal/semiconductor, insulator/semiconductor, insulator/metal, and semiconductor/semiconductor, each governed by distinct physical principles and necessitating tailored modelling frameworks and characterization techniques. When considering halide perovskites, charge transport is primarily mediated by electrons and holes at the CBM and VBM, respectively, assuming negligible contribution from mid-gap defect states or trap-assisted transport mechanisms. Therefore, precise determination of the E_F position within the bandgap, as well as the energetic alignment of the band edges relative to both E_F and the vacuum level, is of fundamental importance.[74] A critical aspect of device performance lies in the band offsets at heterointerfaces. At a metal/semiconductor interface, the valence band offset (ΔE_{VB}) plays a key role in defining hole injection barriers, while in semiconductor/semiconductor junctions, charge transport is dictated by the offset between corresponding band edges: conduction band offsets for electron transport and valence band offsets for hole transport.[70]

Early theoretical frameworks by Mott and Schottky proposed that transport of charges across metal/semiconductor junctions occurs *via* thermionic emission over an energy barrier, determined by the difference between the metal WF and the ionization energy (for p-type) or electron affinity (for n-type) of the semiconductor. This idealized approach, known as the Schottky–Mott limit, assumes no interfacial states or dipoles.[75,76] For semiconductor/semiconductor interfaces, the Anderson model provides an analogous description, wherein the vacuum level alignment of the two materials defines the interface energetics. Within this framework, the energy barrier encountered by electrons or holes is governed by the disparity in electron affinities or ionization energies.[77] However, decades of experimental and theoretical research have shown that these idealized models often fail to capture the complex interfacial physics observed in real devices. Advanced models incorporate phenomena such as interface dipole formation and the alignment of charge neutrality levels, which play a pivotal role in determining the interfacial energy landscape and driving the redistribution of charge carriers at the interface.

3.2.3 Band edge engineering and its role in PSC performance. An appropriate alignment of energy levels at the interfaces is crucial for optimizing the performance of solar cells. Adjusting energy levels can enhance V_{OC} and improve charge transfer and extraction, leading to higher J_{SC} and FF. Two crucial interfaces for aligning the energy levels are those between the perovskite with the hole transport layer (HTL) and with the electron transport layer (ETL) as depicted in Fig. 11.[78] In order to promote the transfer of carriers, it is necessary for the lowest unoccupied molecular orbital (LUMO) of perovskite

Fig. 11 Fundamental energies like ionization energy (IE) and electron affinity (EA), along with the positions of band edges (E_{CBM} and E_{VBM}) of a perovskite layer with a specific band gap (BG) compared to energy levels of adjacent charge transport layers. Reproduced with permission from ref. 78, Copyright 2014. Royal Society of Chemistry.

to be higher than the CBM of the ETL and for the VBM to be lower than the HTL. The transport of electrons across the interface is determined by the variance between the CB edges of the two materials, while hole transport is influenced by the VB edge offset. Critical in determining carrier recombination at the pertinent interfaces are the band offsets of HTL/perovskite and ETL/perovskite. A band offset of approximately 0.2 eV is empirically required for effective charge extraction at the perovskite/CTL interfaces.[79]

The phenomenon known as "band bending" refers to the gradual alteration of a semiconductor's band edge in the vicinity of a junction due to an energy differential with respect to its junction partner.[80] This kind of phenomenon is frequently seen at the interface where the perovskite absorber layer and the transporter layers meet. Kahn and colleagues quantified the band bending at the interface of spiro-OMeTAD and perovskite.[78] Spiro-OMeTAD was discovered to have a reduced ionization energy, resulting in a suboptimal alignment of the energy level with the absorber. This bending introduces an energetic barrier for hole extraction, potentially limiting V_{OC} and reducing overall device efficiency. The underlying cause of this band bending is the disparity in the WF between the HTL and the perovskite. When these materials are brought into contact, Fermi level alignment necessitates interfacial charge redistribution. In the case where the HTL possesses a lower WF, electrons transfer from the HTL to the perovskite, depleting carriers near the HTL surface and causing the energy bands to bend upwards toward the interface. This leads to increased hole trapping and impedes interfacial charge transfer.

In light of the intricate interfacial phenomena delineated across Sections 3.1 to 3.2, it is evident that surface and defect-mediated recombination and energy level misalignment at interfaces represent core limitations to the performance and stability of PSCs. These issues are magnified in tandem configurations, where the multiplicity of interfaces introduces compounded recombination pathways and energetic mismatches. While perovskites possess a unique degree of bulk defect tolerance, it is precisely at their interfaces with charge transport layers that performance is most vulnerable to perturbation. The accumulation of interface trap states, improper band offsets, and unfavorable dipole-induced band bending collectively hinder charge extraction and accelerate degradation. Therefore, addressing these challenges demands more than incremental improvements – it requires a comprehensive, strategic deployment of interface engineering approaches tailored to the distinct physical and chemical characteristics of each heterojunction. Techniques such as interface dipole modulation, surface passivation *via* molecular or ionic additives, compositional tuning of adjacent transport layers, and controlled crystallization pathways are not optional enhancements but rather essential design imperatives. As the field moves toward commercialization and deployment of PSCs especially in complex architectures like tandems serious, nuanced, and targeted interface engineering strategies will play a decisive role in translating laboratory efficiencies into real-world performance and durability which will be discussed in detail in the following section.
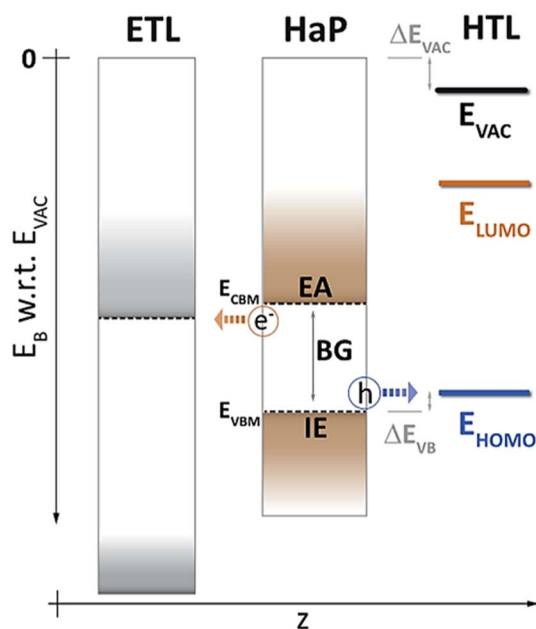
4. Interface engineering in perovskite photovoltaics

As the field of perovskite photovoltaics matures, the focus has progressively shifted from bulk material optimization to the subtleties of interfacial design, where even minor modifications can induce substantial gains in device performance and longevity. Interface engineering strategies now represent a diverse and evolving toolkit that enables researchers to fine-tune charge dynamics, mitigate loss mechanisms, and adapt device architectures for emerging applications. To structure our discussion on interface engineering in perovskite photovoltaics, we begin with an overview of foundational strategies employed in single-junction PSCs (Section 4.1). While not exhaustive, this section highlights representative examples of surface passivation, defect mitigation, and energy level tuning to provide a snapshot of the key approaches that have driven interface innovation to date. Nevertheless, for a more comprehensive treatment of interface engineering strategies in single-junction PSCs, we refer the reader to prior detailed reviews,[56,64,65,81–83] as this lies beyond the scope of the present work. Building on this, Section 4.2 explores the emergence and evolution of self-assembled monolayers (SAMs) as a powerful tool for interfacial modification, tracing their integration into various device architectures. Finally, Section 4.3 delves into the interfacial energetics of chemically modified semiconductors, focusing on how energy level alignment, dipole formation, and band bending influence charge dynamics and recombination at the interface.

4.1. Overview of interface engineering strategies in single junction PSCs

Strategic interface engineering such as tuning the WF of CTLs *via* molecular doping or surface treatments can reduce band bending and improve energy level alignment.[84,85] Even slight increases in the CTL work function can mitigate upward band bending, reduce interfacial energy barriers, and enhance hole extraction. Consequently, minimizing the interfacial energetic mismatch is essential to suppress non-radiative recombination losses and elevate V_{OC}, thereby improving the overall device performance. The need for targeted interface engineering is thus not merely auxiliary but fundamental, offering solutions to tune the electronic structure, passivate surface states, suppress recombination, and modulate interfacial electric fields. In single junction PSCs, a wide variety of interface engineering techniques have been developed to address these multifaceted challenges. Surface treatments with Lewis bases (*e.g.*, thiophene and pyridine), halide salts (*e.g.*, MACl and CsF), small organic molecules, and fullerene derivatives have demonstrated remarkable improvements in passivating undercoordinated Pb^{2+} or halide vacancies at the perovskite surface.[86–92] The idea of surface passivation in PSCs really took off when researchers found that adding a bit of extra PbI_2 could boost efficiency. It helped reduce carrier recombination not just within the perovskite layer itself, but also at the interfaces with the electron and hole transport layers as shown in Fig. 12 a.[93] Since then,

using excess PbI_2 has become a go-to approach in tweaking perovskite compositions.[94–96] Later on, Bi *et al.* took it a step further by carefully adjusting the amount of PbI_2, achieving a remarkable drop in V_{OC} losses and a notable increase in external electroluminescence quantum efficiency.[96]

Lewis base passivation has emerged as another key strategy in interface engineering for PSCs. The idea is fairly straightforward: Lewis bases, which function as lone pair electron donors, interact with undercoordinated Pb^{2+} ions or iodine vacancies in the perovskite, forming stable Lewis adducts that help reduce defect states. Pioneering work was reported by Noel *et al.* in 2014, where they treated the perovskite surface with a thin layer of thiophene or pyridine.[99] These molecules, through strong coordination between the sulfur in thiophene or the nitrogen in pyridine and Pb^{2+}, effectively passivated surface defects as illustrated in Fig. 12b. This treatment led to a notable increase in the time-resolved photoluminescence (TRPL) lifetime and better operational stability under maximum power point (MPP) tracking.

Building on this, Yavari *et al.* used poly(4-vinylpyridine) (PVP), a polymer bearing pyridine groups, as a passivation layer and observed improved performance in MAPbI$_3$-based devices.[100] Other Lewis bases containing amine groups, phosphine groups and diketonate groups have also attracted the attention of the scientific community as proven effective passivation layers since then.[91,97,101] Some of such salient studies are depicted in Fig. 13a–c. Lin *et al.* demonstrated that π-conjugated small molecules, specifically indacenodithiophene end-capped with 1,1-dicyanomethylene-3-indanone, can effectively passivate surface and grain boundary defects in hybrid perovskites as depicted in Fig. 13d.[102] The incorporated Lewis base groups (C=O and C≡N) coordinate with under-coordinated Pb^{2+} ions and Pb clusters, reducing non-radiative recombination. Meanwhile, the n-type π-conjugated backbone enhances electron extraction and transport, contributing to improved device performance. Recently, Li *et al.* used DFT calculations to identify phosphorus-containing Lewis bases as strong binders to Pb^{2+}, with 1,3-bis(diphenylphosphino) propane (DPPP) showing the highest affinity.[103] DPPP effectively passivated defects and bridged grain boundaries in inverted PSCs, enabling devices to retain or slightly exceed an initial ~23% PCE after >3500 hours under AM1.5 illumination at ~40 °C and maintain stability after >1500 hours at 85 °C under open-circuit conditions.

In recent years, buried interface (BI) engineering has emerged as a critical strategy in the development of high-efficiency and stable PSCs, across both regular (n–i–p) and inverted (p–i–n) planar device configurations. The BI defined as the interface between the underlying CTL and the perovskite active layer plays a pivotal role in dictating film crystallinity, charge extraction, defect passivation, and interfacial energy-level alignment.[56] Given that interfacial imperfections can lead to trap-assisted recombination and hysteresis, optimizing the BI has become essential for enhancing both performance and long-term operational stability. In n–i–p structures, where a metal oxide (*e.g.*, SnO$_2$ or TiO$_2$) typically serves as the ETL, chemical modification of the BI has been extensively studied.
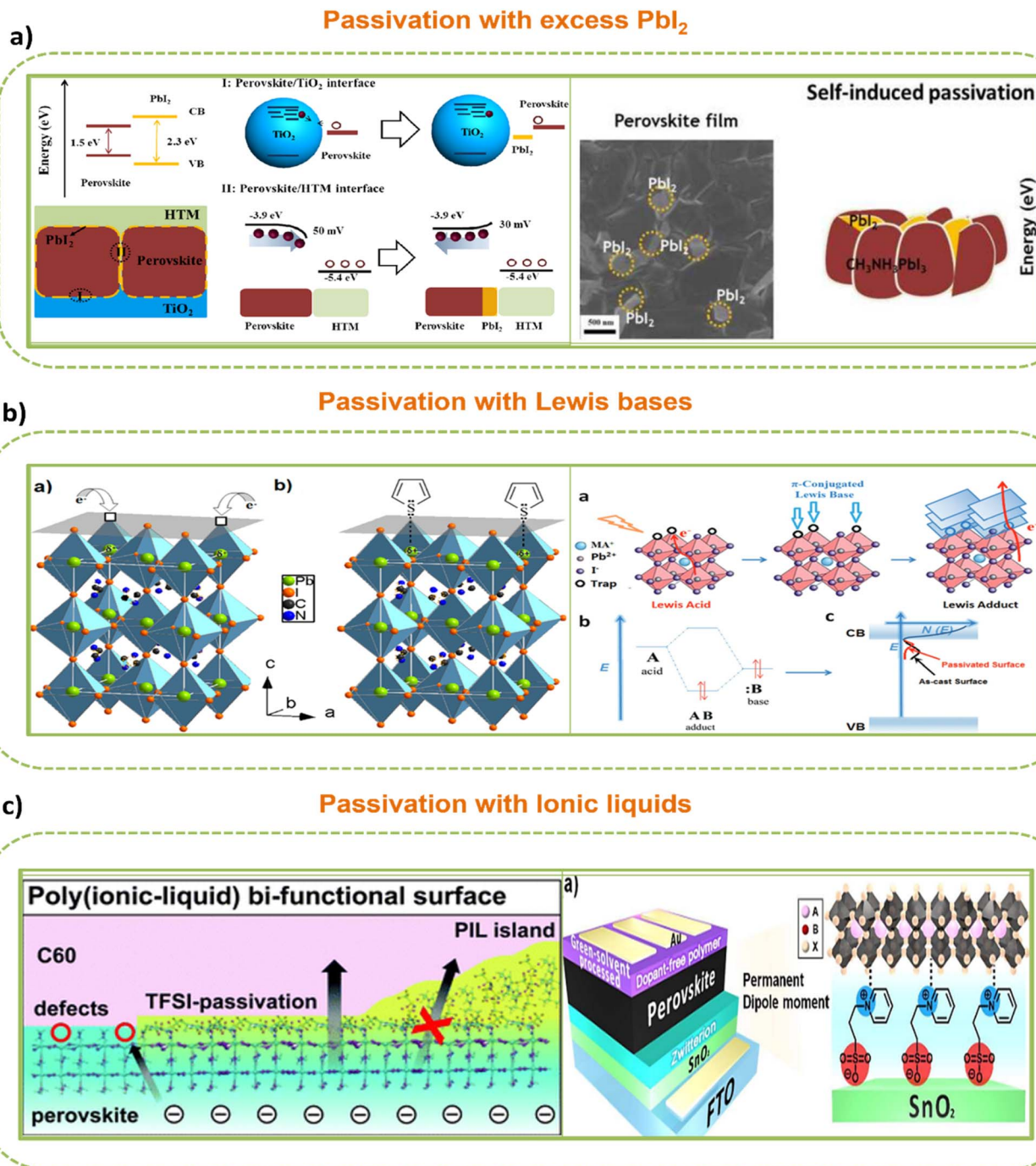
Fig. 12 (a) Schematic illustration of PbI$_2$-induced passivation in CH$_3$NH$_3$PbI$_3$ films. Type-I band alignment between residual PbI$_2$ (2.3 eV) and perovskite (1.5 eV) suppresses interfacial recombination at both TiO$_2$ and HTM interfaces. PbI$_2$ at the perovskite/HTM boundary also modifies grain boundary band bending, reducing carrier losses. Reproduced with permission from ref. 93, Copyright 2014, American Chemical Society. (b) Iodine vacancies creating positively charged Pb^{2+} trap sites and its passivation using coordination of thiophene molecules at perovskite surfaces. Reproduced with permission from ref. 97, Copyright 2014, American Chemical Society. (c) Schematic of passivation by protic ionic liquids (PILs) and surface functionalization of SnO$_2$ with 3-(1-pyridyl)-1-propane sulfonate. Reproduced with permission from ref. 98, Copyright 2021, Royal Society of Chemistry; reproduced with permission from ref. 63, Copyright 2018, Royal Society of Chemistry.

Poor interfacial quality can result in defective nucleation, inferior grain formation, and substantial defect densities, all of which severely degrade device efficiency.[104] To overcome these limitations, a variety of inorganic ionic salts including KCl, KF, and NH$_4$F and functional organic molecules such as zwitterions and self-assembled monolayers (SAMs) have been applied to passivate the surface of SnO$_2$ and tailor the interfacial properties.[105–111] Fig. 12c illustrates some of these studies on interface modification at the ETL/perovskite junction using ionic liquids and zwitterions. These materials mitigate trap
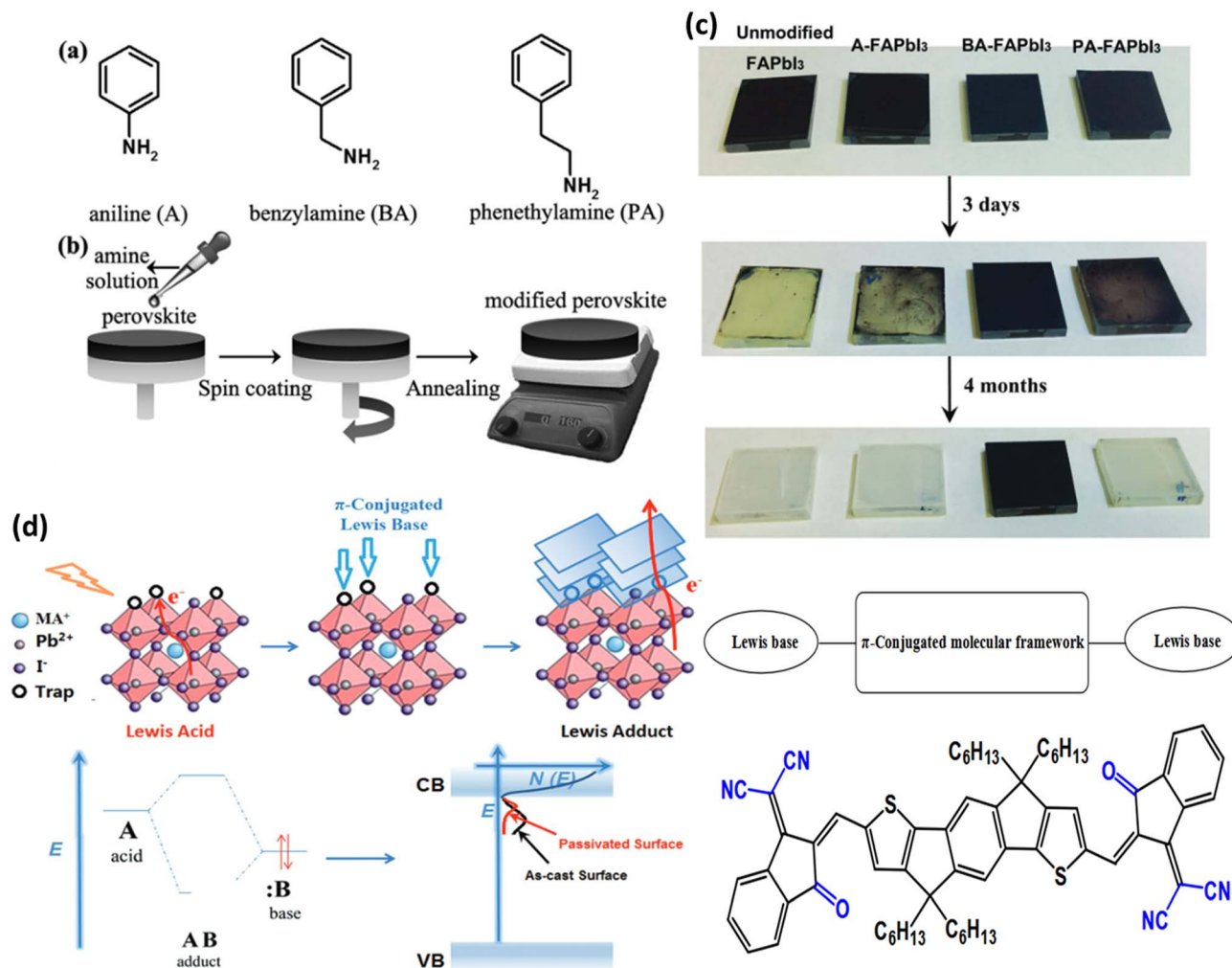
Fig. 13 Amine-based surface treatment and its impact on perovskite film stability: (a) molecular structures of aniline, benzylamine, and phenethylamine; (b) schematic of the spin-coating and annealing process used for amine modification of FAPbI₃ films; (c) visual comparison of untreated and amine-treated FAPbI₃ films over time under controlled humidity exposure. Reproduced with permission from ref. 97, Copyright 2016, Wiley-VCH GmbH. (d) Schematic illustration of trap passivation *via* Lewis base–Pb²⁺ coordination depicting the interaction between π-conjugated Lewis bases and undercoordinated Pb²⁺ ions, leading to dative bond formation and suppression of electronic trap states at the perovskite interface. Reproduced with permission from ref. 102, Copyright 2017, Wiley-VCH GmbH.

densities, improve wettability, and promote more uniform perovskite crystallization. In particular, amine salts have proven effective as pre- and post-deposition additives for SnO₂, facilitating bottom-up BI modification. Their use not only improves CTL quality but also promotes the release of residual stress during thermal processing, driving a favorable transition from thermodynamically unstable to stable perovskite phases with enhanced structural coherence.

A notable benefit of amine salts is their tendency to form low-dimensional 2D perovskite interfacial layers, which act as templating scaffolds for the vertical growth of high-quality 3D perovskite films.[112] These interfacial layers can suppress defect propagation, reduce ion migration pathways, and considerably enhance charge extraction.[113] Additionally, the inherent vulnerability of the buried interface to solvent and thermal damage during fabrication has spurred the development of

alkali metal salt-based strategies. Salts such as KCl, KI, and potassium fluorosulfite (KFSO) have been shown to passivate cation vacancies and grain boundaries both at the BI and within the bulk, thereby mitigating non-radiative recombination and reducing hysteresis.[114–116] Furthermore, recently Chen *et al.* incorporated rubidium halides at the buried interface leading to the *in situ* formation of Rb-based perovskitoid scaffolds, which reinforced interfacial crystallization and passivation. Devices utilizing this approach demonstrated marked PCE enhancements, *e.g.*, from 23.26% to 25.14%.[117]

In contrast, inverted (p–i–n) planar architectures, which utilize hole transport layers (HTLs), such as NiOₓ, PTAA, or PEDOT:PSS beneath the perovskite layer, present a distinct set of challenges and opportunities for BI engineering. The relatively poor wetting behavior and surface energy mismatch between organic HTLs and the perovskite precursor solution
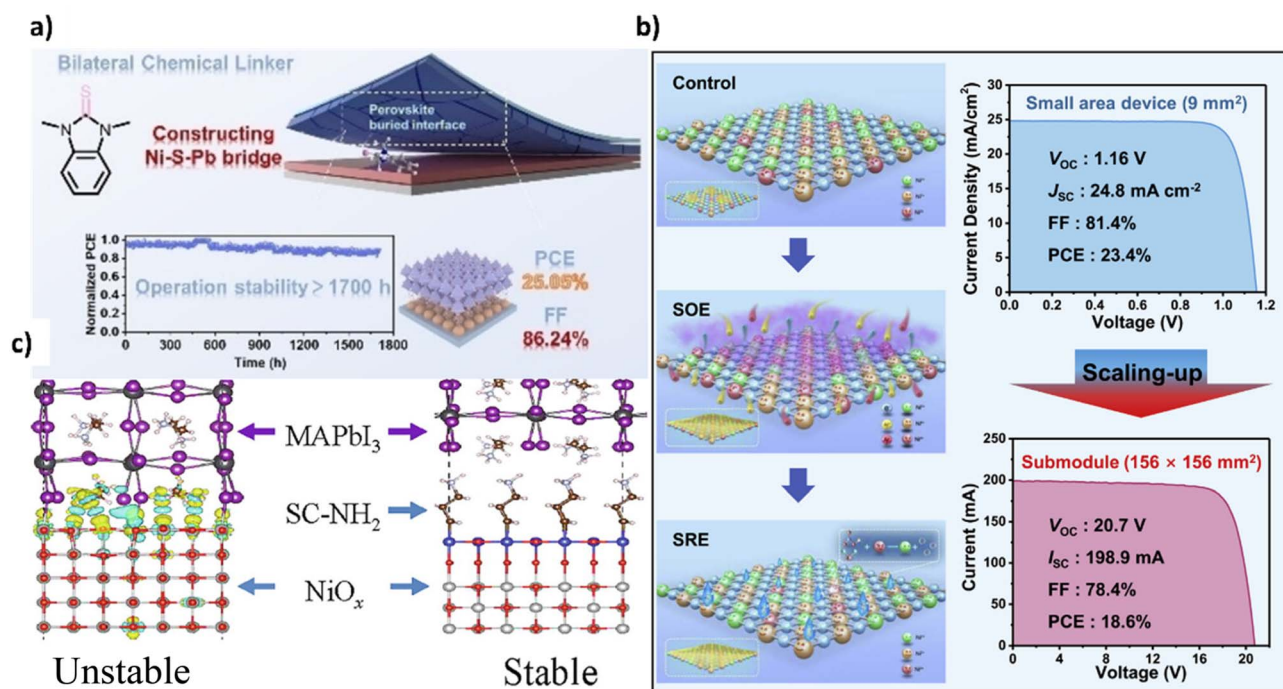
Fig. 14 (a) Bilateral chemical linking at the NiO$_x$ buried interface using 1,3-dimethyl-benzoimidazol-2-thione (NCS). Reproduced with permission from ref. 119, Copyright 2024, Wiley-VCH GmbH. (b) Surface redox engineering (SRE) for electron-beam evaporated NiO$_x$. Reproduced with permission from ref. 120, Copyright 2022, Elsevier Inc. (c) Self-assembled amine-terminated silane monolayer for NiO$_x$ surface passivation. Reproduced with permission from ref. 122, Copyright 2022, Elsevier Inc.

can hinder nucleation, resulting in discontinuous or poorly crystallized films. To address this, various BI modification strategies have been proposed, including surface hydroxylation or plasma treatment of NiO$_x$, amino-functionalized silanes, and molecular interlayers designed to enhance surface polarity and binding affinity.[118–123] Some of these attempts are depicted in Fig. 14. These modifications have been shown to improve perovskite film uniformity, reduce interfacial defects, and increase device reproducibility.

Collectively, these studies highlight that interface engineering is not a one-size-fits-all approach; instead, it must be tailored to the specific physicochemical characteristics of the CTL and the deposition dynamics of the perovskite layer in each device configuration. Whether through chemical additives, surface functionalization, or structural templating, interface modification has become an indispensable component of modern PSC design paving the way for devices with enhanced power conversion efficiency, suppressed hysteresis, and improved long-term stability.

4.2. SAMs in PSCs: a timeline of interface innovation

The development and deployment of SAMs in PSCs represents one of the most transformative interface engineering strategies within the domain of thin-film photovoltaics. SAMs, monomolecular films formed *via* chemisorption of amphiphilic molecules onto reactive substrates, offer exceptional control over interfacial properties at the molecular level.[124] Their

emergence as an essential component in PSCs stems from the growing demand for ultrathin, chemically tailored, and energetically aligned interfaces, particularly in inverted device architectures and tandem configurations.[125] The application of SAMs in PSCs was initially inspired by their success in organic electronics, especially organic field-effect transistors (OFETs) and organic photovoltaics (OPVs), where they were used to modify electrode work functions and promote selective charge extraction.[126] One of the earliest conceptual advances in PSCs was reported by Abrusci *et al.*, who employed a hybrid architecture consisting of a fullerene SAM (C$_{60}$SAM)-functionalized mesoporous TiO$_2$, a CH$_3$NH$_3$PbI$_{3-x}$Cl$_x$ perovskite absorber, and P3HT as the hole-transporting material, achieving a PCE of 6.7%.[127] While C$_{60}$SAM efficiently accepted electrons, it blocked their transfer to the TiO$_2$ scaffold owing to poor energy level alignment and limited electronic coupling as illustrated in Fig. 15. Instead, electrons were transported *via* the perovskite, reducing interfacial losses. This approach enabled a versatile platform for polymer-integrated PSCs and, with spiro-OMeTAD, yielded an improved efficiency of 11.7%.

The application of fullerene SAMs was eventually translated into planar architecture by Wojciechowski *et al.* who introduced a C$_{60}$-based SAM on a TiO$_2$ compact layer.[128] This modification enabled efficient electron extraction and activated both the n–i and i–p heterojunctions, markedly enhancing device operation. The interface engineering strategy markedly improved PCE, from 11.5% to 14.8%, with a peak stabilized output of 15.7%, while simultaneously suppressing hysteresis and non-radiative
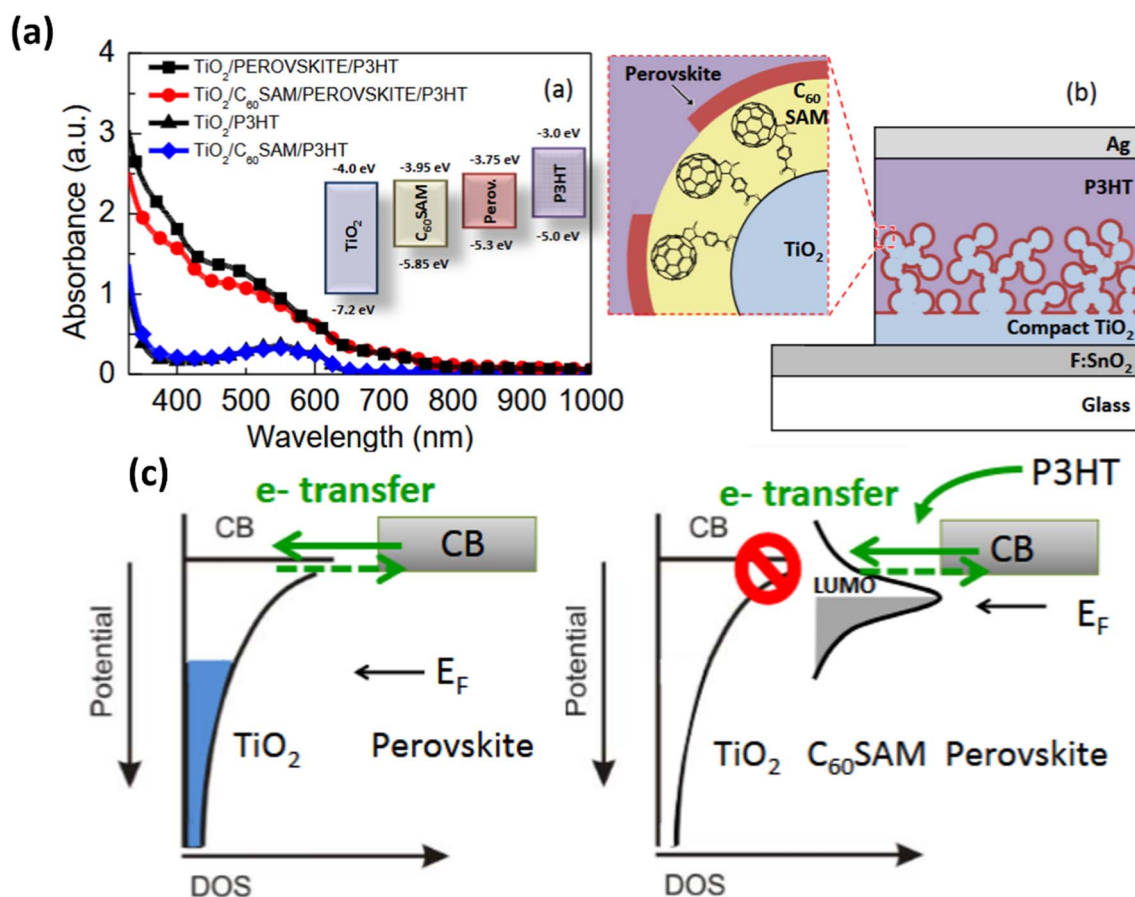
Fig. 15 Impact of C_{60}-SAM functionalization on perovskite optoelectronics and charge transfer: (a) absorption spectra of P3HT/perovskite films with and without C_{60}-SAM modification; (b) schematic of the device architecture; (c) energy level diagram illustrating electron transfer pathways, with shaded DOS regions indicating occupied states in TiO_2 and fullerene layers. Reproduced with permission from ref. 127 Copyright 2013, American Chemical Society.

recombination. The C_{60}-SAM played a pivotal role in passivating interfacial trap states by anchoring to the TiO_2 surface and interacting with the perovskite phase thereby optimizing charge dynamics and establishing its importance in advancing the performance of planar p–i–n PSCs. A more targeted application emerged with Magomedov *et al.*, who explored the introduction of a dopant-free hole-selective SAM, marking the first use of such a layer as a hole transport contact.[129] Utilizing a novel phosphonic acid-functionalized molecule (V1036), the SAM was formed *via* a simple solution-immersion process on indium tin oxide (ITO), enabling efficient charge extraction with minimal parasitic absorption. This strategy delivered PCEs of up to 17.8% and average fill factors approaching 80% as shown in Fig. 16. Beyond performance gains, the approach offered excellent scalability and conformal coverage over large or textured substrates with minimal material and improved absorber quality. Thus, this work marked a turning point: SAMs not only adjusted the ITO work function but also improved film wetting, leading to enhanced perovskite film quality and suppressed interfacial recombination.

Building on these early successes, systematic efforts were undertaken to synthesize and evaluate a broader family of carbazole-based SAMs. The introduction of MeO-2PACz (methoxy-substituted 2PACz) was particularly influential. This molecule was found to substantially increase the ITO WF (by >0.5 eV), reduce interfacial dipole mismatch, and promote ohmic contact formation at the perovskite–electrode interface. Al-Ashouri *et al.* demonstrated that MeO-2PACz could replace conventional polymeric HTLs such as PTAA, leading to inverted PSCs with PCEs exceeding 20%, reduced V_{OC} deficits, and enhanced operational stability.[130] Furthermore, conformal interfacial coverage enabled them to develop monolithic CIGSe/perovskite tandems on rough CIGSe surfaces, achieving a certified 23.26% efficiency on 1 cm² active area as depicted in Fig. 17. Around this period, SAM-based HTLs began gaining favor due to their ultrathin nature (<2 nm), which eliminated parasitic optical absorption and reduced interfacial energetic losses. Additionally, SAMs offered improved chemical stability compared to acidic or hygroscopic polymeric layers. Devices based on MeO-2PACz exhibited improved photovoltage retention under thermal and light soaking conditions, paving the way for their adoption in long-term stability studies.

The next major milestone was the integration of SAMs into monolithic perovskite/silicon (pero/Si) TSCs, where their
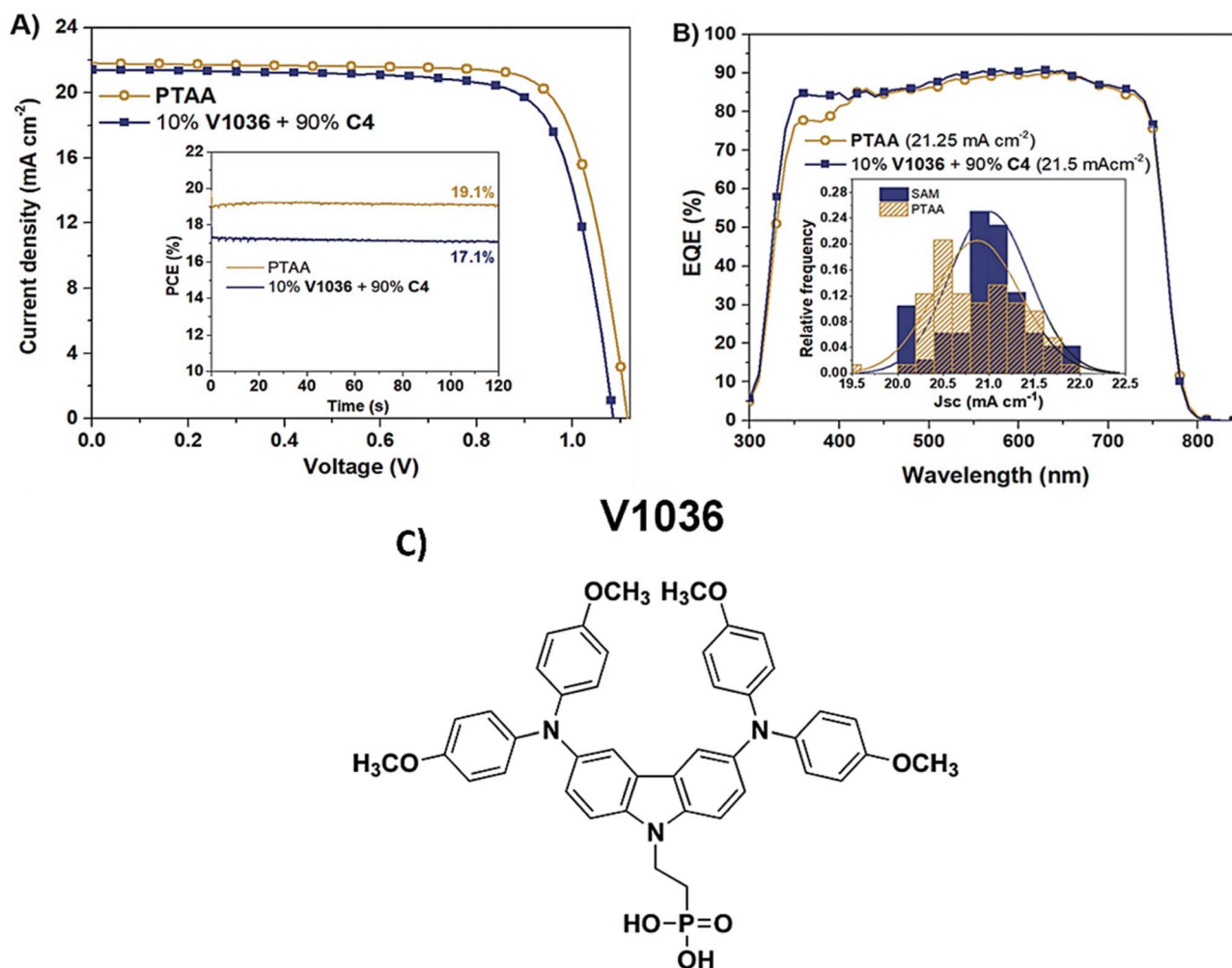
Fig. 16 Photovoltaic performance and spectral response of SAM-modified PSCs. (a) $J-V$ curves and MPP tracking of PTAA devices with V1036/C4 SAMs; (b) EQE spectra of PTAA and SAM–HTM hybrids; (c) structure of a V1036 molecule. Reproduced with permission from ref. 129, Copyright 2018 WILEY-VCH Verlag GmbH & Co.

conformality and chemical robustness became essential. Al-Ashouri *et al.* reported the successful deposition of MeO-2PACz on textured ITO substrates, a critical requirement for integrating SAMs into industrially relevant bottom cells with textured front contacts.[44] The SAM not only enhanced perovskite adhesion and crystallization on the complex topography but also minimized interfacial recombination, allowing tandems to surpass 29% certified PCE. This period also saw the exploration of SAMs on alternative substrates, such as SnO_2 and NiO_x, and their compatibility with scalable deposition techniques like blade coating, slot-die coating, and spray deposition. The ability of SAMs to self-assemble on non-planar and rough substrates was key to enabling large-area device fabrication with high uniformity and reproducibility.

Recent research has focused on expanding the chemical diversity of SAM molecules to incorporate additional functionalities. For example, zwitterionic SAMs, fluorinated derivatives, and phosphorus- or sulfur-containing terminal groups have been employed to fine-tune dipole orientation, improve moisture resistance, and introduce defect passivation capabilities.[131]

Chen *et al.* developed a series of SAMs with tailored alkyl spacer lengths and varying electron-donating/-withdrawing terminal groups to understand the interplay between molecular packing density and energy level alignment.[132] Their findings emphasized that even small changes in the molecular structure could yield notable differences in contact selectivity and interfacial electric fields. The most recent phase of SAM development is characterized by efforts to industrialize their application in large-area modules and tandem architectures. SAMs compatible with roll-to-roll (R2R) processing, exhibiting solvent orthogonality, and demonstrating long-term thermal and photostability are now in focus. In the last 5 years, multiple research groups showcased SAM-integrated minimodules, exceeding 22% efficiency with operational stabilities over 1000 hours under damp heat and continuous illumination.[133] At the same time, the structure–property–function relationship of SAMs is being investigated with greater granularity, including studies on molecular orientation, interfacial dipole formation, and electronic coupling with the perovskite layer. The rapid evolution of SAM-based strategies in PSCs from early fullerene
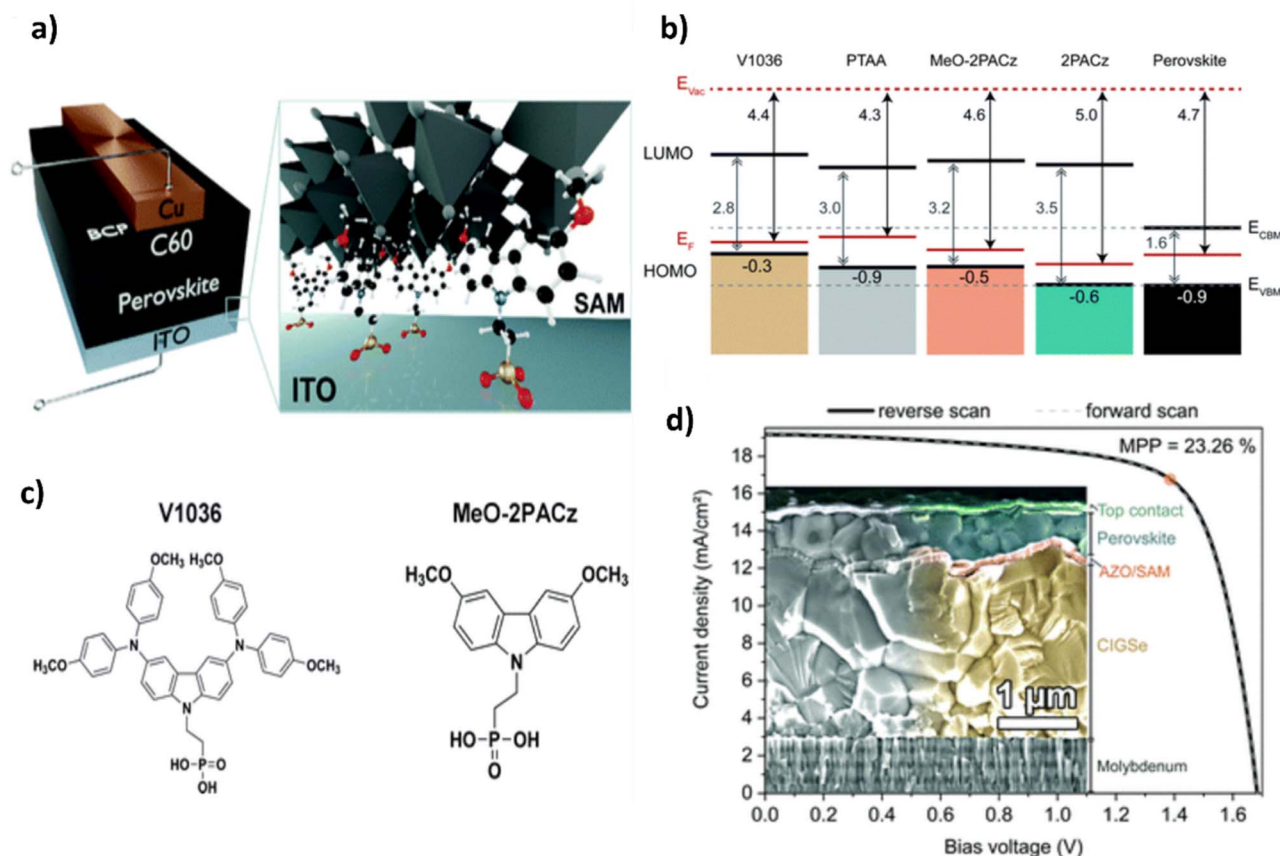
Fig. 17 MeO-2PACz SAMs as ultrathin HTLs in monolithic CIGSe/perovskite tandem solar cells. (a) Schematic illustration of the device stack highlighting the SAM-modified ITO/perovskite interface. (b) Energy level alignment of different SAM molecules relative to the perovskite absorber, illustrating the tuning of interfacial energetics. (c) Chemical structures of representative SAM molecules (V1036 and MeO-2PACz). (d) $J-V$ characteristics of the optimized tandem device incorporating MeO-2PACz, along with corresponding cross-sectional SEM showing the layered architecture. Reproduced from ref. 130 under a Creative Commons CC BY 3.0 license.

monolayers to modern phosphonic acid-functionalized carbazole derivatives has not only enhanced device performance and scalability but also reshaped our understanding of interfacial control at the molecular level. These developments underscore the importance of energetic alignment at the buried interfaces, where even sub-nanometer dipolar modifications can dictate charge selectivity, reduce recombination, and tune built-in potentials. As SAMs increasingly serve as functional replacements for conventional charge transport layers, their influence extends beyond surface chemistry into the realm of interfacial energetics, where molecular dipoles, surface states, and Fermi level alignment govern the electronic structure.

4.3. Interface energetics in chemically modified semiconductors

To fully appreciate and rationalize the performance improvements introduced in the preceding section, it is essential to examine how chemically tailored interfaces, particularly those involving SAMs, redefine the energetic landscape at semiconductor junctions. We now delve into the fundamental principles of interface energetics in chemically modified semiconductors, illustrating how molecular design directly maps onto energy-level tuning, Schottky barrier modulation, and the mitigation of Fermi level pinning. In semiconductor-based devices, particularly those incorporating heterojunctions, the energetic landscape at the interface plays a pivotal role in governing charge injection, extraction, and recombination.[134,135] Historically modeled through the Schottky–Mott framework, the classical approach assumes that the Schottky barrier height (SBH) at a metal–semiconductor (M–S) junction is solely determined by the difference between the metal WF and the electron affinity (χ) of the semiconductor.[136] This idealized description presumes vacuum level alignment and negligible interfacial interaction, yielding the relation:

$$\mathrm{SBH} = \mathrm{WF}_{\mathrm{metal}} - \chi_{\mathrm{semiconductor}} \quad (2)$$

However, experimental observations frequently reveal notable deviations from this model, necessitating a more nuanced understanding of interface energetics. In practice, energy alignment is modulated by the emergence of an interfacial potential step (Δ), which arises from intrinsic dipoles, interfacial states, or chemical bonding.[137] The sign convention for Δ is such that $\Delta > 0$ when the vacuum level increases moving

from the metal into the semiconductor. Thus, a more accurate expression for the SBH becomes

$$\text{SBH} = \text{WF}_{\text{metal}} - \chi_{\text{semiconductor}} - \Delta \qquad (3)$$

The potential step Δ represents a shift in the local vacuum level due to electrostatic reconfiguration at the interface. Its sign and magnitude depend on the direction and density of charge displacement or dipole formation. Importantly, the Fermi level (E_{F}) must equilibrate across the junction at thermodynamic equilibrium, leading to band bending in the semiconductor and establishing a built-in potential (V_{bi}), closely tied to the SBH.[138] The barrier height for an n-type semiconductor is further decomposed into

$$\text{SBH} = V_{\text{bi}} + \xi \qquad (4)$$

where ξ represents the energy offset between the bulk semiconductor's CBM and its E_{F}. When a SAM is chemisorbed onto a semiconductor surface (e.g., Si, TiO$_2$, and ZnO), its net molecular dipole moment introduces a localized potential step at the interface.[139] This modifies the local vacuum level and shifts the energy levels of the semiconductor relative to the adjacent contact (typically a metal or another semiconductor). According to the generalized Schottky barrier equation, Δ includes the contribution of the SAM-induced dipole. SAMs with electron-withdrawing end groups (e.g., –NO$_2$ and –CF$_3$) increase Δ, reducing the barrier for electron injection, while electron-donating groups (e.g., –NH$_2$ and –OMe) can lower Δ, raising the barrier. Such chemical tunability of Δ enables precise control over charge selectivity and injection barriers.

This interfacial rearrangement invalidates the simplistic notion of vacuum level continuity across the junction and introduces the concept of the interface specific region (ISR) – a spatially confined but chemically and electronically distinct zone wherein the frontier orbitals of the adjacent phases hybridize or interact electrostatically.[136] This region accounts for bond polarization at the interface, wavefunction matching between the two materials and charge redistribution due to chemical interactions. Even in the absence of traditional "defect states," such chemical bonding or hybridization effects lead to a built-in dipole, δ_{ISR}, and thus contribute to Δ, modifying the energy level alignment.[140] The ISR is chemically distinct from the adjacent bulk regions and is central to understanding deviations from the Schottky–Mott behavior. In systems with molecular modification, such as SAM-functionalized interfaces, this ISR concept becomes even more critical. SAMs can serve as interfacial capacitors, adding both intrinsic molecular dipoles and interface-induced dipoles via charge rearrangement with the substrate or adjacent contact.[141] SAM molecules occupy this region—replacing native oxides or surface states with a controlled chemical entity. Consequently, within this interface-sensitive region (ISR), dipoles form due to molecular alignment, charge rearrangement occurs between the SAM and the substrate, and band alignment is altered through hybridization or the induction of interface states.[142] SAMs can thus be engineered to define the ISR with desirable electrostatic and electronic characteristics. Energy band alignment and Schottky barrier formation at a metal/n-semiconductor junction via interface-state charging and bond-polarization mechanism are illustrated below in Fig. 18.

The sensitivity of the SBH to changes in the metal work function is often quantified using the index of interface behavior (S) given by[144]

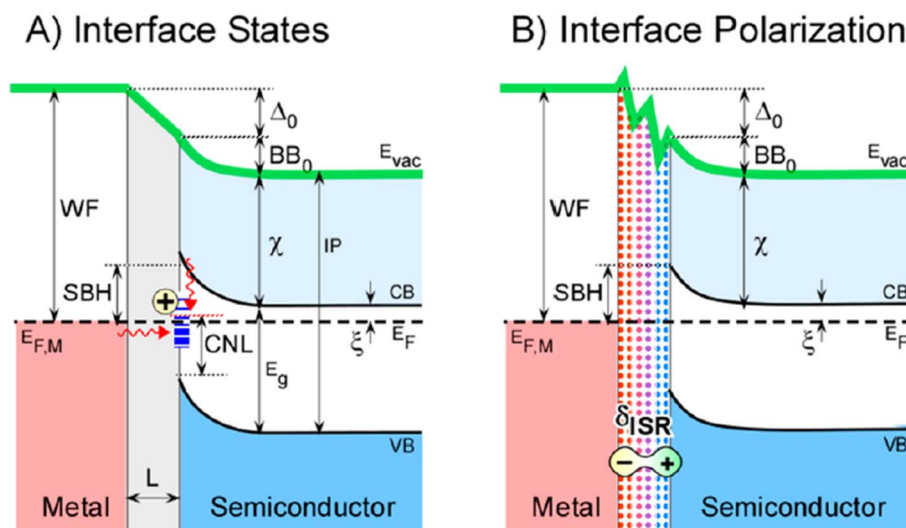$$S = \frac{d(\text{SBH})}{d(\text{WF})} \qquad (5)$$

Fig. 18 Schematic representation of Schottky barrier formation mechanisms at metal/n-type semiconductor interfaces: (A) interface-state-mediated energy level alignment illustrating Fermi level pinning due to a high density of states near the charge neutrality level (CNL), leading to a net interface charge (Q_{IS}) and band bending across the space-charge region (SCR); (B) bond polarization-driven potential step formation at an idealized abrupt interface, where intrinsic dipoles across the interface-specific region (ISR) generate a built-in potential (Δ_0) despite the absence of interface defects or foreign layers. Reproduced with permission from ref. 143, Copyright 2017 American Chemical Society.

Values of $S \to 1$ indicate vacuum level alignment (Schottky–Mott limit), while $S \to 0$ corresponds to Fermi level pinning (Bardeen limit), where the barrier becomes insensitive to the metal's WF and is governed instead by a fixed charge neutrality level (CNL), typically associated with surface or interface states.[145] This transition from intrinsic material properties to extrinsic interfacial characteristics underscores the importance of chemical control at the interface. On bare covalent semiconductor surfaces (like Si), S is typically small ($S \approx 0$), meaning that the Fermi level is "pinned" by interface states. Fermi level pinning is classically attributed to the presence of interface trap states localized electronic states residing energetically within the bandgap.[146] These states act as electron or hole traps, capturing free carriers and distorting the ideal charge distribution. The resulting charge transfer leads to a built-in electrostatic potential, or band bending, that opposes further injection or extraction of carriers. The amount of charge residing in these interface states, Q_{IS}, and its compensation by space charge within the semiconductor Q_{SCR}, yields a net interfacial dipole Q_M:[143]

$$Q_M = -(Q_{IS} + Q_{SCR}) \tag{6}$$

The total SBH under pinning conditions is then approximated as

$$SBH \sim E_g - E_{CNL} \tag{7}$$

where E_g is the semiconductor bandgap and E_{CNL} is the energy of the charge neutrality level.[141] Crucially, this understanding enables the rational design of interface chemistry to mitigate pinning and control the SBH. One effective strategy is the chemical passivation of trap states using self-assembled monolayers (SAMs). SAMs can bind to dangling bonds or defective sites via covalent anchoring groups (e.g., silanes and phosphonic acids), thereby eliminating electronic states within the bandgap and restoring the electronic integrity of the surface. They replace disordered oxide layers with an ordered, dipolar interface, thereby reducing Fermi level pinning and increasing interface behavior (S). A well-ordered SAM with a clean, saturated monolayer can shift interface behavior from the Bardeen limit ($S \approx 0$) toward the Schottky–Mott regime ($S \approx 1$).[147] Furthermore, densely packed SAMs can function as diffusion barriers, suppressing oxidation and chemical degradation of the underlying semiconductor.

By modifying the interfacial dipole and passivating surface states, SAMs also influence the band bending (BB_0) in the semiconductor. Eqn (4) highlights that any change in Δ via SAM-induced dipoles will be reflected in the near-surface potential profile.[145] This is especially critical in photoconductive or photovoltaic devices, where the extent and direction of band bending dictate carrier separation, recombination, and extraction efficiencies. Hence, a judiciously engineered SAM layer can invert surface band bending, improve charge selectivity, and enhance open-circuit voltage in devices such as perovskite or organic solar cells. In addition to removing mid-gap states, SAMs may induce field-effect passivation, wherein molecular dipoles repel majority carriers from the surface, thereby enhancing minority carrier lifetimes even without fully eliminating interface states. Thus, by introducing dipolar fields, altering Fermi level alignment, defining the interfacial region, and controlling band bending, SAMs provide a molecular handle to tune the interfacial electronic structure. This capability is indispensable for enabling the next era of optoelectronic innovation, where performance is fundamentally limited by interfacial energetics. While the preceding discussions have centered on single-junction perovskite devices, the principles of dipole engineering and molecular passivation become even more critical in tandem architectures. Here, multiple sub-cells with dissimilar materials, bandgaps, and fabrication protocols must be seamlessly integrated through electronically and optically compatible interfaces. The application of SAMs and dipole-tailored interlayers in such tandem configurations enables precise control over interfacial energetics, enhances recombination layer performance, and mitigates voltage losses arising from mismatched interfaces. The following section delves deeper into the need for extending and recontextualizing these interface engineering strategies in the domain of tandem photovoltaics.

4.4. Extrapolating interface engineering strategies from single-junction PSCs to tandem architectures

Interface engineering has emerged as a cornerstone of performance optimization in single-junction PSCs, enabling substantial gains in PCE, V_{OC}, and long-term operational stability. These advancements have largely been driven by the strategic manipulation of surface energetics, defect states, and charge extraction barriers at the perovskite/transport layer interfaces as detailed in the preceding sections. Techniques such as chemical passivation, interfacial dipole tuning, and work function modification using SAMs, Lewis bases, and ionic additives have proven highly effective in mitigating non-radiative recombination and aligning energy levels. As TSCs, particularly perovskite-based tandems, advance toward commercial relevance, a critical question arises: to what extent can these single-junction interface engineering paradigms be directly transposed to tandem architectures? The extrapolation is not only plausible and essential but it also demands a more nuanced, holistic, and system-level approach to interface design. Tandem configurations inherently introduce a more complex interfacial landscape, comprising multiple charge-selective layers, recombination junctions, and diverse absorber materials with varying electronic structures. Unlike single-junction devices where the perovskite is interfaced with a single electron transport layer (ETL) and hole transport layer (HTL), tandem devices involve at least two photoactive layers each with its own set of transport contacts necessitating the optimization of multiple nested interfaces. These include perovskite/CTL interfaces within the top cell, the interconnecting or recombination layer between the sub-cells, and in monolithic tandems, the bottom cell interfaces that interact

with the optical and electrical environment imposed by the top cell.

In particular, monolithic (two-terminal) tandems, which are the most industrially viable due to their simplified module integration, pose considerable interfacial challenges. The recombination layer in such devices must facilitate efficient carrier recombination while being optically transparent, chemically inert, and energetically aligned with both sub-cells. Any imbalance in charge transport, improper band alignment, or interfacial recombination at this junction can result in photocurrent mismatch and substantial V_{OC} losses.[148] Crucially, the Fermi level alignment and vacuum level shifts across these interfaces must be optimized to avoid charge buildup and recombination. For example, in a two-terminal tandem, both sub-cells operate under the same current, meaning that any imbalance in interface quality or charge extraction efficiency leads to photocurrent mismatch, reducing the overall performance.[61] While strategies like dipole-inducing interlayers and passivating SAMs have been successful in minimizing energy barriers and trap states in single-junction devices, their integration into buried or recombination interfaces of tandem structures requires additional considerations, such as thermal stability, conformality on textured substrates, and solvent orthogonality during sequential deposition. The transfer of interface engineering strategies such as SAMs and dipole interlayers into tandem cells offers both opportunities and challenges. In single-junction devices, SAMs like MeO-2PACz or PTAA analogues are used to modify ITO or metal oxide substrates, aligning their work functions with the perovskite HOMO or LUMO levels and improving film formation. In tandem cells, these SAMs must play multifunctional roles: they must enable high-quality perovskite deposition, maintain electronic selectivity, and withstand chemical processing steps during the subsequent layer deposition.[149] Moreover, SAM-induced vacuum level shifts must be fine-tuned in tandem architectures to align the Fermi levels across sub-cells. The magnitude and direction of this shift (Δ) due to a SAM is influenced by the molecular dipole moment (μ), the packing density (σ), and the dielectric constant of the medium (ε), approximated using[143]

$$\Delta = \frac{e\mu\sigma}{\varepsilon\varepsilon_0} \qquad (8)$$

This electrostatic model underlines how molecular design namely terminal groups, backbone conjugation, and head-group binding can be used to rationally tune interfacial energetics. However, unlike in single-junction devices where flat, planar substrates are typically employed, tandem cells often involve textured or rough surfaces (*e.g.*, pyramid-textured c-Si). Hence, conformality and uniformity of SAM deposition become crucial.[150] Techniques like molecular vapor deposition (MVD) or solution-based immersion on textured substrates have been explored, but reproducibility and long-term stability remain open challenges.[151]

Furthermore, the perovskite top cell in a tandem device must operate at a higher bandgap ($\sim$1.7–1.8 eV) compared to the $\sim$1.5 eV used in single-junction PSCs. This shift affects the absolute positions of the conduction and valence band edges, necessitating re-optimization of energy level alignment with both ETLs and HTLs. For example, ETLs that are well matched to low-bandgap perovskites may form energy barriers or cause Fermi level pinning when interfaced with wide-bandgap perovskites.[152] As a result, interface energetics must be tailored specifically for the optical and electronic environment of the tandem configuration, rather than relying on established single-junction recipes.

Another key consideration is optical parasitics. In tandem cells, each interfacial layer contributes not only to electronic properties but also to light management. Even minor absorption or reflection losses at interfacial layers tolerable in single-junction designs can compound into substantial efficiency penalties in tandem devices.[27] Interface materials such as SAMs, with their ultrathin, conformal, and optically benign nature, are uniquely positioned to address this constraint, offering a path to low-loss, chemically tailored interlayers. Finally, the mechanical and chemical compatibility of interfacial materials becomes more critical in tandem configurations, particularly for large-area, scalable fabrication.[153] For instance, the use of orthogonal solvents during top-cell deposition must not degrade the underlying bottom cell or previously deposited layers. Here again, interface engineering approaches developed for single-junction devices such as covalently bonded SAMs or robust interfacial passivation layers can be adapted, provided they are engineered with an understanding of multi-stack interactions. From a mechanical standpoint, tandem devices undergo multiple thermal cycles and solvent exposures, necessitating chemically robust and thermally stable interface designs.[154] SAMs with phosphonic acid anchoring groups on TCOs have shown excellent thermal and moisture resistance, making them suitable candidates for tandem integration.

Ultimately, while the physical principles underpinning interface engineering like defect passivation, dipole modulation, and energy level alignment are consistent across single-junction and tandem devices, the architectural complexity of tandem cells demands a systems-level rethinking of these strategies. This includes

- engineering sequential energy level alignment across stacked layers,
- designing optically transparent, recombination-capable interlayers with minimal electrical resistance,
- ensuring chemical orthogonality between layers deposited *via* solution or vacuum processing,
- maintaining mechanical adhesion and stability across interfaces under operational stress.

A robust interface design in tandem devices must not only optimize carrier extraction but also support the physical integration of dissimilar materials with varying thermal budgets, surface chemistries, and processing requirements. Therefore, the translation of single-junction interface strategies into tandem architectures is not a matter of direct replication, but of adaptation, integration, and co-optimization across the full device stack. The following table gives a comparison of interface

Table 1 Key differences in interface engineering for single-junction *vs.* tandem perovskite architectures

Parameter	Single-junction PSCs	Perovskite-based tandem PSCs	Implication for interface engineering
Number of interfaces	Typically, 2 primary interfaces: perovskite/ETL and perovskite/HTL	Multiple nested interfaces: ETL/perovskite, perovskite/HTL, recombination layers, and transparent electrodes	Requires layer-by-layer optimization and holistic interface mapping
Perovskite bandgap	~1.5 eV (narrow bandgap)	~1.7–1.8 eV (top cell) and ~1.2 eV (bottom cell in all-perovskite tandems)	Band alignment strategies must be recalibrated for wider or complementary gaps
Energy level alignment	Focus on aligning with transport layers (ETL/HTL) for efficient extraction	Requires staggered energy levels between sub-cells and recombination layers	Demands precision dipole tuning and redefined WF gradients
Optical constraints	Moderate; focus is on transparency of CTLs and avoiding parasitic absorption	Critical; interlayers must be ultra-thin and low-loss to prevent photon filtering in the bottom cell	Promotes use of optically benign interlayers like SAMs and ultrathin doped contacts
Recombination management	Primarily at perovskite/CTL interfaces	Also occurs at recombination junctions between sub-cells	Requires recombination layers with balanced carrier mobility and minimal barrier height
Processing compatibility	Sequential solution or vacuum processing, usually on flat substrates	Requires cross-compatible materials for sequential top/bottom cell stacking; may involve textured or rough surfaces	Demands solvent orthogonality and conformal coating techniques (*e.g.*, MVD or blade-coating of SAMs)
Surface engineering	Flat, uniform substrates (glass/ITO/FTO)	Textured or rough interfaces (*e.g.*, c-Si pyramids or CIGSe)	Surface passivation layers must ensure conformality and coverage on non-planar surfaces
Stability requirements	Moisture and thermal stability for front-end device	Must withstand cumulative stresses from multi-step processing and operational heating	Interface layers must be chemically and thermally robust
Device architecture impact	Mostly independent of the stack above or below	Interfacial properties affect both sub-cells; *e.g.*, shunt in the top cell reduces current in the bottom cell	Interfaces must be optimized in the context of interconnected device physics

engineering considerations in single-junction and tandem PSCs (Table 1).

5. Molecular interface design in tandem PSCs

5.1. From surface passivation to electrostatic control: a comparison of SAMs and dipole-tailored interlayers

In the realm of interface engineering, both SAMs and dipole-tailored interlayers are widely used to modulate surface properties and interfacial energetics in electronic and optoelectronic devices. Despite their common application in adjusting interface characteristics, SAMs and dipole-tailored interlayers differ fundamentally in their formation, functionality, and impact on device performance. This section will compare and contrast SAMs and dipole-tailored interlayers in terms of their formation, structural characteristics, functional roles, molecular design, and impact on interface engineering. SAMs are formed by the spontaneous adsorption of molecules onto a substrate, typically driven by favorable chemical interactions such as covalent bonding (in the case of thiols on gold or silanes on silicon) or weaker van der Waals and hydrogen bonding forces. The process of self-assembly results in a well-ordered, densely packed monolayer where the molecules align themselves in a specific orientation based on the functional groups present and the substrate's surface chemistry.[155] This organized

structure often ensures uniformity across large areas, making SAMs suitable for applications requiring surface passivation and chemical modification. SAMs typically form a monolayer that is either vertically or laterally aligned, depending on the molecular structure of the adsorbate. While SAMs can exhibit dipolar effects, their primary role is often in providing surface stabilization and altering surface reactivity, rather than directly influencing the electrostatic properties of the underlying substrate in a considerable way.

Dipole-tailored interlayers, on the other hand, encompass a broader range of materials, including polymers, small molecules, or hybrid systems, that are specifically designed to introduce dipoles at the interface. These interlayers may not always form through spontaneous self-assembly but are typically deposited using solution processing, vapor deposition, or other film-forming techniques. Unlike SAMs, which are primarily focused on chemical modification and passivation, dipole-tailored interlayers are designed with the explicit intent of modifying the electrostatic potential at the interface through the alignment and interaction of molecular dipoles.[156] The dipole density, orientation, and molecular packing within these interlayers can be tuned, offering greater flexibility in optimizing the interfacial electrostatic environment. These interlayers are often more flexible in terms of their structural organization, as they are not as constrained by self-assembly processes. This flexibility allows for the creation of interlayers

with specific dipolar characteristics that directly influence the interface's electrical and optical properties. The primary function of SAMs is to modify surface properties such as wettability, chemical reactivity, and adhesion. They are often used for surface passivation, where they reduce surface defects, protect against contamination, and provide a stable, uniform interface that boosts both functional performance and long-term stability. SAMs are particularly useful in applications requiring precise control over surface chemistry, such as in sensors, biosensors, and electronic devices where surface reactivity plays a critical role. While SAMs can introduce dipoles at the interface, their contribution to the electrostatic modulation of the interface is often secondary. Their influence on electronic properties, such as energy alignment or charge injection, is usually modest unless specifically designed to target these effects.[157]

In contrast, dipole-tailored interlayers are designed with the explicit goal of modulating the electrostatic environment at the interface. These interlayers can markedly impact the energy level alignment between the substrate and the active material, which is crucial for optimizing charge injection, transport, and collection in devices like OSCs, PSCs, and organic light-emitting diodes (OLEDs). By introducing an additional dipole moment at the interface, these interlayers create an electrostatic potential step that can shift the vacuum level, thereby controlling the charge injection barriers and improving the overall performance of the device.[158] Additionally, dipole-tailored interlayers can also be designed to enhance stability by passivating interface defects, preventing charge recombination, and protecting the underlying substrate. Thus, while SAMs are primarily used for surface modification, dipole-tailored interlayers play a more direct role in controlling the electrostatic and electronic properties of the interface, making them especially valuable in the engineering of optoelectronic devices. Fig. 19 provides a comparative overview of the structural configurations and dipole alignment schemes of SAMs and dipole-tailored interlayers.

The design of SAMs is focused on achieving stable, well-ordered monolayers with minimal disruption to the underlying substrate's properties. SAM molecules are typically functionalized with specific groups (*e.g.*, thiols, silanes, and carboxylates) that enable them to bond with the substrate surface. These functional groups are often selected based on the desired chemical interaction with the substrate, which could range from strong covalent bonding (*e.g.*, thiol–gold interactions) to weaker physical interactions (*e.g.*, van der Waals forces or hydrogen bonding).[163] The molecular design of SAMs is typically simpler, as the goal is to create a stable, passivating layer without considerably altering the electronic properties of the surface. While the dipolar effect in SAMs is inherent in the structure of the molecules, it is not always the primary focus of the molecular design. The dipole moment can be oriented perpendicular or parallel to the substrate, depending on the specific functionalization of the SAM, but in many cases, its role is secondary to surface passivation and chemical tuning.
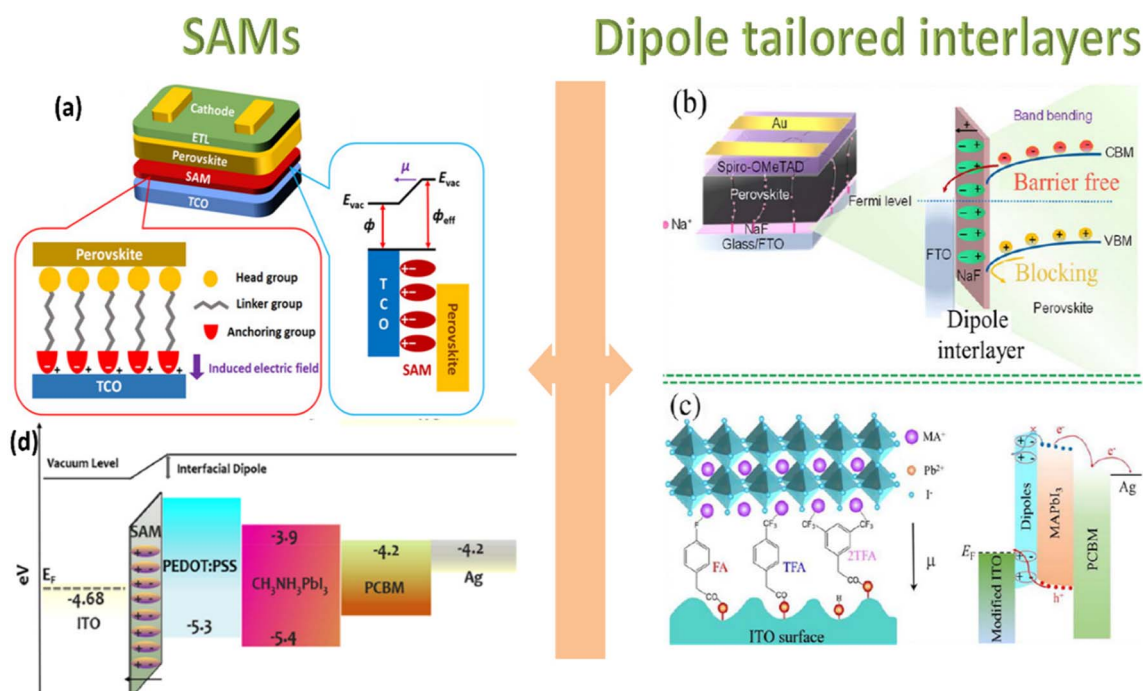

Fig. 19 Schematic overview of SAMs and dipole-tailored interlayers for interface engineering in PSCs. (a) and (b) Illustrations of the structural integration and interfacial dipole formation of SAMs and dipole interlayers at the (TCO)/perovskite interface; reproduced with permission from ref. 159 and 160 Copyright 2022, American Chemical Society and under a Creative Commons CC BY 4.0 license. (c) and (d) Energy level alignment and interfacial dipole effects induced by SAMs and dipole interlayers, enhancing charge extraction and minimizing energetic barriers. Reproduced with permission from ref. 161 and 162 Copyright 2018, American Chemical Society and Copyright 2022 Elsevier Inc.

The molecular design of dipole-tailored interlayers, however, is explicitly focused on creating and controlling dipolar effects at the interface. These interlayers are engineered to introduce specific dipole moments that can align in a way that generates a substantial electrostatic potential step. The molecules used in these interlayers often have functional groups that promote dipole alignment (e.g., electron-withdrawing or electron-donating groups) or facilitate the formation of a uniform, ordered structure that maximizes the dipolar effect.[164] The design process for dipole-tailored interlayers is typically more complex, as it requires careful consideration of factors such as dipole strength, molecular packing density, and orientation relative to the substrate. These interlayers are tailored to maximize their impact on the interface's electrostatic environment, with the goal of enhancing charge injection, transport, and overall device efficiency. Unlike SAMs, which rely on molecular ordering and single-molecule dipole alignment, dipole interlayers typically consist of thin films ranging from a few to several tens of nanometers comprising materials with intrinsic or induced dipolar character. These interlayers do not require long-range molecular order to be effective; rather, their electrostatic influence emerges from net polarization effects, which may originate from permanent dipole moments of the constituent molecules, asymmetric molecular orientation, gradient doping profiles, or charge separation across the film.[165]

The electrostatic potential step (Δ) introduced by such interlayers at the interface arises from the collective dipole moment per unit area, determined from the product of dipole density and the cosine of the average dipole tilt angle relative to the substrate.[166] In contrast to monolayers, here the dipole density is not limited by steric constraints at the surface but can be modulated through film thickness, molecular concentration, and processing conditions (e.g., annealing, solvent polarity, and electric poling). The resulting interfacial electric field can reach magnitudes exceeding 10^8 V m^{-1} in the near field, substantially perturbing the local electronic structure and enabling precise tuning of the vacuum level alignment, EA, and effective WF at the interface.[167]

Crucially, dipole interlayers can modulate semiconductor surface band bending (BB) and Schottky barrier heights (SBHs) without changing the contact metal itself. For instance, positively oriented interfacial dipoles can lower the effective WF of the electrode or increase the EA of the semiconductor, promoting ohmic contact formation and electron extraction. Conversely, negative dipole orientation can enhance upward band bending in n-type semiconductors, resulting in depletion or even inversion regimes effectively mimicking p–n junction behavior.[168] These effects are quantitatively captured by the interface behavior index (S), which reflects the extent to which the induced dipole controls the interfacial potential drop. Notably, values of S approaching unity indicate near-ideal control, with the SBH linearly tracking the induced potential shift ($\chi + \Delta$).[169] While the far-field impact of such interfacial dipoles may be screened by the surrounding dielectric environment, their local electrostatic influence remains substantial due to the confined geometry of the interlayer and the sharp dielectric discontinuity at the interface. Moreover, dielectric properties of the interlayer itself such as relative permittivity, polarizability, and charge relaxation dynamics essentially dictate the stability outcomes and magnitude of the induced dipole.[167] Careful tuning of molecular architecture (e.g., donor–acceptor segments), dipole moment orientation, and film morphology thus becomes essential for optimizing interfacial energetics. Importantly, the electrostatic modulation achieved through such interlayers is chemically robust, compatible with solution-based processing, and scalable rendering this strategy particularly attractive for next-generation solar cells, light-emitting diodes, and transistors where control over interface energetics is pivotal (Table 2).

5.2. Interface engineering using SAMs in tandem perovskite photovoltaics

This section explores the strategic role of SAMs in advancing both perovskite/perovskite and perovskite/silicon tandem architectures. Beginning with all-perovskite tandems where the

Table 2 Comparison between Self-Assembled Monolayers (SAMs) and dipole tailored interlayers at a semiconductor interface

Parameter	Self-Assembled Monolayers (SAMs)	Dipole-tailored interlayers
Formation method	Spontaneous self assembly via chemisorption or physisorption	Deposited via solution processing, spin-coating, vacuum deposition, etc.
Typical thickness	~1–3 nm (monolayer)	~5–50 nm (thin films)
Structural order	Highly ordered and densely packed	Often disordered or semi-ordered
Primary function	Surface passivation, chemical modification, and adhesion tuning	Electrostatic modulation, energy level alignment, and defect passivation
Dipole control	Limited, often incidental	Explicitly designed and tunable
Electrostatic potential step (Δ)	Typically ≤ 0.3 eV	Up to ~1 eV or more
Molecular design	Focused on surface anchoring and passivation	Tailored dipole strength, orientation, and packing density
Dependence on substrate chemistry	Strong (e.g., thiol–Au and silane–Si)	Weaker; compatible with broader material systems
Effect on band bending/SBH	Moderate, substrate-limited	Substantial modulation possible without changing the electrode material
Device applications	Sensors, biosensors, organic TFTs, and molecular electronics	Solar cells, OLEDs, photodetectors, and transistors

challenge lies in harmonizing wide- and narrow-bandgap sub-cells through tailored interfacial layers we then transition to perovskite/silicon tandems, where SAMs are employed to address complex hybrid interfaces between inorganic substrates and solution-processed top cells. Together, these case studies illustrate how molecular interface engineering is integral to the attainment of robust and high-efficiency tandem photovoltaics.

5.2.1 SAMs in all perovskite tandem solar cells. Wide-bandgap subcells have frequently been identified as a key contributor to V_{OC} losses in a wide range of tandem PSCs reported to date. Addressing this challenge, Thiesbrummel *et al.* introduced an integrated three-pronged optimization approach aimed at enhancing the efficiency of high-bandgap perovskites centered on interface and material engineering at critical junctions within the device stack.[170] First, the conventional HTL PTAA was replaced with the carbazole-based SAM 2PACz, enabling better alignment of energy levels alongside decreased recombination at the interface. Second, oleylamine was incorporated into the perovskite precursor solution to modulate crystallization and passivate surface defects, resulting in improved film morphology and optoelectronic quality. Third,

a lithium fluoride (LiF) interlayer was inserted between the perovskite and ETL to further suppress interface-induced non-radiative losses. This combined strategy was applied to triple-cation high-bandgap perovskite compositions with bandgaps of 1.80, 1.85, and 1.88 eV, resulting in substantial reductions in V_{OC} losses as shown in Fig. 20. Notably, the 1.85 and 1.88 eV compositions were especially well-matched with a 1.27 eV narrow-bandgap bottom cell, offering near-optimal bandgap complementarity for tandem integration.

Devices fabricated with these optimized absorbers demonstrated impressive steady-state power conversion efficiencies of 23.4%, 23.7%, and 21.5% for the 1.80/1.27 eV, 1.85/1.27 eV, and 1.88/1.27 eV tandems, respectively. Additionally, replacing PTAA with 2PACz reshaped the interfacial energetics by introducing a well-defined molecular dipole at the perovskite/HTL junction, lowering the hole-extraction barrier and shifting Fermi-level alignment. This reduced non-radiative recombination, recovering the photoluminescence quantum yield (PLQY) to near-bulk levels, and increased V_{OC} by ≈ 10 mV as is clear from the figure. Lai *et al.* developed an integrated optimization strategy for high-bandgap (~ 1.77 eV) flexible perovskite solar cells by employing the carbazole-based SAM 2PACz as the HTL, which
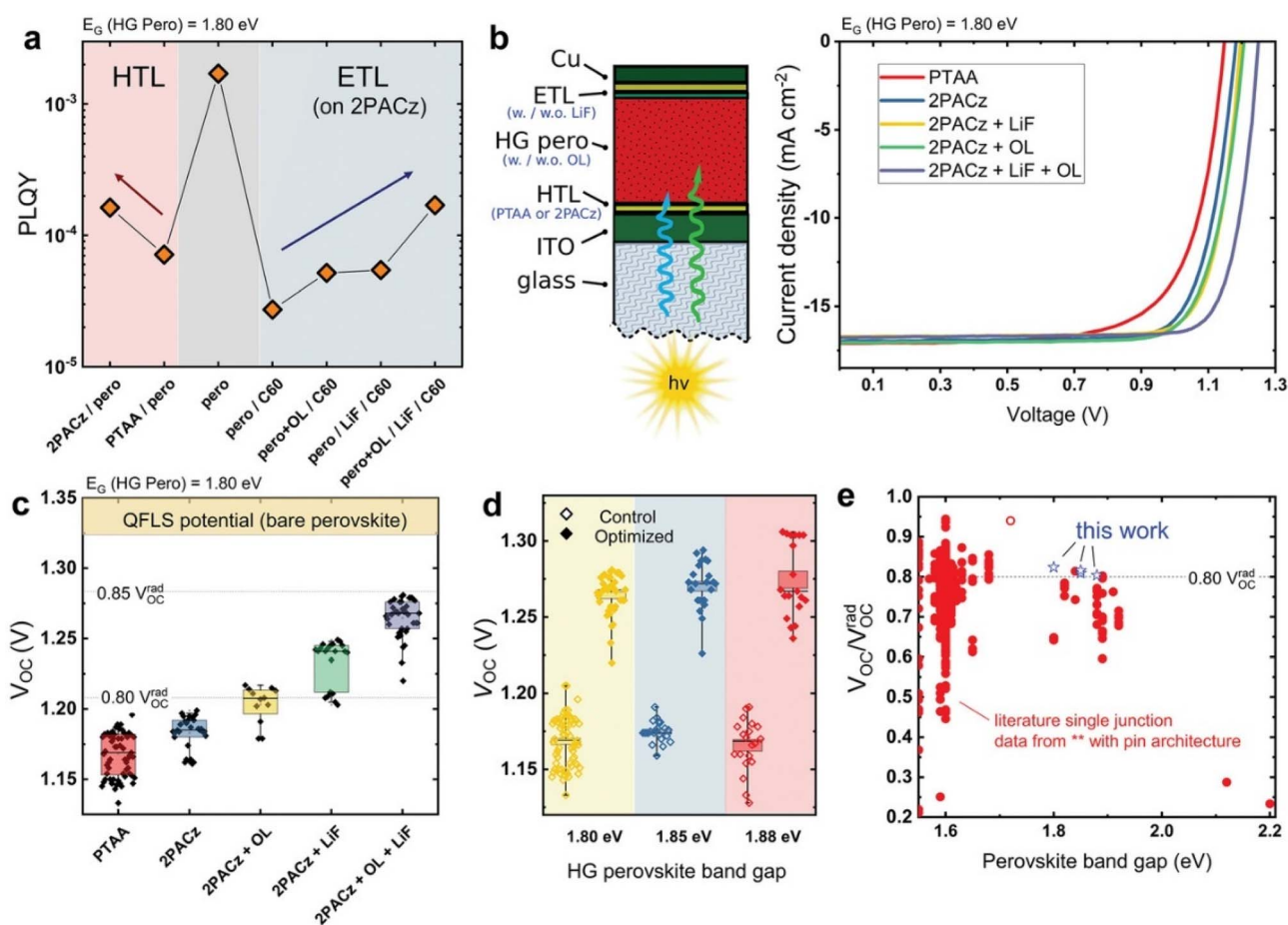

Fig. 20 Comprehensive assessment of radiative efficiency and voltage loss in wide-bandgap perovskite solar cells. (a) PLQY for various device substructures; (b) device schematic and *J*–*V* curves; (c) V_{OC} *vs.* optimization steps; (d) V_{OC} statistics across bandgaps; (e) V_{OC}/V_{OC}^{rad} benchmarking against the literature. Reproduced from ref. 170 Copyright 2022, Wiley-VCH GmbH.

suppressed V_{OC} losses through improved energy-level alignment and enabled uniform perovskite film formation on flexible substrates.[171] Solvent engineering was used to optimize PCBM morphology, while 2-thiopheneethylammonium chloride formed a 2D perovskite surface layer that reduced recombination and enhanced charge extraction by aligning energy

levels at the ETL interface. These combined modifications yielded a V_{OC} of 1.29 V and a PCE of 15.1%, with a record-low V_{OC} deficit (480 mV) for a ~1.80 eV bandgap. By pairing with a flexible 1.24 eV narrow-bandgap cell, they developed the first proof-of-concept 4T all-perovskite flexible TSC with a PCE of 22.6%, along with a 2T TSC achieving a PCE of 23.8%. As
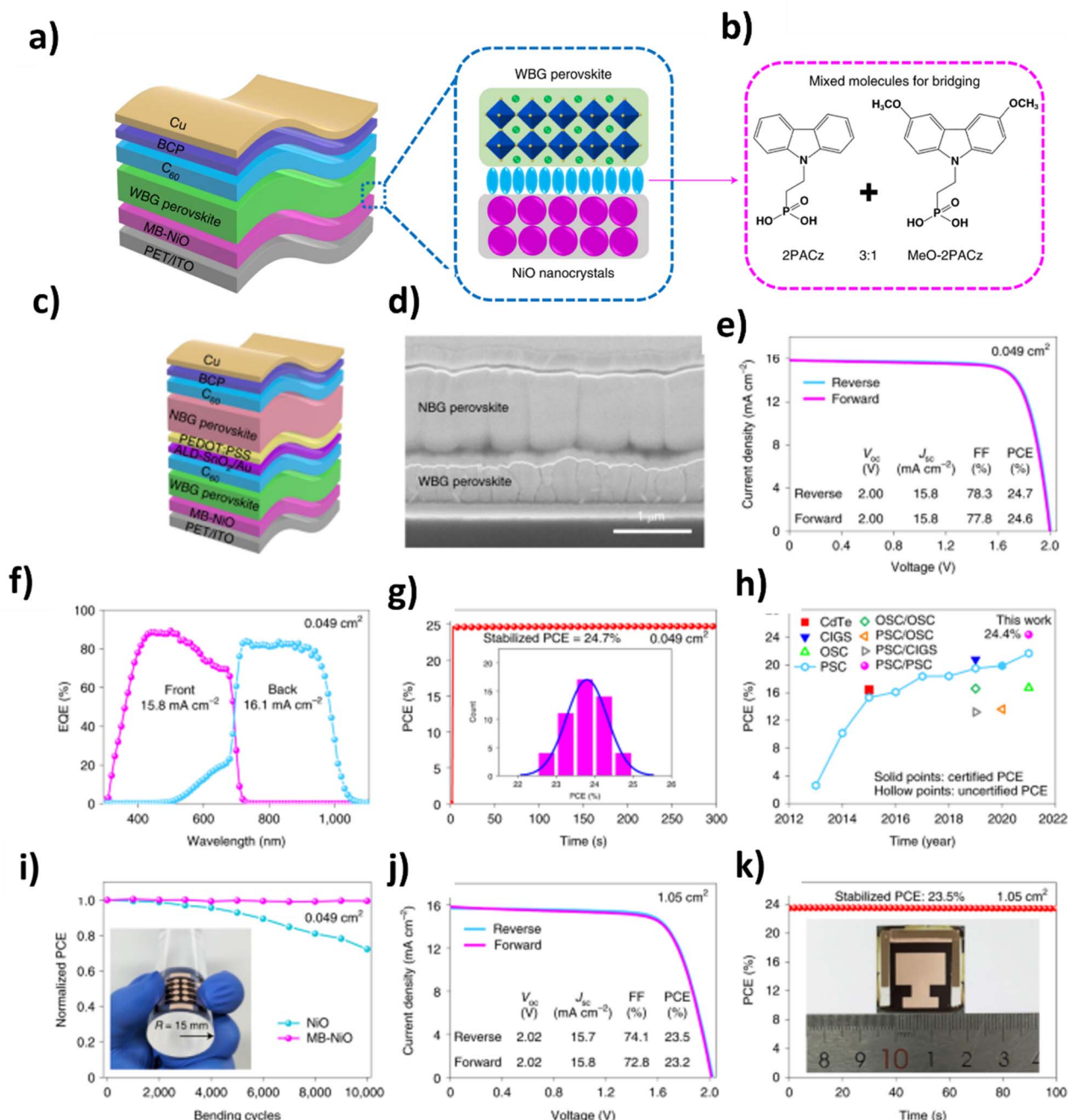

Fig. 21 Flexible monolithic perovskite tandems enabled by nanocrystal-bridged NiO interfaces. (a) Schematic device stack showing WBG/NBG perovskite layers bridged by MB-NiO nanocrystals. (b) Molecular structures of the mixed phosphonic acid SAMs used for NiO surface bridging. (c) Layered architecture of the flexible tandem device. (d) Cross-sectional SEM confirming stacked perovskite absorber configuration. (e) J–V characteristics of the flexible tandem under forward and reverse scans. (f) EQE spectra of the top and bottom sub-cells. (g) Stabilized power output and PCE distribution. (h) Comparison of tandem PCE with reported perovskite and hybrid tandem architectures. (i) Mechanical durability under repeated bending cycles. (j) Large-area flexible tandem J–V performance. (k) Stabilized efficiency measurement of the flexible large-area device. Reproduced with permission from ref. 172 Copyright 2022, Springer Nature Limited.

EES Solar

Review

a monolayer with a well-defined molecular dipole, 2PACz tailored the interfacial electric field, promoting more favorable energy-level alignment between the perovskite valence band and the HTL. This alignment reduced the hole-extraction barrier, minimized energetic offsets, and suppressed charge accumulation at the interface. Furthermore, the strong anchoring of 2PACz to oxide substrates improved the structural order at the contact, thereby reducing interfacial trap states that typically facilitate non-radiative recombination.

In a recent advancement by Li *et al.*, a new molecularly engineered hole-selective interface was developed to overcome limitations in charge extraction and interfacial recombination in flexible perovskite solar cells.[172] This interface, termed molecularly bridged NiO, was created by anchoring a mixture of hole-selective molecules onto low-temperature-processed nanocrystalline NiO films, establishing a well-connected and energetically favorable contact with the perovskite layer. The researchers employed a 3 : 1 blend of 2PACz and MeO-2PACz molecules previously shown to enhance hole selectivity and reduce non-radiative losses to construct the molecular bridge. Using this strategy, they fabricated flexible all-perovskite TSCs comprising a ~1.75 eV $FA_{0.8}Cs_{0.2}PbI_{1.95}Br_{1.05}$ wide-bandgap (WBG) top cell and a ~1.22 eV $FA_{0.7}MA_{0.3}Pb_{0.5}Sn_{0.5}I_3$ narrow-bandgap (NBG) bottom cell. The devices featured an inverted architecture (PET/ITO/MB-NiO/WBG perovskite/C_{60}/ALD-SnO$_2$/Au/PEDOT:PSS/NBG perovskite/C_{60}/BCP/Cu) as shown in Fig. 21, enabling efficient charge transport and optical transparency. This approach led to impressive power conversion efficiencies of 24.7% (0.049 cm^2) and 23.5% (1.05 cm^2), while also imparting exceptional mechanical resilience maintaining performance after 10 000 bending cycles with a 15 mm bending radius.

Wang *et al.* developed a versatile SAM-based HTL that matched the performance of widely used HTLs like PTAA and PEDOT:PSS in WBG PSCs.[173] The SAM was derived from (4-(10-bromo-7*H*-benzo[*c*]carbazol-7-yl)butyl)phosphonic acid (BCBBr-C4PA), incorporating an asymmetrical conjugated backbone and bromine substitution to enhance molecular solubility and increase dipole moment. This molecular design led to a lower HOMO energy level and negligible light absorption, facilitating efficient hole extraction while minimizing interfacial non-radiative recombination. Devices employing BCBBr-C4PA achieved a peak PCE of 18.63%, maintaining over 90% of their initial efficiency after 250 hours of continuous operation. Furthermore, by pairing the optimized WBG cell with a narrow-bandgap perovskite bottom cell, the resulting 4T all-perovskite TSC reached an impressive PCE of 26.24%, underscoring the potential of SAM-based HTLs in high-efficiency tandem architectures. The rapid efficiency gains in small-area (<0.1 cm^2) series-connected TSCs have largely stemmed from advancements in NBG perovskite subcells (~1.25 eV). However, scaling up remains challenging, particularly for WBG top subcells (>1.75 eV) in large-area (>1 cm^2) devices. To address this, He *et al.* introduced a SAM of 4-(7*H*-dibenzo[*c*,*g*]carbazol-7-yl)butyl phosphonic acid (4PADCB) as an HTL tailored for WBG perovskite solar cells.[174] This SAM enabled the uniform growth of high-quality 1.77 eV perovskite films while suppressing

interface-related non-radiative recombination and enhancing hole extraction. The resulting devices exhibited a high V_{OC} of 1.31 V, corresponding to a low V_{OC} deficit of just 0.46 V as illustrated in Fig. 22. By incorporating these optimized WBG subcells into a monolithic all-perovskite tandem architecture (total aperture area: 1.044 cm^2), the team achieved a certified PCE of 27.01%, with an impressive V_{OC} of 2.12 V and a fill factor (FF) of 82.6%.

In a recent study, Jiang *et al.* highlighted the critical role of SAMs in enabling high-performance TSCs, particularly when combined with a gas-quenching method optimized for bromine-rich perovskite compositions.[175] The WBG perovskite absorber (1.75 eV) was deposited on an ITO substrate modified with a mixed SAM of MeO-2PACz and Me-4PACz, which played a vital role in aligning interfacial energy levels, suppressing non-radiative recombination, and ensuring efficient hole extraction. The complete tandem device-comprising a glass/ITO/SAM/WBG perovskite/LiF/C_{60}/SnO$_x$/Au/PEDOT:PSS/NBGperovskite/C_{60}/BCP/Ag stack-integrated this optimized WBG sub-cell with a 1.25 eV Sn–Pb narrow-bandgap absorber, achieving a remarkable PCE of 27.1% and a high open-circuit voltage of 2.2 V. The SAM-enabled interface engineering was instrumental in facilitating efficient charge transport and maintaining device stability.

Chen *et al.* addressed the persistent issue of high V_{OC} deficits in wide-bandgap (WBG >1.7 eV) PSCs, which typically suffer from greater non-radiative losses compared to lower bandgap counterparts (~1.5 eV).[176] Quasi-Fermi level splitting (QFLS) analyses revealed that these losses were largely driven by interfacial recombination at the ETL, exacerbated by non-uniform surface potentials and poor energy level alignment. To mitigate these losses, the authors introduced 1,3-propanediammonium iodide (PDA) as a surface passivation layer, improving the perovskite's surface uniformity and reducing trap-assisted recombination. Crucially, this strategy was integrated with a device architecture that included a SAM of Me-4PACz on NiO$_x$, which functioned as a hole-selective contact. The SAM not only provided favorable energy level alignment but also minimized interfacial losses at the hole transport interface further enhancing carrier extraction in the WBG sub-cell. With PDA and the SAM combined, the WBG PSC (1.79 eV) achieved a QFLS improvement of 90 meV, a certified V_{OC} of 1.33 V, and a PCE over 19%. Integration into a monolithic all-perovskite TSC yielded an impressive V_{OC} of 2.19 V and a certified steady-state PCE of 26.3%, with devices maintaining over 86% of their initial performance after 500 hours under-scoring the synergistic benefits of SAM-assisted interface engineering for efficient and stable TSCs as illustrated in Fig. 23.

5.2.2 SAMs in perovskite–silicon tandem solar cells. Self-assembled monolayers (SAMs), owing to their covalent attachment to substrate surfaces, offer robust interfacial stability and excellent conformal coverage, even on textured silicon, a key requirement for monolithic perovskite–silicon TSCs. Capitalizing on these advantages, Ou *et al.* developed a dual-interface engineering strategy to improve both the quality and stability of MA-free WBG perovskite absorbers.[177] They employed a mixed SAM composed of 2PACz and MeO-2PACz as a hole-
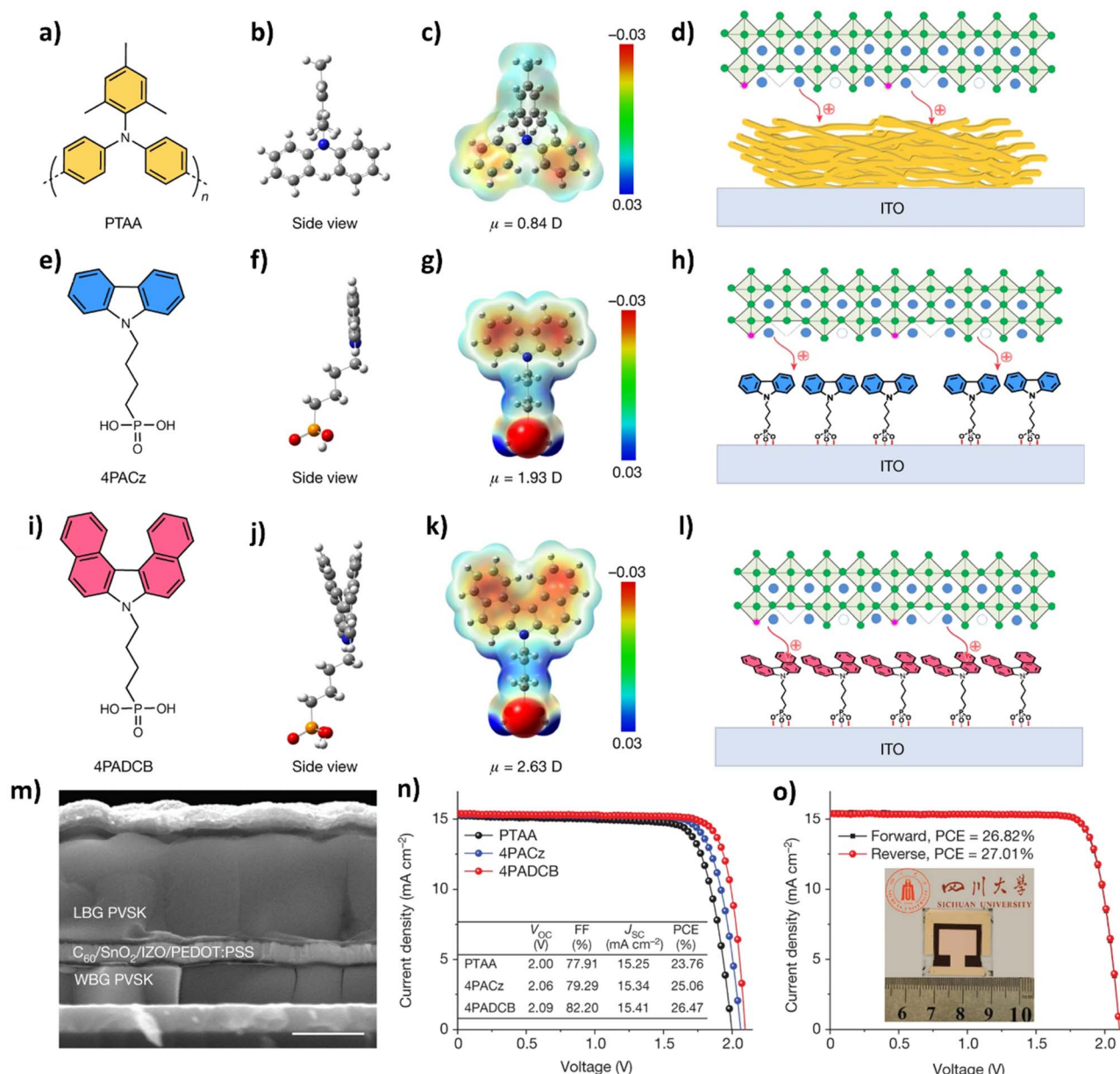
Fig. 22 Comparison of PTAA and phosphonic acid-based SAMs as hole-selective contact layers in all-perovskite tandems. (a–d) PTAA: molecular structure, molecular configuration, electrostatic potential map, and schematic interface arrangement on ITO/perovskite. (e–h) 4PACz: molecular structure, molecular configuration, electrostatic potential map, and interface arrangement. (i–l) 4PADCB: molecular structure, molecular configuration, electrostatic potential map, and interface arrangement. (m) Cross-sectional SEM of the tandem device stack incorporating the SAM-modified hole contact. (n) J–V characteristics of tandem devices using PTAA, 4PACz, and 4PADCB hole contacts. (o) Stabilized efficiency measurement of the optimized tandem device. Reproduced with permission from ref. 174 Copyright 2023, Springer Nature Limited.

selective layer to reduce charge transport barriers and facilitate the growth of large-grained perovskite films. Simultaneously, they passivated surface defects using 4-trifluoromethylphenyl iodide ammonium to suppress recombination losses. This synergistic modification led to notable improvements in V_{OC} and PCE. Devices with opaque and transparent contacts achieved PCEs of 20.11% and 17.80%, respectively, with the opaque device retaining over 85% of its original performance after 1750 hours of storage in an inert environment. Leveraging the optimized WBG sub-cell, a 4-T perovskite–silicon TSC was

assembled, reaching a high efficiency of 26.59%. These results underscore the critical role of SAMs in enhancing charge extraction, film morphology, and operational stability in advanced TSC architectures.

Isikgor et al. demonstrated a synergistic strategy combining chemical passivation and SAM-based interface engineering in TSCs.[178] They employed phenformin hydrochloride (PhenHCl), a multifunctional molecule with both electron-rich and electron-deficient moieties, to effectively suppress interfacial and bulk defects, reduce ion migration, and prevent light-
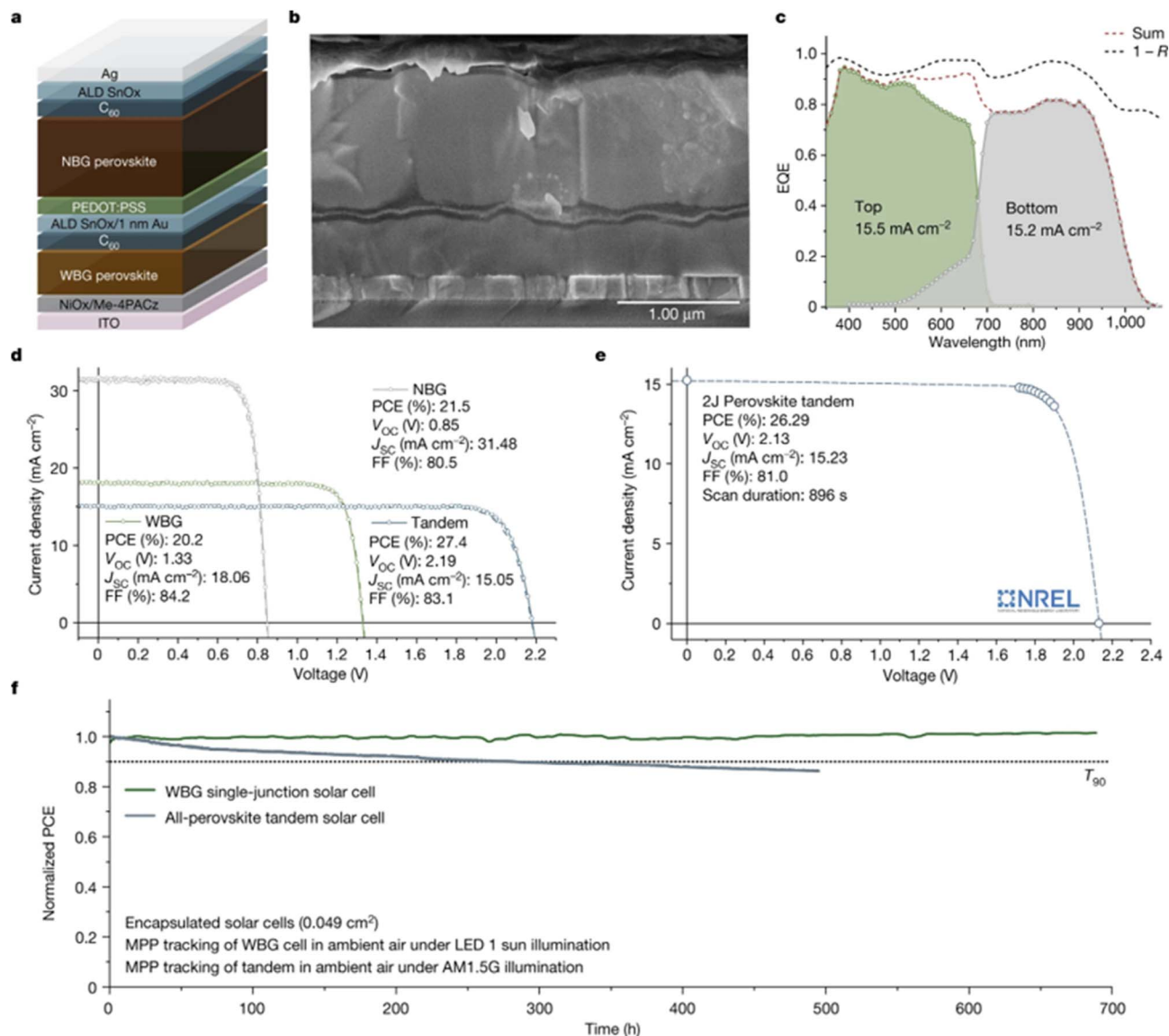
Fig. 23 All-perovskite tandem solar cells incorporating 1,3-propanediammonium iodide (PDA) surface passivation layer and Me-4PACz SAM modified NiO_x HTL. (a) Schematic of the monolithic tandem device architecture. (b) Cross-sectional SEM confirming the stacked WBG/NBG perovskite configuration. (c) EQE spectra of the top and bottom sub-cells with integrated current densities. (d) $J-V$ characteristics of the individual sub-cells and the monolithic tandem. (e) Stabilized power output of the tandem device under MPP tracking. (f) Operational stability under continuous illumination for both tandem and single-junction reference cells. Reproduced with permission from ref. 176 Copyright 2022, Springer Nature Limited.

induced phase segregation in WBG (≈ 1.68 eV) perovskite absorbers. This passivation led to a substantial V_{OC} improvement (~ 100 mV) and a PCE of 20.5% in standalone p–i–n perovskite devices. To further optimize charge extraction and minimize interfacial recombination, 2PACz was introduced as a hole-selective contact. The SAM provided strong covalent anchoring to the ITO substrate and favorable energy level alignment with the perovskite layer, enabling efficient hole transport and enhanced device stability, as is evident from Fig. 24.

The combined application of PhenHCl passivation and 2PACz SAM substantially boosted the efficiency of monolithic perovskite–Si tandem solar cells, elevating the PCE from 25.4%

to 27.4%, alongside improved thermal robustness, as devices maintained V_{OC} even after 3000 hours at 85 °C in a N_2 atmosphere.

Zheng *et al.* demonstrated that integrating 2PACz on NiO_x markedly improved the interface quality in inverted perovskite–Si tandem solar cells using tungsten-doped indium oxide electrodes as illustrated in Fig. 25.[179] The SAM served as a crucial interfacial layer, enhancing energy level alignment and suppressing recombination losses at the NiO_x/perovskite junction. Through a combined NiO_x/SAM hole transport strategy, they achieved superior performance compared to using either material alone. Additionally, the incorporation of PCBM as a light-management layer addressed both scattering-related
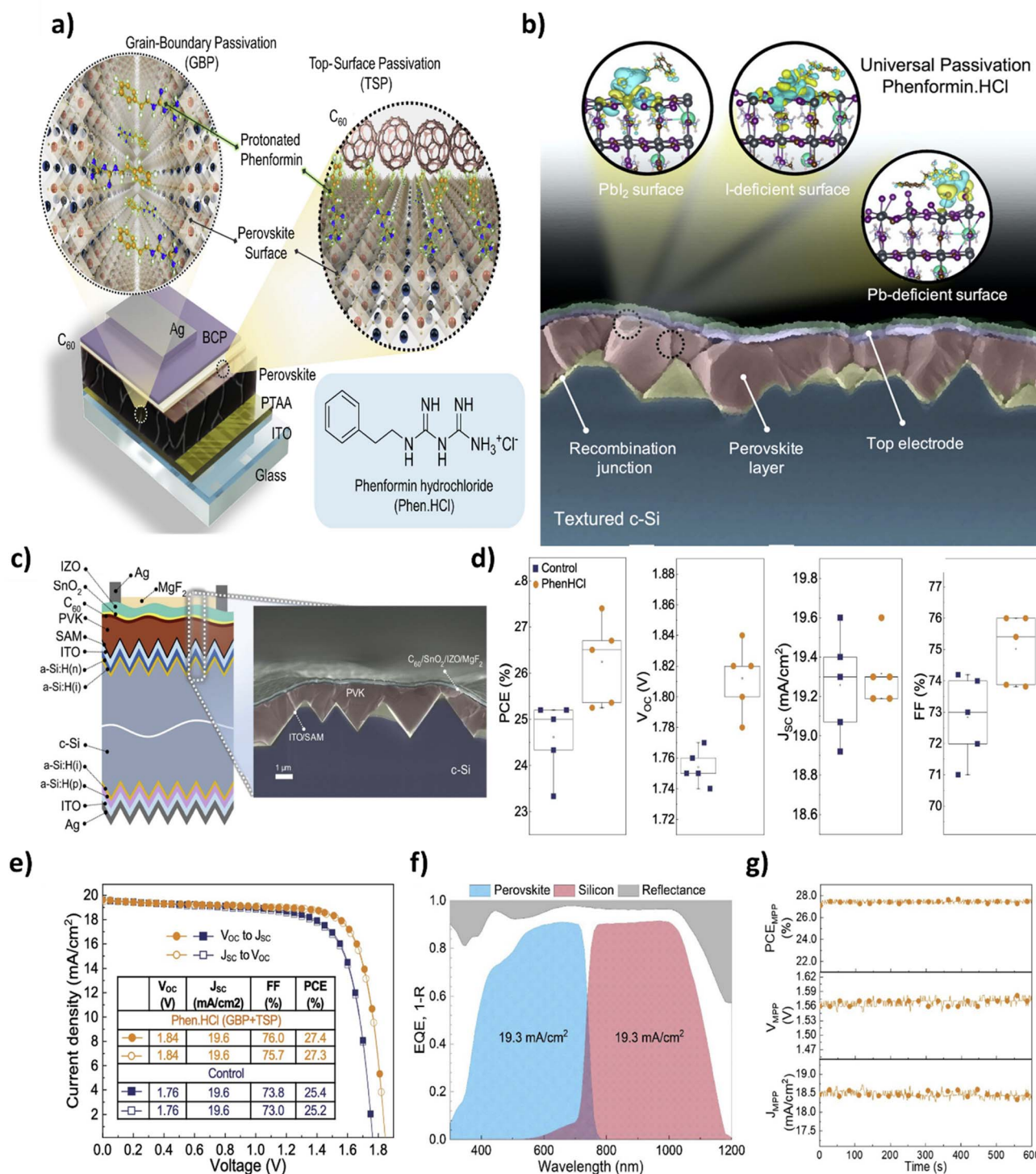
Fig. 24 Phenformin·HCl-assisted grain-boundary and surface passivation in perovskite/silicon tandem solar cells. (a) Schematic illustration of grain-boundary and top-surface passivation enabled by Phenformin·HCl. (b) Conceptual depiction of universal defect passivation across Pb-rich, Pb-deficient, and I-deficient surfaces. (c) Cross-sectional device architecture and SEM image of the textured c-Si/perovskite tandem interface. (d) Statistical comparison of device parameters for control and Phenformin·HCl-treated tandems. (e) J–V characteristics of treated and control tandem devices. (f) EQE spectra of the perovskite top and silicon bottom sub-cells with integrated current densities. (g) Operational stability under continuous MPP tracking. Reproduced with permission from ref. 178 Copyright 2021 Elsevier Inc.

reflection losses and parasitic absorption, thereby optimizing optical energy transfer to the underlying silicon cell. This synergistic interface and optical engineering enabled the pero/Si tandem device to reach an impressive PCE of 27.6%.

Ying *et al.* demonstrated high-efficiency monolithic perovskite/silicon TSCs incorporating a tunnel oxide passivated contact (TOPCon) structure with nanostructured black silicon (b-Si) as the bottom cell.[180] A key innovation in the device
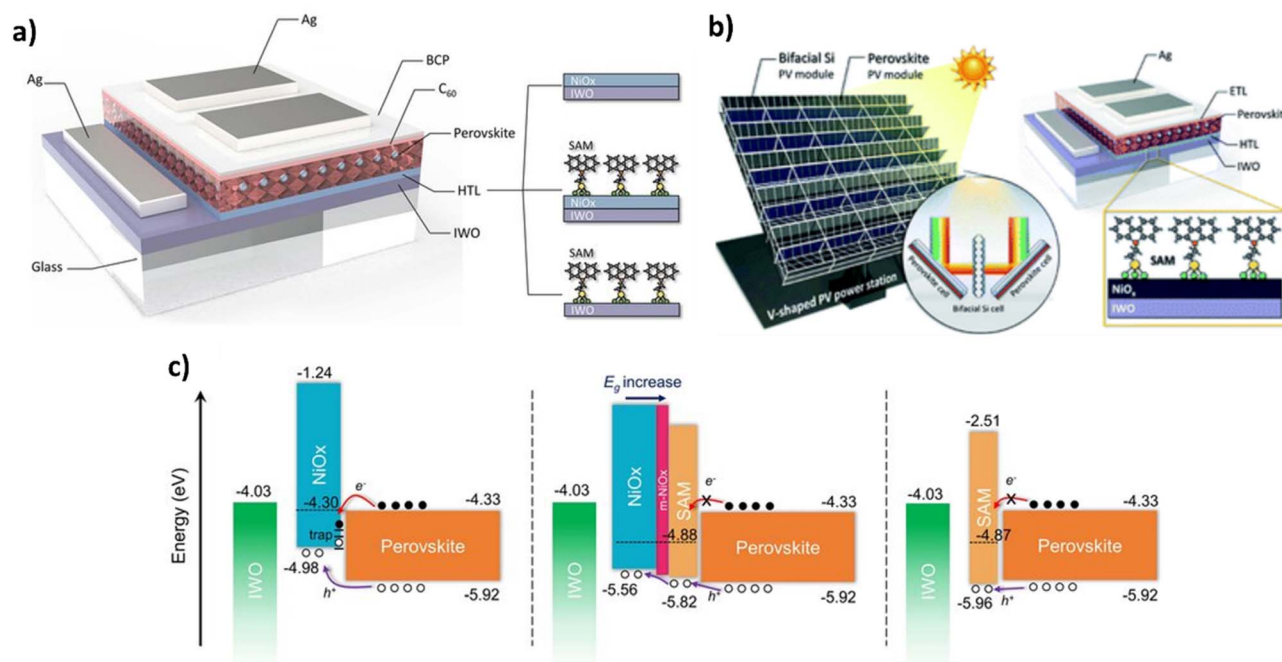
Fig. 25 Interface engineering and photon management in inverted perovskite subcell based TSCs employing IWO transparent electrodes and SAM-modified NiO$_x$ hole transport layers. (a) Device architecture illustrating SAM functionalization on NiOx/IWO hole-selective contacts in perovskite cells. (b) Conceptual integration of SAM-modified perovskite modules with bifacial Si modules in a tandem power station layout. (c) Energy level alignment diagrams comparing interfacial band structure and carrier transfer pathways before and after SAM modification. Reproduced with permission from ref. 179, Copyright 2022, Royal Society of Chemistry.

architecture was the application of a carbazole-based MeO-2PACz SAM at the indium zinc oxide/perovskite interface. This SAM acted as a highly effective hole-selective layer, contributing to improved interfacial energetics, reduced carrier recombination, and enhanced overall device performance. The integration of these strategies resulted in a TSC achieving a notable PCE of 28.5%. Mishima's study focused on enhancing the performance of inverted perovskite–silicon TSCs through
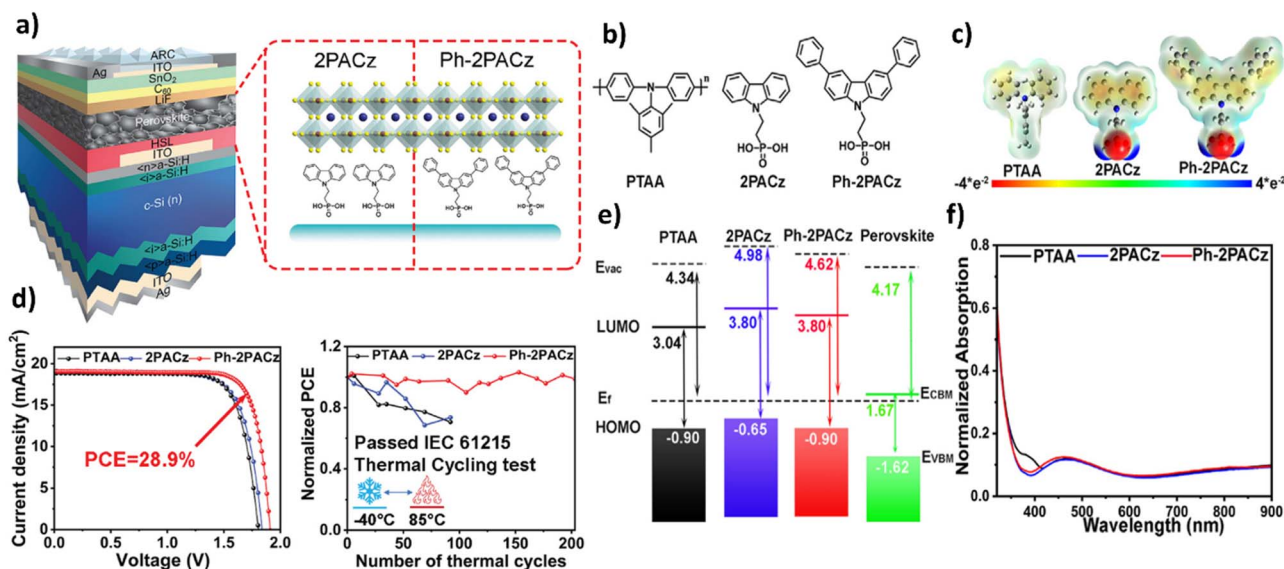

Fig. 26 Comparison of PTAA, 2PACz, and Ph-2PACz hole-selective layers in perovskite/silicon tandem solar cells: (a) schematic illustration of the monolithic perovskite/silicon tandem solar cell architecture incorporating 2PACz and Ph-2PACz as HTLs. (b) Molecular structures of PTAA, 2PACz, and Ph-2PACz. (c) Electrostatic potential maps highlighting the charge distribution of the respective HTL molecules. (d) J–V characteristics and thermal cycling stability of tandem devices based on different HTLs. (e) Energy level alignment diagrams of PTAA, 2PACz, Ph-2PACz, and perovskite layers. (f) Normalized absorption spectra of the corresponding HTLs. Reproduced with permission from ref. 182, Copyright 2022, Elsevier Inc.

strategic engineering of the hole-selective contact using a blend of two carbazole-based SAMs: MeO-2PACz and 2PACz.[181] MeO-2PACz, while commonly used, was found to leave certain regions of the ITO substrate insufficiently covered, leading to suboptimal passivation. To address this, 2PACz known for its superior passivation capability and structural compatibility was introduced as a co-SAM. By blending the two molecules, the researchers achieved a more complete and uniform surface coverage, compensating for the uncovered areas left by MeO-2PACz alone. Advanced characterization techniques such as XPS, cyclic voltammetry, and impedance spectroscopy confirmed the improved interfacial properties of the blended SAM system. This optimized SAM interface considerably reduced interfacial recombination losses, enhanced charge extraction, and contributed to better energy alignment at the ITO/perovskite interface. As a result, the tandem solar cell incorporating the mixed SAMs achieved an impressive power conversion efficiency of 28.8%, underscoring the critical role of tailored SAM formulations in advancing tandem device performance.

Building on the foundational design of (2-(3,6-diphenyl-9H-carbazol-9-yl)ethyl)phosphonic acid (Ph-2PACz), Wang et al. developed an advanced carbazole-based SAM with an extended conjugated system incorporating two phenyl rings.[182] This structural enhancement was specifically engineered to improve interfacial alignment and performance in high-bandgap PSCs, particularly those intended for tandem architectures using multiple-cation perovskites. The modified SAM exhibited a better-aligned HOMO level with the perovskite VBM, minimizing energetic mismatches and improving hole extraction efficiency as shown in Fig. 26.

In addition to favorable energy level alignment, the SAM demonstrated enhanced surface wettability, which facilitated high-quality perovskite film formation and reduced interfacial defects. These combined effects led to an optimized perovskite/HTL interface and faster charge extraction. In device applications, the Ph-2PACz SAM enabled a p–i–n single-junction PSC (1.67 eV bandgap) to reach a PCE of 21.3% with a high V_{OC} of 1.26 V and FF of 82.6%. When integrated into monolithic perovskite/silicon tandem cells, the improved interface quality contributed to a PCE of 28.9% and a V_{OC} of 1.91 V. Moreover, the encapsulated tandem devices displayed excellent operational stability, maintaining performance under prolonged illumination (680 hours) and elevated humidity and temperature conditions (85 °C for 280 hours), emphasizing the reliability and practical potential of the enhanced SAM strategy for tandem photovoltaics. Albrecht and Tan et al.[183] both reported notable advancements in monolithic and 4T perovskite–silicon TSCs, with a shared emphasis on interface engineering using SAMs to enhance device performance and stability. In Albrecht's study, the integration of Me-4PACz SAM as a hole-selective contact in WBG (1.68 eV) perovskite top cells played a critical role in achieving a certified PCE of 29.15%.[44] The SAM enabled rapid hole extraction and substantially reduced non-radiative recombination at the perovskite/HTL interface, key factors contributing to a high $V_{OC} = 1.92$ V and an exceptional FF = 84% in the tandem configuration as depicted in Fig. 27.

These performance enhancements were supported by a low ideality factor of 1.26, indicative of suppressed trap-assisted recombination. Notably, the TSC maintained 95% of its original efficiency after 300 hours of exposure to ambient air, despite the absence of encapsulation, underscoring the stabilizing role of the SAM-modified interface.

Tan et al. introduced a complementary approach named Grain Regeneration and Bilateral Passivation (GRBP) to address recombination at both grain boundaries and perovskite/contact interfaces.[183] This method involved post-treatment with MASCN to regenerate the grain structure and PEAI to infiltrate and passivate buried interfaces. The perovskite top cells were fabricated using MeO-2PACz, another carbazole-based SAM, as the HTL. This layer enhanced interfacial alignment and supported efficient charge extraction. Devices treated with GRBP achieved PCEs of 21.9% (opaque) and 19.9% (semi-transparent) and retained high stability under 500 hours of continuous illumination. Importantly, when the optimized perovskite top cells were integrated into 4T tandem configurations, they achieved record-breaking efficiencies of 29.8% (0.09 cm²) and 28.5% (1 cm²). The use of MeO-2PACz contributed to improved interfacial energetics and wettability, leading to high-quality film formation and efficient hole collection.

In their work, Chin et al. demonstrated a dual-passivation strategy to minimize voltage losses at both the HTL and ETL interfaces.[184] Me-4PACz was employed as the HTL modifier, which due to its strong anchoring on indium tin oxide (ITO) and favorable energy-level alignment effectively suppressed non-radiative recombination at the perovskite/HTL interface, thereby improving V_{OC}. To address interface defects on the ETL side, 2,3,4,5,6-pentafluorobenzenephosphonic acid (FBPAc) was added into the perovskite precursor. FBPAc, a small molecule with a strong electron-withdrawing fluorinated phenyl group, was found to passivate surface defects during crystal growth, particularly at the perovskite/C₆₀ interface. This dual-side treatment led to an improved film microstructure and reduced interfacial trap density. Additionally, by conformally coating the perovskite layer onto micron-sized silicon pyramids, the optical path was enhanced, boosting photocurrent. These synergistic interfacial optimizations resulted in a certified PCE of 31.25% (active area: 1.17 cm²), establishing a new benchmark in tandem device performance.

Mariotti et al., in a separate study, emphasized a multilayered strategy for recombination loss mitigation and charge extraction improvement.[185] They incorporated Me-4PACz as the HTL to ensure efficient hole extraction and stable perovskite/HTL contact as illustrated in Fig. 28. This SAM not only provided optimal energy-level alignment with the perovskite VB but also improved surface wettability, ensuring high-quality film deposition. Additionally, pyridine iodide was used to modify the triple-halide perovskite absorber, fine-tuning the CB alignment at the ETL interface and reducing non-radiative recombination at the electron-selective contact. The fabrication process was further enhanced by additive engineering to promote better film morphology. Together, these enhancements yielded an exceptionally high V_{OC} of 2.00 V and a certified PCE of 32.5%, one of the highest reported for monolithic TSCs.
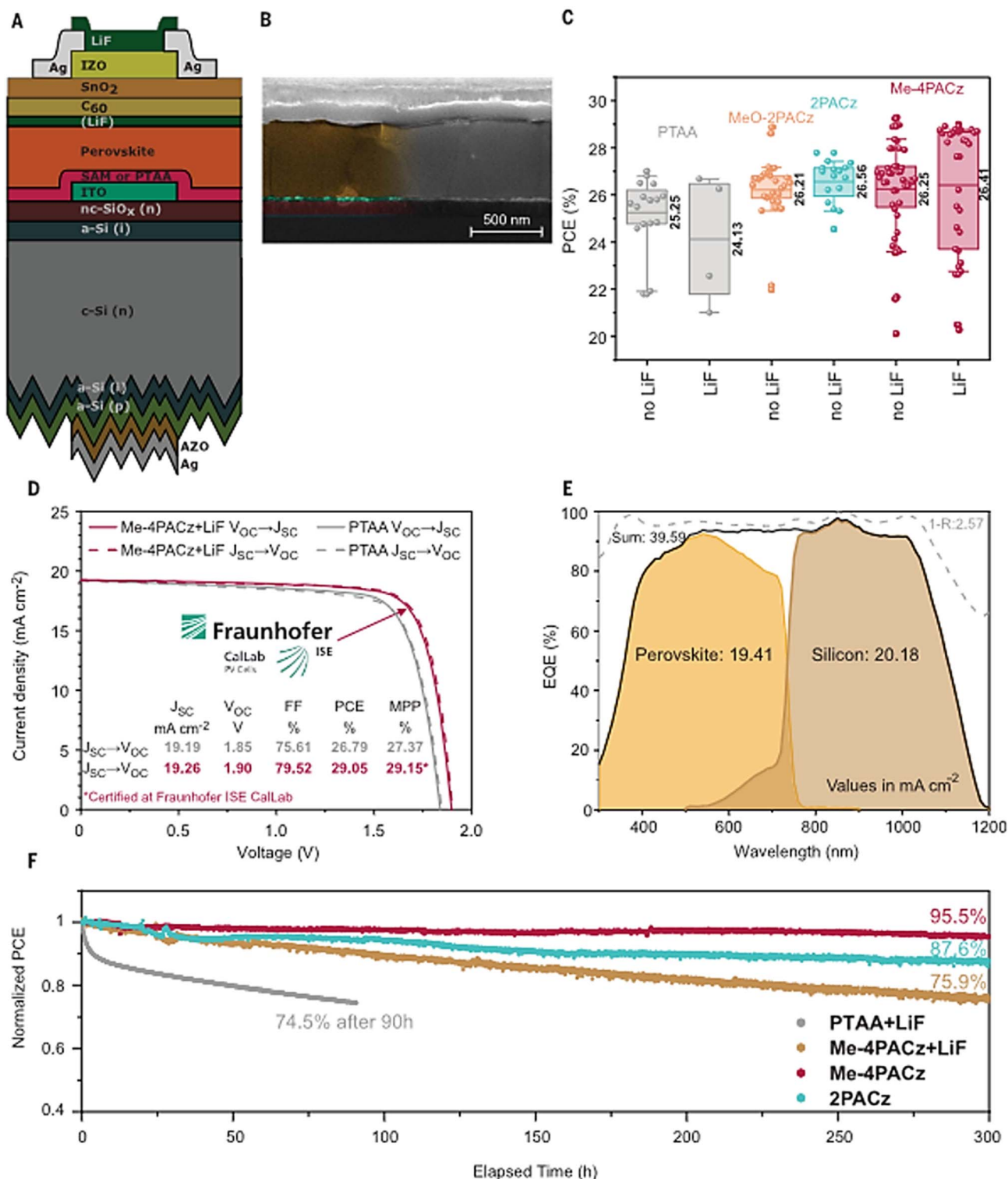
Fig. 27 Device architecture, cross-sectional morphology, photovoltaic performance, and stability of perovskite/silicon tandem solar cells incorporating Me-4PACz and 2PACz SAM-modified HTLs with and without LiF interlayers. (A) Schematic device structure, (B) cross-sectional SEM image, (C) PCE statistics, (D) J–V characteristics, (E) EQE spectra, and (F) operational stability under continuous illumination. Reproduced with permission from ref. 44, Copyright 2020, The American Association for the Advancement of Science.

While other perovskite–silicon TSCs have achieved higher efficiencies, such as JinkoSolar's 33.84% and Longi's 34.6%, these records do not specify the use of SAMs in their device architectures.[186,187] Therefore, the 32.5% efficiency reported by Mariotti *et al.* currently stands as the highest for TSCs explicitly incorporating SAM modification.
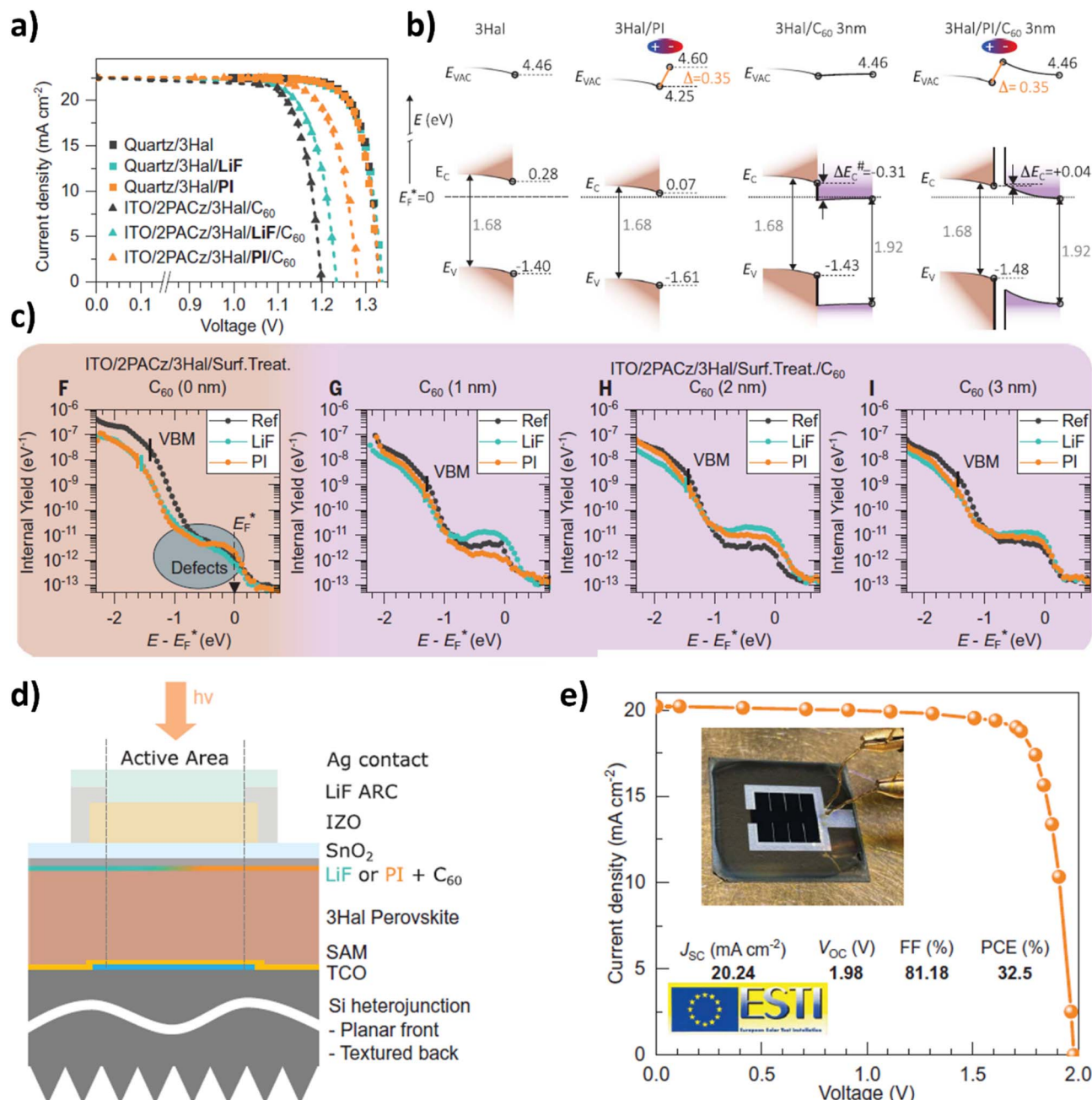
Fig. 28 Interfacial dipole modification of the 3Hal perovskite/C_{60} contact for improved charge extraction. (a) $J-V$ characteristics comparing 3Hal-based devices on quartz and ITO/2PACz with LiF or PI interlayers, with and without C_{60}. (b) Schematic energy level diagrams showing dipole-induced shifts at the 3Hal/PI interface and resulting band alignment changes across C_{60} thicknesses. (c) Internal photoemission yield spectra (IPEY) for devices with varying C_{60} thickness (0–3 nm), indicating changes in interfacial valence band position and defect-associated states. (d) Device architecture of the monolithic perovskite/Si tandem incorporating SAM and interfacial dipole layers. (e) $J-V$ curve and certified PCE of the optimized tandem device. Reproduced with permission from ref. 185, Copyright 2023, The American Association for the Advancement of Science.

From the same group, Harter *et al.* demonstrated certified PCE exceeding 30% in monolithic perovskite/silicon TSCs fabricated on submicron-textured, industry-standard silicon bottom cells.[188] A key enabler of this performance milestone was the strategic incorporation of a multifunctional SAM derived from Me-4PACz, with an additional phosphonic acid (PA) with different functional groups as illustrated in Fig. 29. Utilizing

this SAM-based HTL led to markedly improved perovskite film morphology by enhancing surface wettability, reducing parasitic shunting, and mitigating interfacial non-radiative recombination losses.

Characterization *via* transient surface photovoltage and transient photoluminescence revealed that the combined Me-4PACz/phosphonic acid (PA) interface retained efficient charge
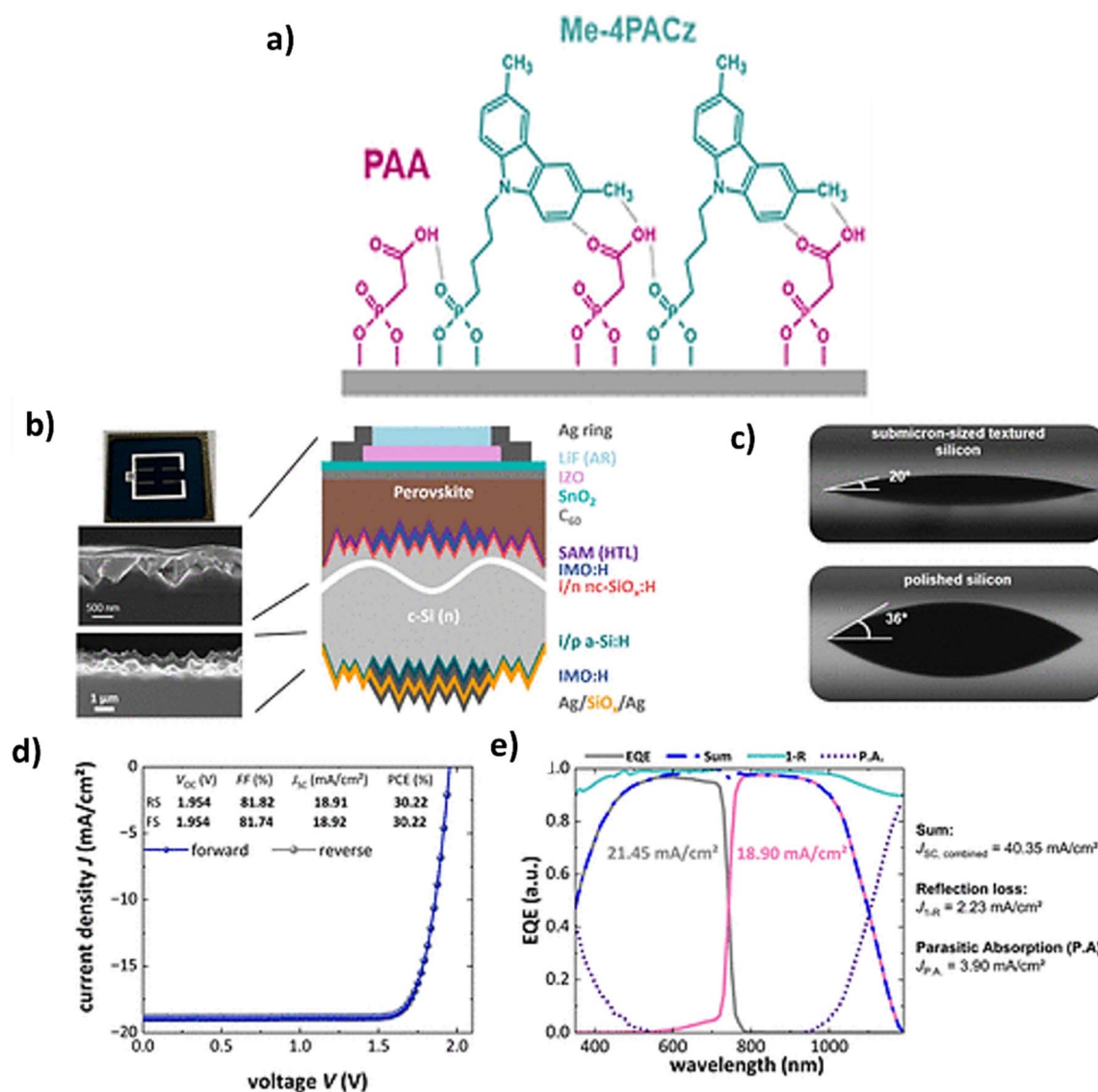
Fig. 29 (a) Molecular structures of SAMs (Me-4PACz and PAA), (b) device architecture with submicron-textured silicon, (c) contact angle measurement on textured and polished silicon (d) photovoltaic performance of perovskite/Si tandem solar cells and (e) EQE measurements of champion device. Reproduced from ref. 188, under a Creative Commons CC BY 4.0 license. Copyright 2024 American Chemical Society.

transport characteristics similar to pristine Me-4PACz. These interface optimizations enabled the device to deliver a high J_{SC} of 40.2 mA cm^{-2}, achieve an FF above 82%, and attain V_{OC} near the radiative efficiency limit—collectively resulting in a stabilized PCE exceeding 30%. Compared to earlier SAM-based interface engineering approaches many of which were limited to planar substrates or yielded modest improvements in device metrics the use of Me-4PACz on textured silicon surfaces represents a substantial advancement, demonstrating that judicious molecular design and interfacial tailoring can simultaneously optimize charge selectivity, film formation, and energetics in complex tandem architectures. Kore *et al.* took this forward by presenting a strategically distinct interface engineering approach that enabled the successful integration of thermally evaporated HTLs onto fully textured silicon bottom

cells, a notoriously challenging configuration due to surface roughness and interfacial discontinuities.[189] Central to this advancement was the use of a MeO-2PACz SAM on ITO, which acted as a multifunctional interfacial modifier. Unlike prior studies that largely relied on solution-processed HTLs (*e.g.*, PTAA or spin-coated MeO-2PACz layers), this study pioneered a vacuum-compatible route using TaTm as the evaporated HTL as shown in Fig. 30. The SAM ensured favorable energy level alignment, suppression of interfacial recombination, and enhanced wetting and growth morphology of the evaporated layer – the challenges that conventional methods often failed to address effectively on textured substrates. This tailored SAM–HTL interface led to tandem devices with reduced voltage losses and a remarkably high FF, achieving a certified PCE of 29.2%
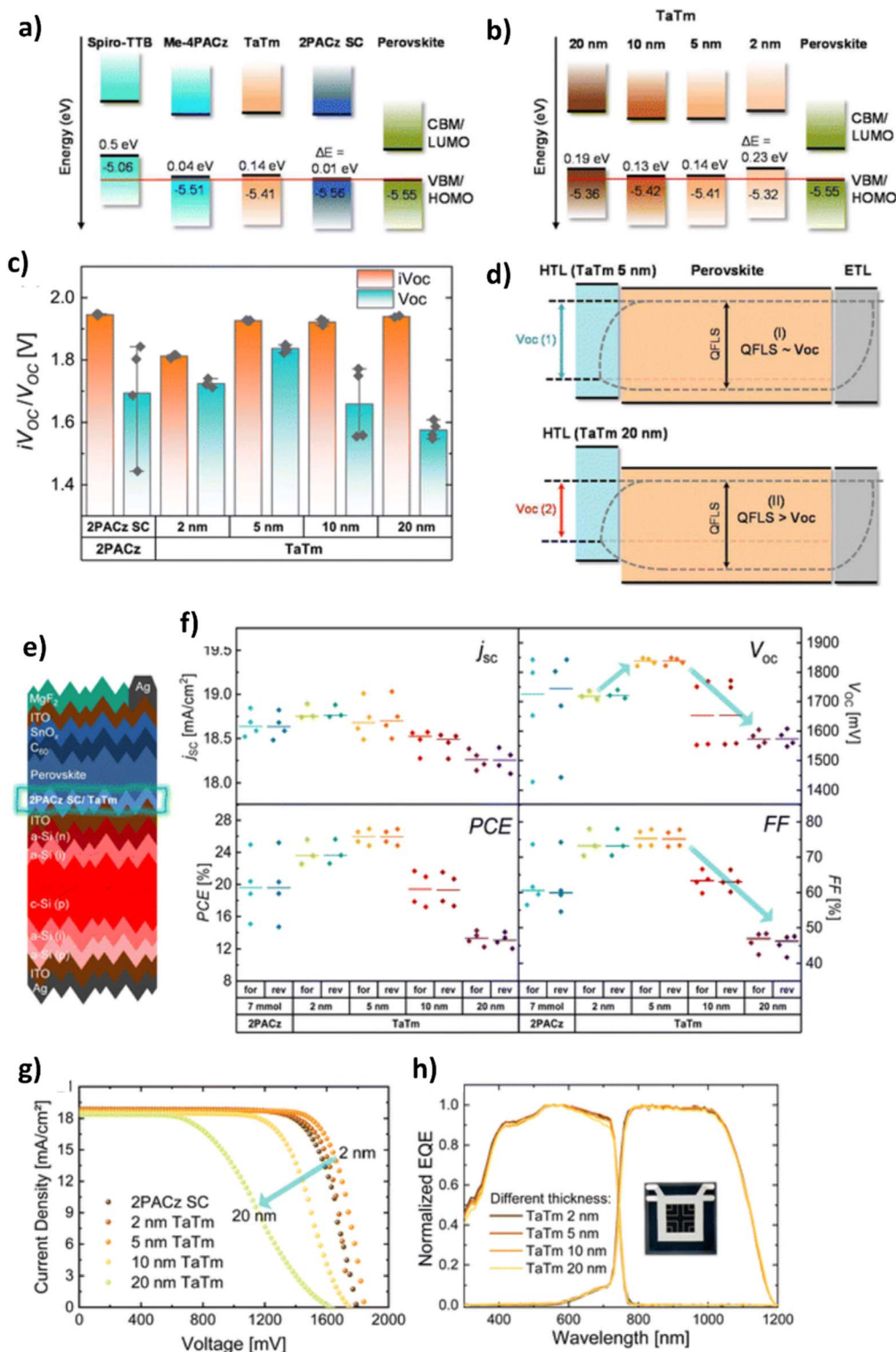
Fig. 30 Energy level alignment, device architecture, and photovoltaic performance of perovskite solar cells with varying TaTm interlayer thicknesses. (a and b) Energy level diagrams of different HTLs and TaTm with varying thicknesses. (c) Ratio of IOC/VOC for devices with different TaTm thicknesses. (d) Schematic illustration of quasi-Fermi level splitting and VOC for thin (5 nm) and thick (20 nm) TaTm layers. (e) Schematic cross-section of the tandem device architecture. (f) Photovoltaic parameters as a function of TaTm thickness. (g) Current density–voltage characteristics. (h) Normalized EQE spectra for devices with different TaTm thicknesses. Reproduced from ref. 189, under a Creative Commons 3.0 Licence. Copyright 2025, Royal Society of Chemistry.
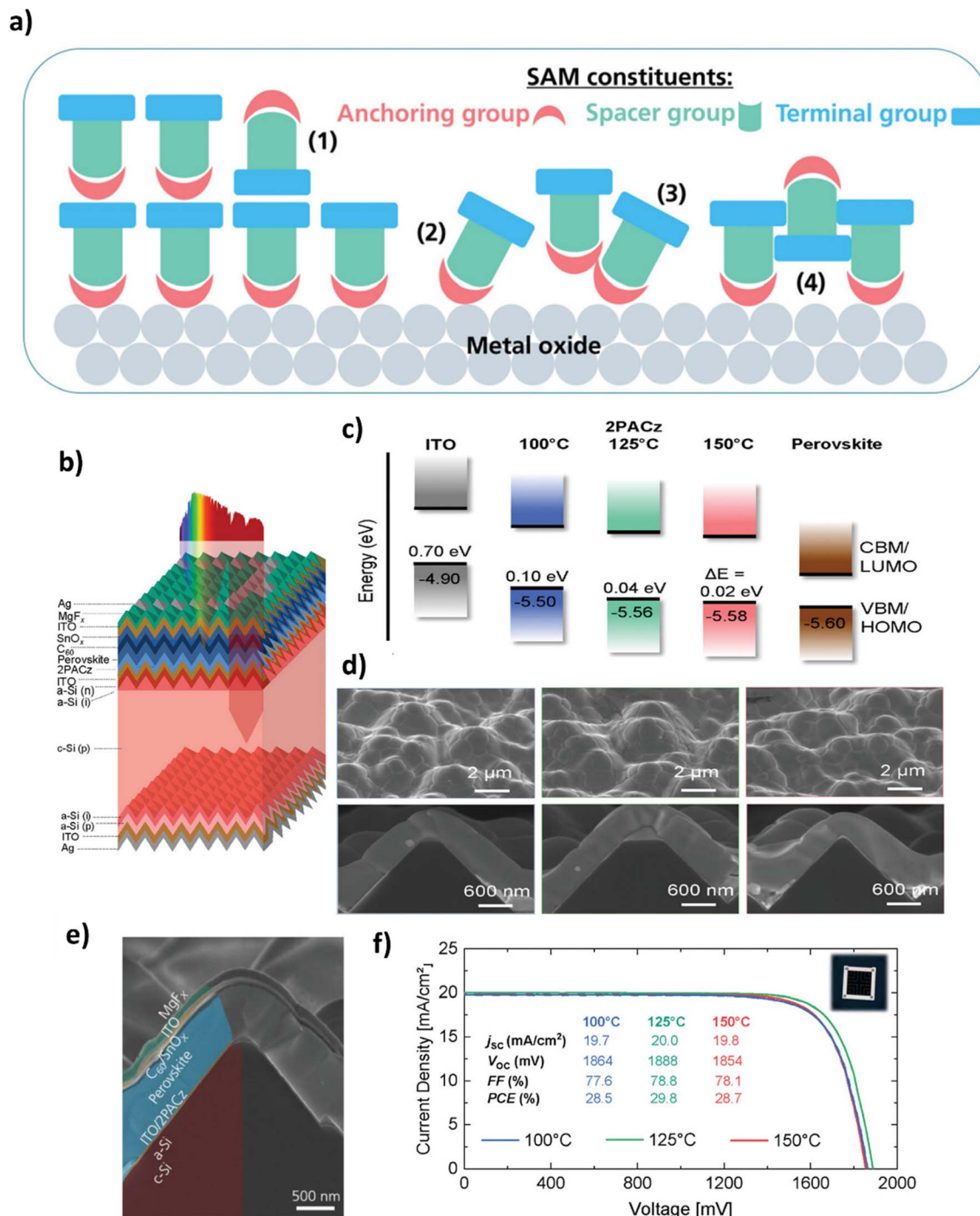
Fig. 31 Thermal processing effects on SAM packing, interfacial energetics, and tandem device performance. (a) Schematic illustration of SAM anchoring, packing, and tilt configurations on metal-oxide surfaces. (b) Layered device architecture of the monolithic perovskite/silicon tandem stack incorporating a 2PACz-based HTL. (c) Work-function tuning and interfacial energy alignment of 2PACz on ITO as a function of annealing temperature. (d) Top- and cross-sectional SEM images of perovskite films deposited on 2PACz-treated substrates under different thermal treatments. (e) Cross-sectional SEM of the complete textured c-Si/perovskite tandem device with the 2PACz interface layer. (f) J–V characteristics of tandem devices fabricated at 100 °C, 125 °C, and 150 °C, with corresponding performance metrics. Reproduced with permission from ref. 191 and 192 Copyright 2020, American Chemical Society, Copyright 2025 Wiley-VCH GmbH.

among the highest reported for monolithic tandems employing evaporated layers.

Importantly, the work demonstrated that the performance of vacuum-deposited interfaces can match or surpass the

performance of solution-processed counterparts when guided by precise molecular interface design. It also opened the door for scalable, industry-compatible tandem fabrication strategies that are less constrained by the processing limitations of spin-

coated HTLs. In this context, the SAM is not merely a passive dipole modifier but a key enabler of structural and electronic coherence across rough, multi-material junctions offering a new paradigm for hybrid interface engineering in next-generation tandem photovoltaics. On a slightly different approach, Zhang *et al.* demonstrated an effective buried-interface SAM in an n–i–p tandem architecture, which remained a relatively underexplored and technically challenging domain due to wetting, deposition, and interfacial contact issues.[190] The authors effectively incorporated a SAM of fullerene (C_{60}), featuring a large monovalent organic cation, at the interface. This SAM considerably enhanced the surface conductivity of the NbO_x ETL, mitigating interface recombination and reducing the energetic mismatch with the perovskite layer. Unlike traditional methods that primarily focussed on bulk material modifications or simple surface passivation, the fullerene SAM in this study improved both electronic properties and morphology, resulting in enhanced electron extraction and reduced device hysteresis. The TSCs achieved a remarkable efficiency of 27% (over 1 cm^2) with a V_{OC} of 1.9 V, demonstrating substantial performance gains compared to other state-of-the-art perovskite/silicon tandem devices.

In the most recent advancement in the area, Er-Raji *et al.* unveiled a sophisticated interface engineering strategy, centered on the modulation of SAMs to enhance the performance and reproducibility of monolithic perovskite/silicon TSCs.[191] The study meticulously examined the formation dynamics and interfacial impact of MeO-2PACz as a hole-selective contact. Crucially, the authors demonstrated that the molecular assembly and consequently the interfacial energetics are highly sensitive to the SAM deposition conditions, such as solution concentration, solvent polarity, and immersion time as is evident from Fig. 31.

Poorly optimized deposition results in inhomogeneous coverage and dipolar disorder, which in turn compromise energy level alignment and perovskite film formation. To overcome this, the authors introduced a bilayer assembly protocol, where a sub-monolayer of PACz, possessing a shorter molecular backbone, was first adsorbed onto a silicon oxide substrate. This prestructuring primes the surface, enabling a more ordered and densely packed MeO-2PACz overlayer. Spectroscopic ellipsometry, contact angle measurements, and ultraviolet photoelectron spectroscopy (UPS) collectively confirm improved molecular orientation and increased SAM dipole density, leading to better-defined energy level alignment with the perovskite absorber. From a device standpoint, this improved SAM interface translated to notable enhancements: the TSCs exhibited a reduction in interfacial non-radiative recombination losses, higher V_{OC}, and greater operational stability. Importantly, the bilayer SAM treatment addressed a persistent challenge in hybrid TSC batch-to-batch variability by decoupling the effects of solvent-induced disorder and adsorption kinetics. This work exemplified how molecular-scale engineering of contact interfaces *via* SAMs can be leveraged not only to optimize energetics but also to enforce reproducibility, a critical requirement for the commercialization of perovskite-based tandem photovoltaics. Compared to conventional SAM strategies employed in PSCs, this approach stands out for its specific focus on controlling the self-assembly process itself, rather than merely selecting a SAM with a favorable head group or dipole orientation. Most existing studies utilize SAMs like MeO-2PACz or PTAA in single-step deposition protocols, where the emphasis is often placed on the molecular design *e.g.*, introducing electron-donating or -withdrawing substituents to tune the WF alignment with the perovskite absorber. While such strategies have yielded reasonable success, they often suffer from issues of interfacial disorder, poor reproducibility, and limited control over molecular packing density – the factors that critically influence charge extraction and recombination kinetics. While traditional methods emphasize molecular design for energy level tuning, they often suffer from inhomogeneous coverage and solvent-induced disorder. In contrast, pre-functionalizing the substrate with a shorter PACz molecule enabled more controlled adsorption of MeO-2PACz, leading to denser packing, better dipolar alignment, and reduced interfacial trap states. Thus this hierarchical strategy decoupled substrate and perovskite interface optimization, mitigating non-radiative losses and improving device uniformity offering a process-integrated pathway that goes beyond passive SAM roles toward deterministic interface engineering in scalable tandem photovoltaics.

5.2.3 Critical analysis of SAM molecules in perovskite solar cells.
A critical evaluation of commonly used SAM molecules demonstrates that small structural modifications, including head-group chemistry, tail-group substitution, and molecular length, can significantly influence device performance and stability.

5.2.3.1 Energy-level alignment and dipole effects. The molecular dipole of a SAM directly modulates the vacuum level at the perovskite/SAM interface, affecting the built-in potential and V_{OC}. Methoxy-functionalized carbazole SAMs, such as MeO-2PACz, induce a stronger upward dipole shift compared to 2PACz, improving hole extraction and V_{OC}. The enhanced dipole effect of MeO-2PACz relative to 2PACz originates from the methoxy group ($-OCH_3$), an electron-donating substituent that increases electron density on the carbazole unit. When the molecule self-assembles on the substrate, this redistribution of charge strengthens the permanent dipole moment oriented from the phosphonic acid anchor toward the carbazole moiety, thereby producing a stronger upward vacuum-level shift.[193] This shift elevates the substrate WF, aligns it more favorably with the perovskite valence band, and consequently facilitates more efficient hole extraction and higher V_{OC}. In contrast, 2PACz provides a more modest interfacial dipole and hence moderate energy-level alignment, but supports high intrinsic hole mobility owing to efficient π-conjugation and dense molecular packing, ensuring low energetic disorder at the interface. Extending the alkyl tether, as in 4PACz, reduces packing density and introduces minor local variations in vacuum-level alignment. However, this increased molecular flexibility can facilitate improved film morphology and defect passivation during perovskite growth, offering a practical balance between energetic uniformity and large-area process compatibility.[194] On the other hand, novel carbazole derivatives, including BCBBr-C4PA

and 4PADCB, introduce extended π-conjugation or brominated substituents that further tune interfacial dipoles. BCBBr-C4PA, with a brominated benzo[c]carbazole core, increases interfacial dipole magnitude and improves energy-level alignment, while 4PADCB, featuring a planar dibenzo[c,g]carbazole core, offers strong π–π interactions and moderate dipole effects suitable for efficient hole extraction. BCBBr-C4PA leverages the electron-withdrawing effect of bromine on a benzo[c]carbazole core to strengthen the interfacial dipole moment, producing a pronounced upward vacuum-level shift and improved energy-level alignment for hole extraction, while simultaneously enhancing passivation through halogen-induced stabilization. In contrast, 4PADCB, with its planar dibenzo[c,g]carbazole core, promotes strong π–π stacking, dense monolayer formation, and excellent trap passivation. Although its intrinsic dipole strength is more moderate, this balanced electronic and structural behavior ensures efficient hole extraction, robust perovskite crystallization, and outstanding interfacial stability.[195]

5.2.3.2 Interfacial trap passivation. The functional head group chemistry determines the ability of SAMs to bind undercoordinated Pb^{2+} or halide ions at the perovskite surface. Phosphonic acid-based SAMs (2PACz, MeO-2PACz, 4PACz, BCBBr-C4PA, and 4PADCB) exhibit strong chemisorption to the oxide/hybrid perovskite surface *via* tridentate, bidentate, or hydrogen-bond-assisted coordination. This robust binding reduces the density of surface trap states, in turn lowering trap-assisted recombination, increasing the QFLS and directly improving the V_{OC} and non-radiative loss factor (ΔV_{nr}). Beyond anchoring strength, the π-conjugated cores of SAM molecules mediate additional passivation through electronic interactions with the perovskite frontier orbitals (predominantly Pb 6p and halide np states near the valence/conduction band edges).[196] For instance, 4PADCB, with its dibenzo[c,g]carbazole planar extended π-system, exhibits strong π–π stacking and enhanced orbital overlap with the Pb-halide surface. This delocalization provides two synergistic effects: (i) better charge delocalization across the interface, lowering interfacial resistance and improving hole transfer, and (ii) stabilization of shallow surface states, which suppresses recombination *via* defect-assisted channels. The planarization also enhances molecular ordering, reducing energetic disorder, which benefits charge transport uniformity. BCBBr-C4PA, in contrast, introduces a bromine substituent on the benzo[c]carbazole core. The bromine atom is highly polarizable and electron-withdrawing, which increases the interfacial dipole moment ($\Delta\mu$) *via* inductive and resonance effects. This results in a more pronounced vacuum-level shift (ΔE_{vac}) at the interface, fine-tuning the alignment between the perovskite VBM and the SAM HOMO level. Simultaneously, the bromine substituent enhances electrostatic passivation of undercoordinated Pb^{2+} by partial halogen–metal interactions, effectively mimicking halide compensation. This dual mechanism (dipole tuning + orbital overlap) yields stronger suppression of surface recombination velocities. In comparison, simpler carbazole-based SAMs (2PACz, 4PACz, and MeO-2PACz) primarily rely on phosphonic anchoring and carbazole π-interactions for passivation. While they effectively reduce trap density, their dipole magnitude and

orbital overlap effects are comparatively moderate. Notably, MeO-2PACz benefits from electron-donating methoxy substitution, which increases the electron density on the carbazole ring, strengthening π-donor interactions with Pb orbitals, thereby enhancing passivation relative to unsubstituted 2PACz. Overall, the hierarchy of passivation efficacy stems from a balance between

(1) chemical passivation (strength of Pb–O–P bonds from phosphonic acids),

(2) electrostatic tuning (molecular dipole magnitude and orientation), and

(3) electronic delocalization (π–π interactions and orbital overlap).

The synergistic interplay of these mechanisms underpins their role in suppressing non-radiative interfacial recombination, stabilizing perovskite energetics, and enabling efficient hole extraction.

5.2.3.3 Surface coverage, morphology, and wettability. Molecular packing and uniform coverage are critical for minimizing pinholes and ensuring homogeneous interfacial energetics. The structural and chemical diversity of SAM molecules directly governs their packing density, surface energy, and consequently the nucleation and growth of perovskite films. Methoxy-functionalized carbazole SAMs such as MeO-2PACz form dense, highly ordered monolayers due to strong anchoring and compact aromatic packing, while their polar methoxy substituents enhance wettability, leading to high nucleation density and uniform grain growth. In contrast, 4PACz, with its longer alkyl tether, exhibits slightly reduced packing density and increased conformational disorder, introducing minor local energetic inhomogeneities but often facilitating smoother large-area film formation. BCBBr-C4PA, bearing a bulky brominated benzo[c]carbazole core, poses challenges for close packing and requires optimized deposition to achieve full surface coverage; however, once ordered, its high polarizability improves interfacial smoothness and stabilizes perovskite growth. Meanwhile, the highly planar dibenzo[c,g]carbazole backbone of 4PADCB promotes strong π–π stacking and lateral order, yielding monolayers with excellent coverage and surface wettability that guide uniform crystallization. Collectively, these comparisons highlight how subtle variations in molecular design such as tail length, substituent polarity, steric bulk, and backbone planarity critically influence perovskite film morphology and interface quality.

5.2.3.4 Operational stability. Under operational stressors such as heat, humidity, and illumination, distinct trade-offs emerge among different SAM molecules due to variations in anchoring strength, conjugation, and substituent chemistry. MeO-2PACz exhibits superior stability, with its strong phosphonic acid anchoring and electron-donating methoxy substituents maintaining both the interfacial dipole and chemical bonding under prolonged light soaking and thermal stress. By contrast, 2PACz and 4PACz, while still forming stable P–O–Pb linkages, show moderate resistance, as their less polar substituents render the interfacial dipole more susceptible to partial relaxation and moisture-induced disorder. Incorporation of bromine into the benzo[c]carbazole backbone in BCBBr-C4PA

Table 3 Critical comparison of varied SAM molecules for perovskite interface modification

Parameter	2PACz	MeO-2PACz	4PACz	BCBBr-C4PA	4PADCB
Tail/head group	Phosphonic acid (head) and carbazole (tail)	Phosphonic acid (head) and methoxy-carbazole (tail)	Phosphonic acid (head) and a longer alkyl-carbazole tail	Phosphonic acid (head) and brominated benzo[c]carbazole	Phosphonic acid (head) and dibenzo[c,g]carbazole
Dipole effect & energy alignment	Moderate dipole; favorable hole extraction; moderate V_{OC}	Strong upward dipole; improved energy alignment	Moderate dipole; good energy alignment	Strong dipole; improved energy-level alignment	Moderate dipole; planar conjugation improves hole extraction
Passivation strength	Strong; binds undercoordinated Pb^{2+} ions	Strong; effective trap passivation	Strong; comparable to 2PACz	Strong; bromination enhances electronic passivation	Strong; extended π-conjugation enhances passivation
Packing density	High; uniform monolayer	Very high; dense packing	Moderate	Moderate to high; packing optimization required	High; an ordered monolayer
Processing compatibility	Good wettability	Excellent wettability	Improves morphology; optimization needed	Promotes smooth perovskite crystallization	Excellent wettability
Stability under stress	Moderate; stable under short-term stress	High; maintains dipole and binding	Moderate; comparable to 2PACz	High; the brominated core enhances thermal and chemical stability	Very high; the rigid planar structure ensures robustness
Performance trade-offs	High initial FF and mobility and slightly lower V_{OC}	Slightly lower FF; higher V_{OC} and better stability	Balances morphology and energetics; slightly lower reproducibility	Strong dipole and passivation; requires careful packing	Excellent stability, good morphology, and balanced energetics

enhances molecular stability by reducing photooxidation and suppressing bond cleavage pathways through the heavy-atom effect, thereby prolonging interfacial dipole retention. Meanwhile, the rigid, highly conjugated backbone of 4PADCB confers exceptional thermal and photostability, as its extended π-system and planar packing minimize conformational disorder and resist structural degradation. These comparative insights underscore how molecular rigidity, electronic substituents, and anchoring strength govern SAM resilience under device-relevant stress conditions, directly impacting long-term perovskite solar cell stability.

5.2.3.5 Performance trade-offs. The performance of SAM-modified perovskite interfaces reflects a delicate balance between energy-level alignment, trap passivation, film morphology, and operational stability, with each molecular design offering distinct advantages and trade-offs. 2PACz provides high initial fill factors and efficient hole transport owing to its favorable intrinsic mobility, though its stability is moderate. MeO-2PACz enhances both V_{OC} and long-term durability by combining strong dipole-induced energy-level tuning with robust interfacial binding. 4PACz, featuring a longer alkyl spacer, slightly compromises packing density but promotes smoother large-area film formation and improved morphological uniformity. BCBBr-C4PA, while requiring careful optimization to overcome steric constraints, introduces a stronger interfacial dipole and enhanced electronic passivation through bromination, thereby improving energy alignment and recombination suppression. 4PADCB, with its rigid, planar dibenzo[c,g]carbazole core, achieves highly ordered monolayer formation that simultaneously delivers excellent defect passivation and outstanding thermal and photostability. Collectively, these comparisons highlight that the rational design of SAM head- and tail-group chemistries is crucial for achieving the optimal compromise between efficiency, stability, and scalability in perovskite solar cells (Table 3).

5.3. Interface engineering using dipole tailored interlayers

The polycrystalline nature of perovskite films inherently leads to trap states at grain boundaries and within the bulk, which act as recombination centers and impair device efficiency, stability, and reproducibility. Suppressing charge trapping is thus critical for advancing PSC performance. While external reverse bias has been shown in polymer solar cells to enhance carrier extraction by generating strong internal electric fields (E_{in}), applying such fields within operational PSCs remains impractical. Enhancing E_{in} intrinsically using interlayers tailored to meet the interface dipole requirements within the device is therefore essential. At this juncture, it is worth mentioning that while such dipolar modifications have been extensively explored in single-junction PSCs, their application in more complex device architectures such as TSCs has remained largely unexplored until recently. It was only quite recently, in 2024, that the group led by Anita Ho-Baillie[205] demonstrated the use of dipole-tailored interlayers in perovskite-based TSCs, marking a pivotal advancement in extending this strategy beyond single-junction devices. We begin by highlighting key milestones and fundamental insights
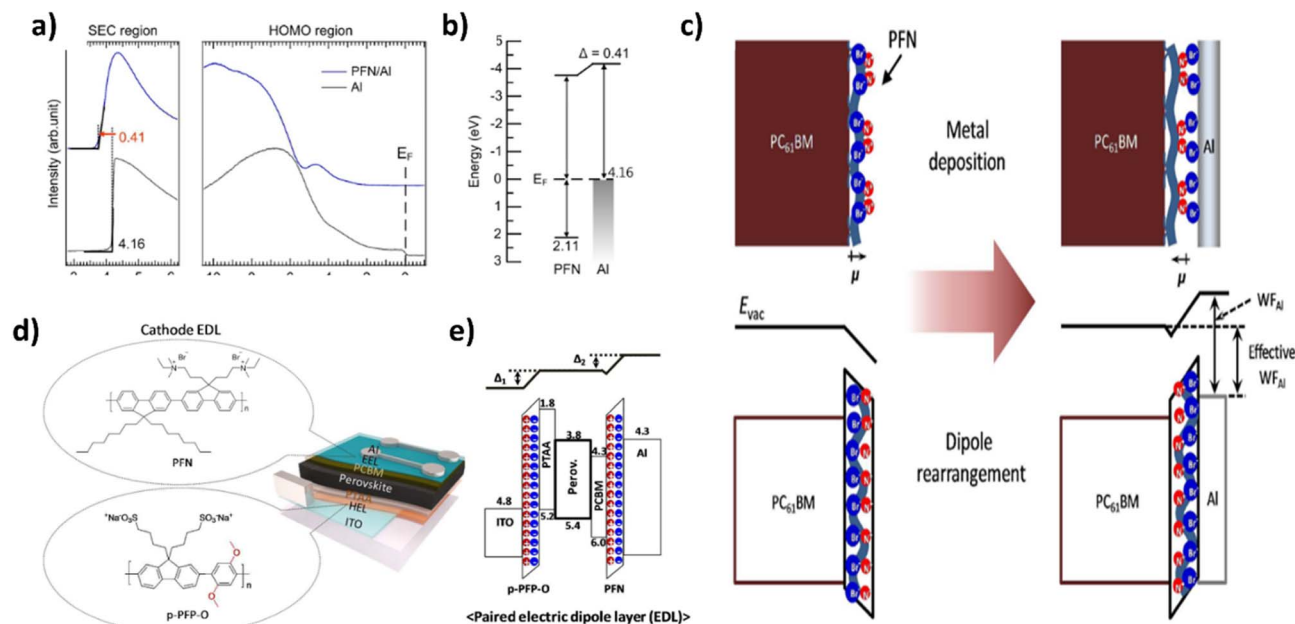
Fig. 32 Paired electric dipole layer (EDL) engineering at the $PC_{61}BM$/metal contact for controlled work-function modulation. (a) UPS spectra comparing PFN/Al and bare Al interfaces. (b) Energy-level diagram showing the work-function shift induced by PFN. (c) Schematic illustration of dipole orientation before and after metal deposition and the resulting effective work-function change. (d) Chemical structures of PFN and p-PFP-O forming cathode EDLs, and device architecture. (e) Band alignment and interfacial dipole configuration demonstrating paired EDL formation at both ITO and Al interfaces. Reproduced with permission from ref. 197, Copyright 2018, Royal Society of Chemistry.

gained from studies on single-junction PSCs, which have laid the groundwork for interface dipole engineering. Building on this foundation, we then delve into the emerging application of dipole-tailored interlayers in tandem solar cells, exploring their implications for advancing multi-junction device performance.

The pioneering study on employing dipole tailored interlayers was done by Lee *et al.* who introduced a dual-dipole-layer architecture to attenuate the built-in electric field (E_{in}) across p–i–n planar PSCs and thereby suppress charge trapping at grain-boundary and bulk defects.[197] By inserting a p-doped conjugated polyelectrolyte (p-PFP-O) as a hole-extraction dipole layer at the ITO/anode interface and a dipolar fullerene derivative (PFN) at the cathode/$PC_{61}BM$ junction, they shifted each electrode's vacuum level by ± 0.6 eV, increasing the electrode work-function difference and thus E_{in} as depicted in Fig. 32.

Ultraviolet photoelectron spectroscopy (UPS) and contact potential difference (CPD) measurements were instrumental in elucidating the interfacial energetics and dipole behavior in the devices, particularly in the context of metal–organic junctions. At the PFN/Al interface, UPS revealed an upward shift in the vacuum energy level (E_{vac}), indicating the formation of new electric dipoles with anions oriented toward the Al electrode. This reorientation was attributed to strong interactions between the thin (~ 5 nm) PFN layer and diffusing metal atoms during electrode deposition. Similar trends observed for the Au/PFN interface supported the idea that metal contact can induce considerable dipole rearrangement, effectively modifying the metal WF and enhancing the E_{in} across the device *via* paired electrical double layers (EDLs). CPD studies on PTAA films further illustrated the influence of interlayers in tuning energy

alignment. While PTAA on ITO showed an increased CPD due to Fermi level mismatch, the introduction of PEDOT:PSS or p-PFP-O led to a negative shift in surface potential, indicating hole accumulation in PTAA driven by the interlayers' self-aligned surface dipoles. Notably, p-PFP-O induced a stronger Fermi level shift than PEDOT:PSS, emphasizing the importance of dipole engineering at interfaces for improved charge transport and device efficiency. Schematic illustration of trap-assisted charge recombination in PI(N) junctions and its modulation by electric double layers (EDLs) is illustrated in Fig. 33.

Devices incorporating both dipole layers achieved a champion power-conversion efficiency of 19.4% (*versus* 17.8% with conventional PEDOT:PSS/TiO_x transport layers), with an average efficiency of 18.0% and a remarkably low device-to-device standard deviation of 0.7% (*versus* 1.05%). Mott–Schottky and impedance spectroscopy analysis also demonstrated an elevated built-in potential (0.94 V *vs.* 0.84 V) and suppressed recombination resistance, respectively, underlining the effectiveness of paired dipole layers in enhancing charge extraction, reducing hysteresis, and improving reproducibility in low-temperature-processed PSCs.

In their study, Yang *et al.* introduced a zwitterionic interfacial dipole – trimethylamine oxide (TMAO) between a mesoporous TiO_2 ETL and a perovskite absorber to suppress charge accumulation and recombination at this critical junction.[198] By forming a molecular "bridge," TMAO shifted the TiO_2 conduction-band minimum upward (from 4.23 eV to 4.15 eV), thereby lowering the interfacial energetic barrier for electron transfer, and its negatively charged oxygen sites bound to surface Ti^{4+} to reduce oxygen vacancy defects. The impact of
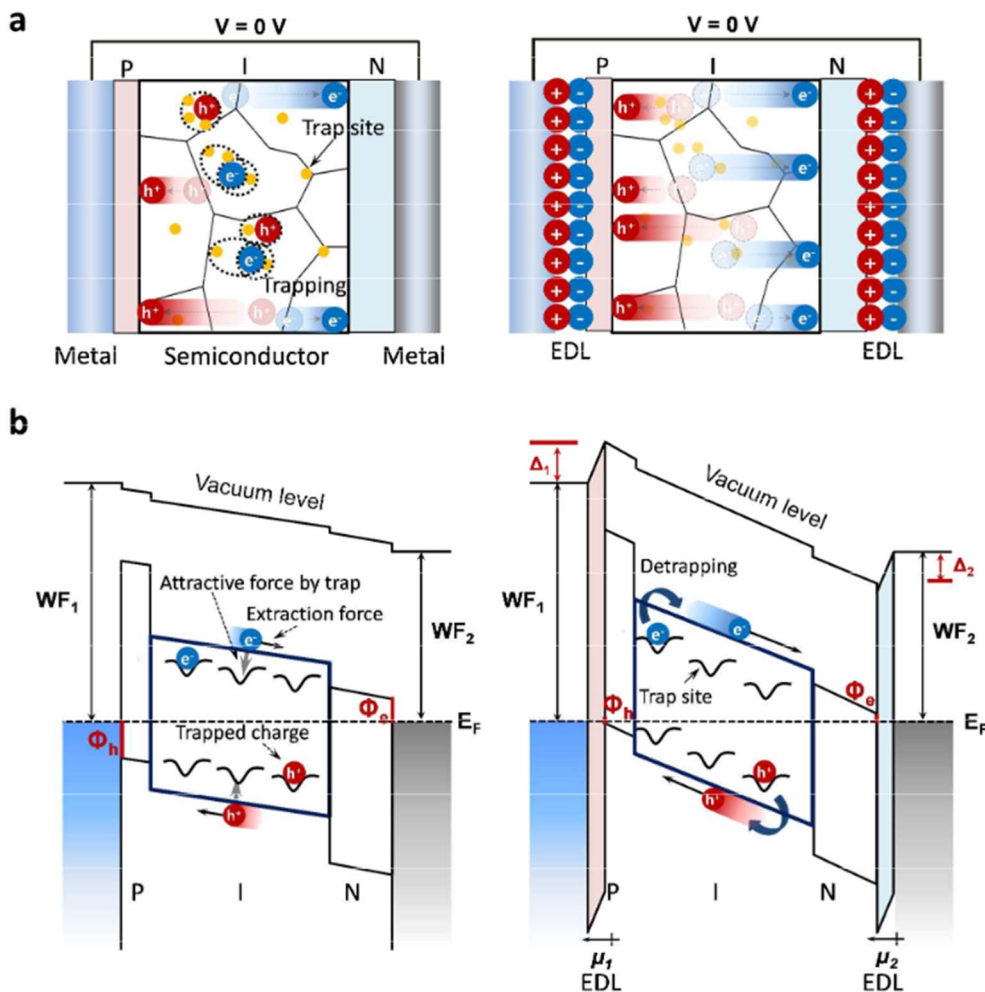
Fig. 33 Mitigation of interfacial charge trapping in PI(N) junctions *via* electric double layers (EDLs): (a) conceptual diagrams showing trap sites and charge dynamics in untreated and EDL-modified structures; (b) energy band diagrams illustrating how EDL-induced dipoles modulate vacuum levels and facilitate charge extraction by suppressing trapping effects. Reproduced with permission from ref. 197, Copyright 2018, Royal Society of Chemistry.

the TMAO interlayer in engineering the interface energetics is presented in Fig. 34. Simultaneously, the positively charged trimethylammonium moiety promoted uniform perovskite crystal growth within the mesoporous scaffold, eliminating interfacial voids and passivating surface trap states. These synergistic effects accelerated charge extraction (fast PL lifetime shortened from 10.94 to 6.51 ns), decreased trap-state densities (Mott–Schottky-derived doping density halved), and nearly eliminated hysteresis (hysteresis index reduced from 2.2% to 0.07%), resulting in a champion PCE of 21.77% with negligible hysteresis. Crucially, even without encapsulation, the devices maintained 80% of their original performance after 200 hours of exposure to testing conditions under continuous 100 mW cm^{-2} illumination and showed markedly improved thermal and humidity stability (only 36% PCE loss after 108 h at 85 °C/85% RH), underscoring the promise of interfacial-dipole engineering for durable, high-performance perovskite photovoltaics.

Previous studies on interfacial dipole engineering in PSCs predominantly employed solution-processable methods using polymeric or small-molecule interlayers deposited prior to or during perovskite formation. While these approaches showed improvement in device performance, they often introduced changes to film morphology, crystallization, and interface coverage, making it difficult to isolate the electronic effects of the dipole layer. In contrast, Lee *et al.* employed vacuum-deposited, sub-nanometer pyridine-containing small molecules as interfacial layers (EILs) between CH$_3$NH$_3$PbI$_3$ perovskite and a C$_{60}$ ETL to engineer interface energetics.[199] Among the tested molecules – 3TPYMB, B4PyMPM, and TmPyPB, the 0.5 nm 3TPYMB layer yielded the most notable performance gains, with champion PCEs reaching 18.8%, representing a 24.5% improvement over control devices without the EIL. *In situ* ultraviolet photoelectron spectroscopy (UPS) and X-ray photoelectron spectroscopy (XPS) provided critical insight into the origin of these enhancements. The UPS spectra revealed that the introduction of the 3TPYMB EIL led to a notable
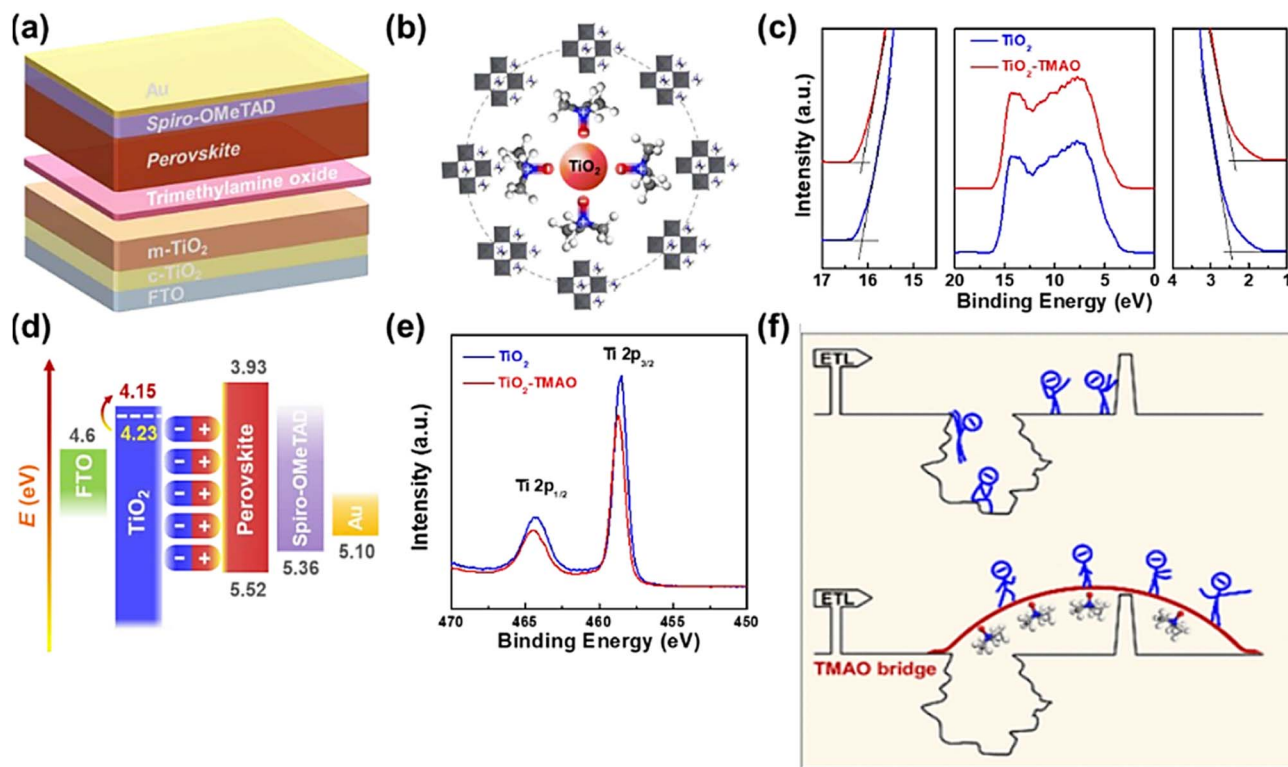
Fig. 34 TMAO-assisted surface passivation and energy alignment in TiO$_2$-based perovskite solar cells: (a) device structure; (b) schematic of TMAO interaction with the TiO$_2$ surface; (c) UPS spectra comparing TiO$_2$ and TiO$_2$–TMAO films; (d) energy level alignment across device layers; (e) Ti 2p core level XPS spectra showing negligible chemical shift with TMAO modification; (f) schematic illustration of TMAO molecules bridging interfacial defects to suppress charge recombination and enhance carrier transport. Reproduced with permission from ref. 198, Copyright 2019, American Chemical Society.
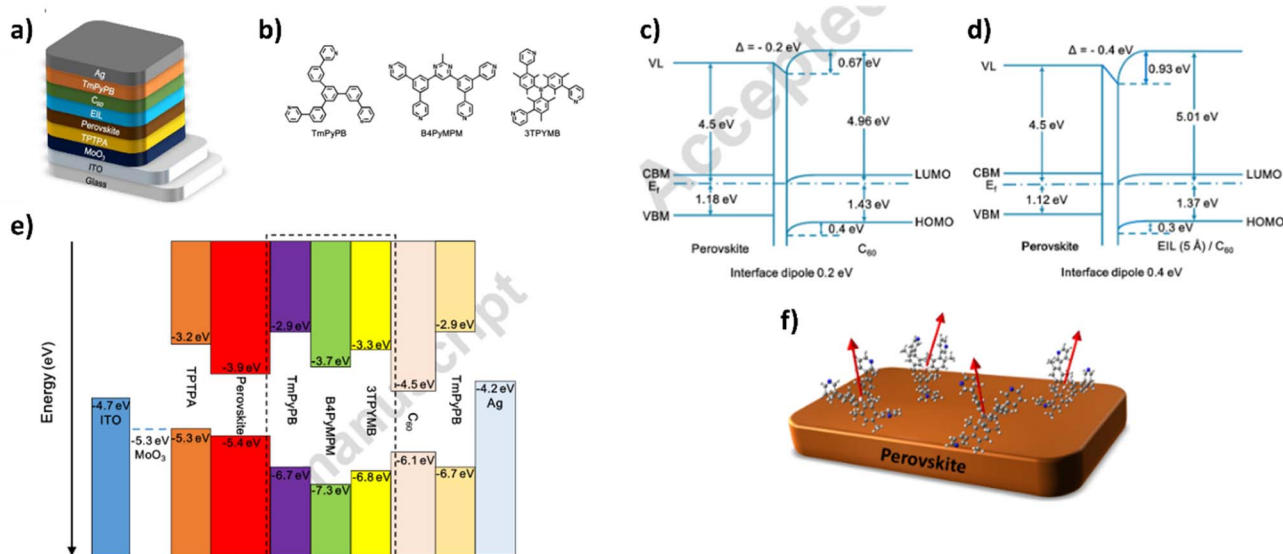

Fig. 35 Energy level tuning and interface dipole engineering in inverted PSCs: (a) device architecture incorporating a C$_{60}$-based ETL and doped TmPyPB as the hole-transport material; (b) molecular structures of TmPyPB, B4PyMPM, and 3TPYMB; (c) energy level diagram of individual layers showing HOMO/LUMO or VBM/CBM levels, with band alignments across interfaces; and a 5 Å-thick EIL modifying vacuum level alignment and reducing energy barriers; (e) illustration of oriented interfacial dipole moments at the perovskite interface that contribute to vacuum level shifts and improved charge extraction (f) schematic representation of molecular orientation contributing to interfacial dipole formation. Reproduced with permission from ref. 199, Copyright 2017, Elsevier Ltd.
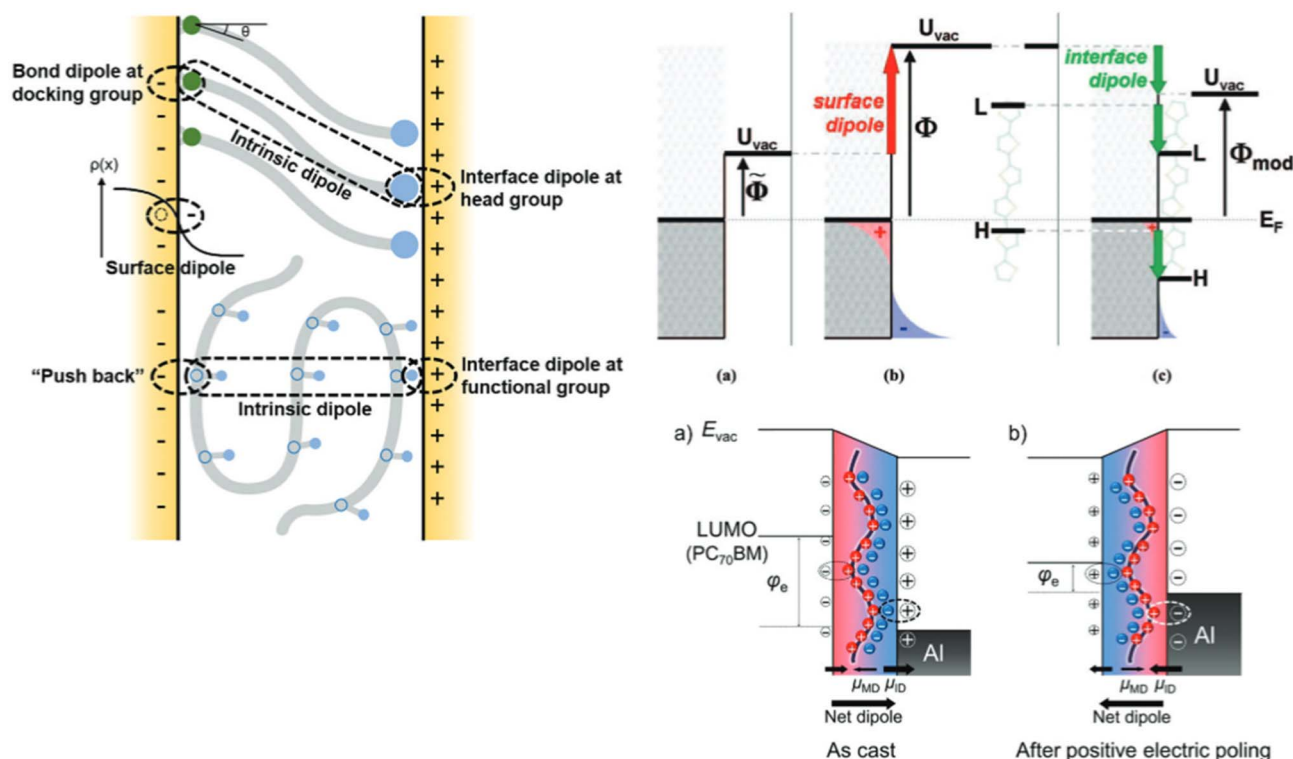
Fig. 36 Mechanisms of dipole formation and decoupled contributions from intrinsic molecular dipoles and interfacial dipole moments in self-assembled monolayers and polar polymers. (Upper left) A schematic of SAMs showing decoupled dipole contributions: bond dipoles at the docking group, interface dipoles at the head group, intrinsic backbone dipole, and terminal functional group dipoles. These interact with the electrode to induce vacuum level shifts *via* "push–back" and charge redistribution effects. (Bottom left) Polar polymer interlayers with intrinsic backbone dipoles and interface dipoles at both the electrode and active layer interfaces, influencing local electric fields and energy level alignment. Reproduced with permission from ref. 200–202, Copyright 2018, Royal Society of Chemistry; Copyright 2015, WILEY-VCH; Copyright 2008, American Chemical Society.

vacuum-level shift of approximately 0.4 eV at the perovskite/C_{60} interface, substantially greater than the 0.2 eV shift induced by C_{60} alone. This shift signifies the emergence of a pronounced interfacial dipole oriented to promote efficient electron transfer from the perovskite layer to the C_{60}, as illustrated in Fig. 35. Concurrently, XPS analysis showed no detectable chemical interaction or core-level shifts in the perovskite, confirming that the EILs do not alter its surface composition or structure, thus isolating the effect to purely electronic modulation.

This combination of strong dipole formation and chemical inertness suggested that the EILs improve interfacial band alignment without compromising perovskite integrity. The inferred electronic realignment was further supported by device-level measurements: transient photocurrent (TPC) showed faster charge extraction ($\tau_{ph}c$ reduced from 0.24 μs to 0.17 μs) and transient photovoltage (TPV) exhibited slower recombination ($\tau_{ph}\nu$ increased from 0.64 μs to 0.72 μs). In their comprehensive study, Lim *et al.* systematically investigated how dipolar interlayers including SAMs and conjugated polyelectrolytes (CPEs) can be strategically employed to modulate electrode work functions and tune energy-level alignments at critical interfaces in both organics and PSCs.[200] By combining controlled interlayer deposition with *in situ* UPS/XPS, the authors decoupled and quantified the effects of interfacial

dipoles from morphological or chemical influences. Some of the salient observations of the study are illustrated in Fig. 36.

Their results revealed that the vacuum-level shifts induced by these interlayers (typically 0.2–0.6 eV) are governed primarily by the bonding dipole formed at the substrate–molecule junction, rather than the net molecular dipole moment. In the case of CPEs, the nature of the counterion played a key role: for instance, replacing Br^- with a bulkier and less coordinating BIm_4^- led to a larger vacuum-level shift and enhanced band bending at the interface. Notably, XPS analysis confirmed the absence of core-level shifts or new chemical species, validating that these effects are purely electronic in nature. In addition to this, they observed that the energy-level alignment at the electrode/active-layer interface can transition from vacuum-level alignment to Fermi-level pinning depending on the strength and nature of the induced dipole. This transition was particularly evident in the case of CPE layers, where strong dipoles from bulky counterions (like BIm_4^-) led to pronounced downward vacuum-level shifts, effectively lowering the injection barrier for electrons. Second, the study found that the dipole-induced shifts scale with the areal dipole density and molecular orientation, which highlights the importance of molecular packing and substrate interaction in determining the interfacial electronic landscape. Third, they noted that these dipolar
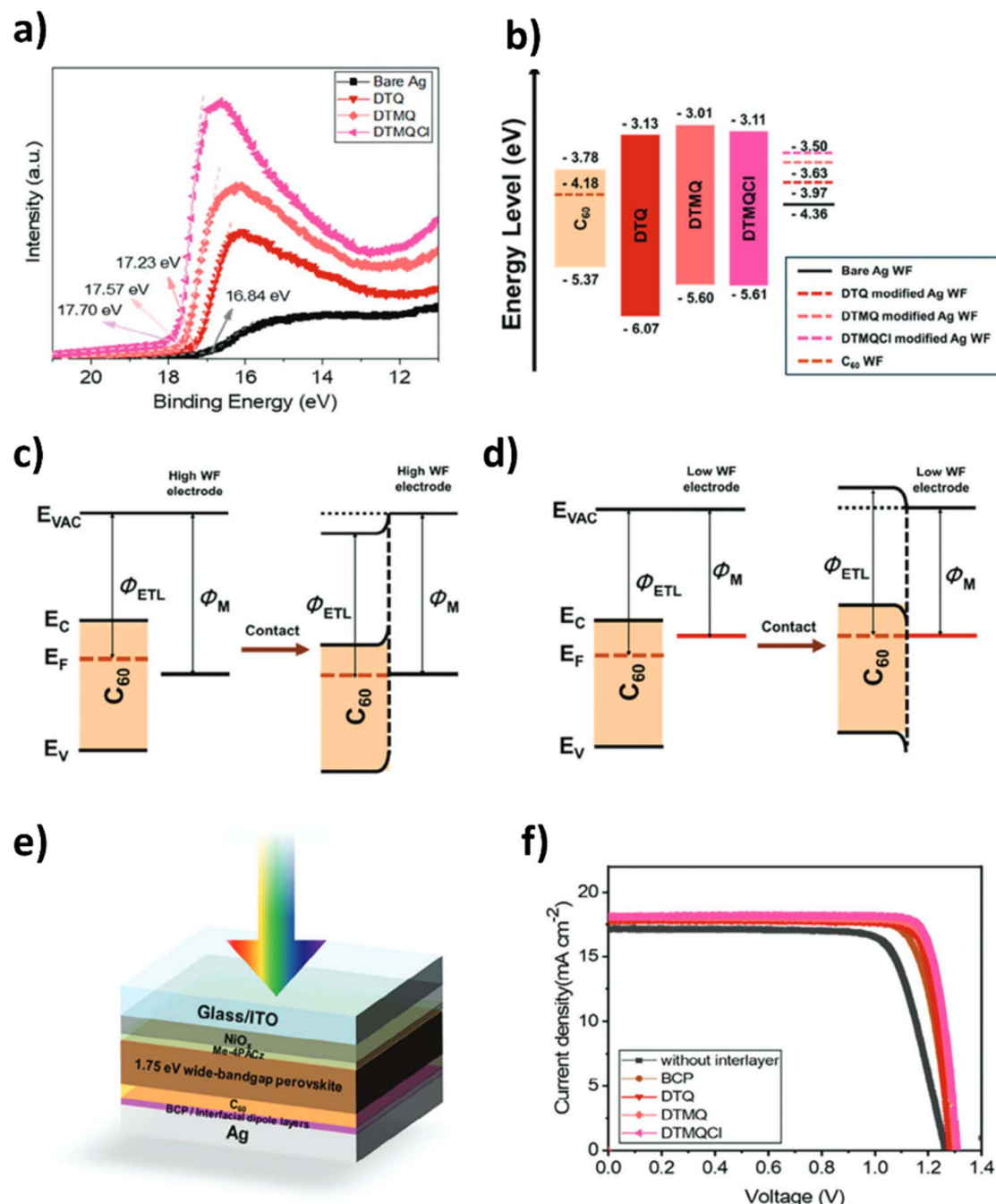
Fig. 37 (a) Ultraviolet photoelectron spectroscopy (UPS) spectra showing the secondary electron cut-off region used to extract work functions of bare Ag and Ag modified with dipolar interlayers DTQ, DTMQ, and DTMQCl. (b) Energy level diagrams of C_{60}, DTQ, DTMQ, and DTMQCl, illustrating how molecular dipole moments modulate interface energetics. (c and d) Schematic band bending diagrams for C_{60} in contact with Ag electrodes: (c) high work function Ag induces a Schottky barrier, while (d) low work function Ag (modified using interlayers) leads to ohmic contact. (e) Schematic architecture of a planar PSC used in this study. (f) J–V characteristics of PSCs with and without dipolar interlayers. Reproduced with permission from ref. 203, Copyright 2024, Wiley-VCH GmbH.

modifications are broadly applicable across different substrate types, including ZnO, ITO, and MoO_3, illustrating the generality of the approach. Finally, the work emphasized that because these dipolar layers are chemically orthogonal and do not react with the substrate or active layer, they are compatible with delicate semiconductors such as halide perovskites. Overall, the

study laid out a predictive and transferable framework for interface engineering *via* dipolar interlayers, enabling fine-tuned control over WF and energy-level alignment in a wide range of optoelectronic devices.

Heo *et al.* presented a strategic interface engineering approach to mitigate V_{OC} losses in WBG PSCs – a crucial
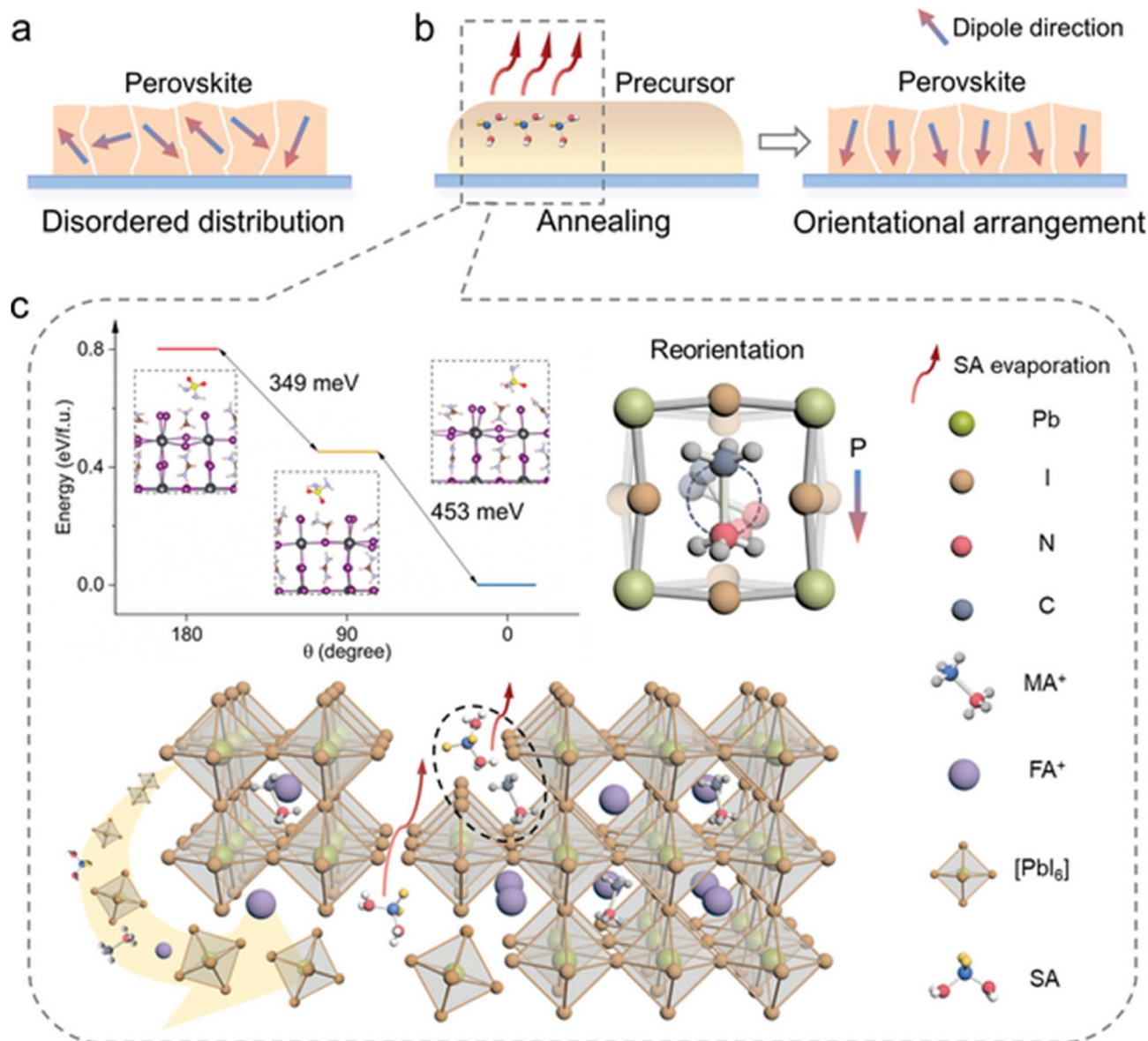
Fig. 38 Schematic illustration of vertical polarization alignment in perovskite films. (a) Random dipole orientation in the reference film with no net polarization. (b) SA-regulated film showing aligned dipoles and macroscopic vertical polarization. (c) Polarization rearrangement driven by molecular traction from the SA additive, with insets showing relative energies for different MA^+ orientations (0°, 90°, and 180°), favoring vertical alignment. Reproduced with permission from ref. 204, Copyright 2023 Wiley-VCH GmbH.

limitation that hinders their application in tandem photovoltaic architectures.[203] The researchers introduced n-type quinoxaline-phosphine oxide-based small molecules with strong dipole moments as effective cathode interfacial layers between the WBG perovskite absorber, $FA_{0.65}MA_{0.20}Cs_{0.15}$-$Pb(I_{0.8}Br_{0.2})_3$, and the ETL (PCBM). Detailed characterization using UPS revealed that the organic interfacial layers named DTQ, DTMQ, and DTMQC layers induce a downward shift in the vacuum energy level of the perovskite surface, effectively deepening the WF as is evident from Fig. 37. This shift resulted in a more favorable alignment between the CBM of the perovskite and the lowest unoccupied molecular orbital (LUMO) of PCBM, facilitating more efficient electron extraction and reducing energetic barriers at the interface. Complementary

measurements using Kelvin probe force microscopy (KPFM) further confirmed the formation of an interfacial electric dipole, as evidenced by a distinct increase in surface potential at the perovskite/PCBM interface following FABr treatment. The combined UPS and KPFM results thus demonstrated that the FABr layer not only adjusts the interfacial energy landscape but also introduces an internal electric field that enhances carrier separation and transport.

These modifications were correlated with substantial optoelectronic improvements: photoluminescence (PL) and electroluminescence (EL) measurements indicated reduced nonradiative recombination, contributing to a remarkable V_{OC} of 1.29 V among the highest reported for ≈1.74 eV bandgap perovskites and a PCE of 17.6%. Thus, this work established
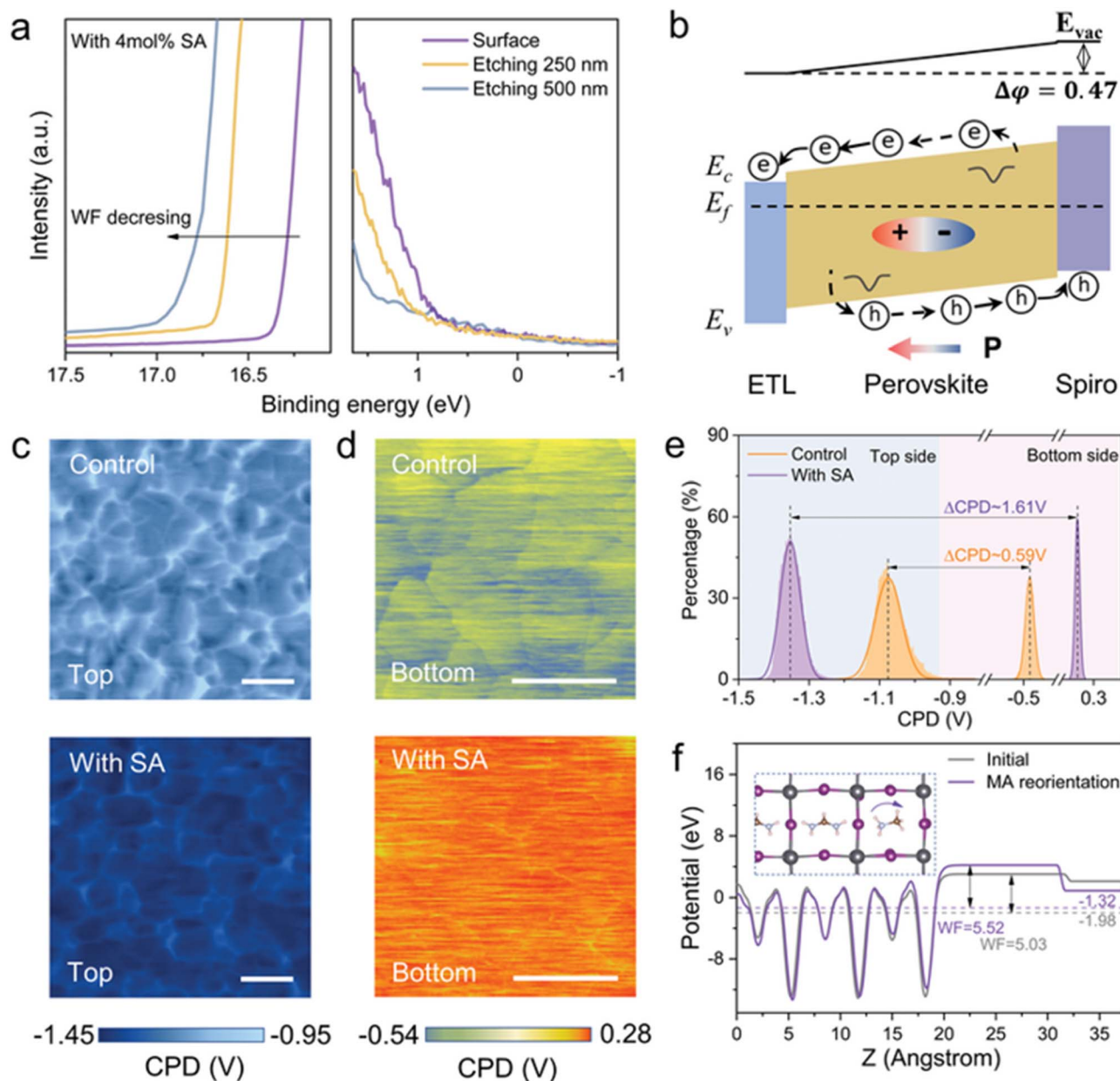
Fig. 39 Electronic properties and charge transport. (a) UPS spectra of SA-regulated perovskite films recorded at different Ar$^+$ ion etching depths. (b) Energy-level diagram and carrier transport model. (c and d) KPFM CPD maps of top and bottom film surfaces. (e) Histogram of CPD values. (f) Calculated electrostatic potential and WF with/without MA$^+$ reorientation. Reproduced with permission from ref. 204, Copyright 2023 Wiley-VCH GmbH.

interfacial dipole engineering as an effective, solution-processable strategy for boosting the efficiency of WBG PSCs and offered a promising pathway for their application in high-performance perovskite–silicon tandem devices. In their 2023 study, Wu *et al.* presented a pioneering strategy for internally coordinating the energy levels of PSCs through molecular dipole alignment.[204] The authors introduced a polar small molecule, 4-trifluoromethylphenethylammonium iodide (CF$_3$-PEAI) as an SA (self-alignment) additive, into the perovskite precursor solution to induce spontaneous reorientation of methyl-ammonium (MA$^+$) cations during film formation. This

molecularly driven alignment resulted in a vertically oriented intrinsic dipole moment across the absorber layer as illustrated in Fig. 38.

A key strength of the study lies in the direct spectroscopic and surface-potential characterization of this internal dipole. UPS combined with sequential Ar$^+$ etching revealed a gradual upward shift in the vacuum energy level from the bottom to the top of the perovskite film in SA-treated samples as shown in Fig. 39. This gradient reflected a built-in electric field established by the vertically aligned dipoles, which created a favorable energy-level cascade for carrier transport. Specifically, the
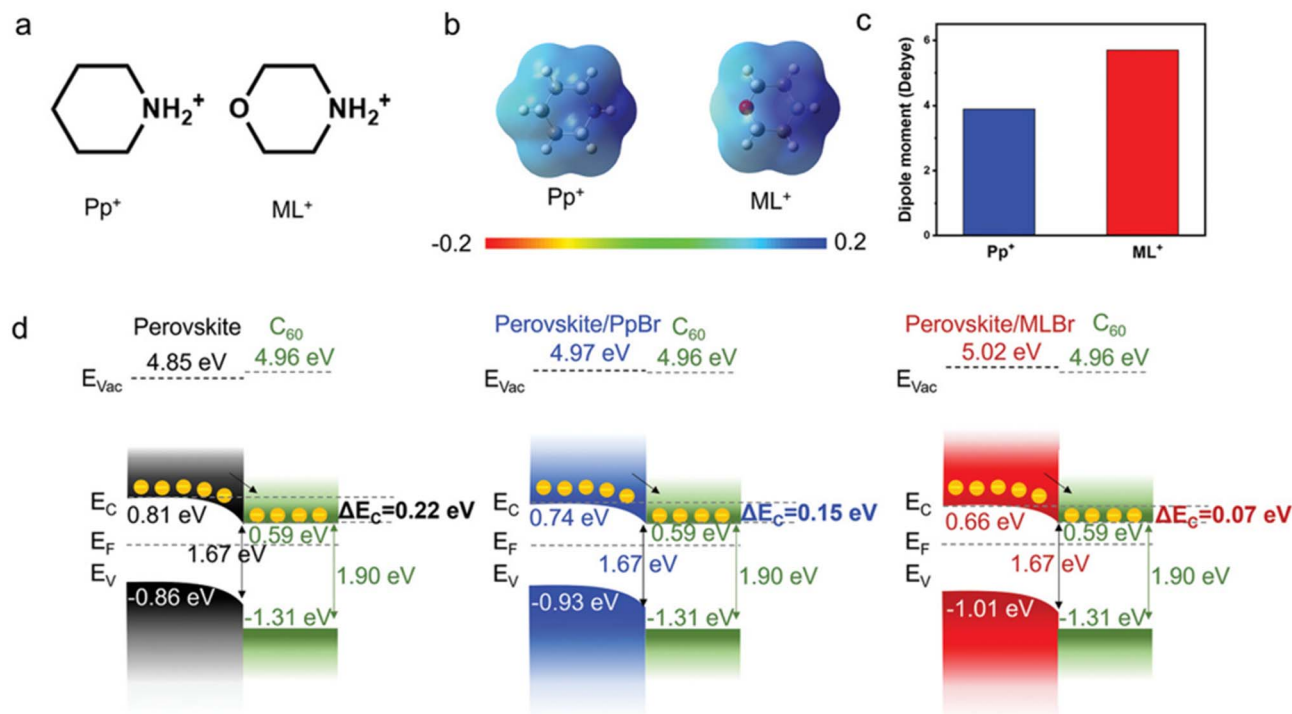
Fig. 40 Dipole engineering at the perovskite/C$_{60}$ interface. (a) Molecular structures of Pp$^+$ and ML$^+$. (b) Electrostatic potential (ESP) distributions. (c) Calculated dipole moments. (d) Energy level alignment for perovskite/C$_{60}$, perovskite/PpBr/C$_{60}$, and perovskite/MLBr/C$_{60}$ configurations. Reproduced with permission from ref. 205, Copyright 2024 Wiley–VCH GmbH.

VBM became progressively deeper toward the surface, with a total shift of ~0.15 eV compared to untreated films.

Complementary evidence was provided by KPFM, where the SA-treated films exhibited a notable increase in surface potential relative to control samples. This surface potential shift (~50–80 mV) confirmed the presence of an interfacial dipole layer that enhanced the built-in field and improves charge extraction at the electrode interfaces. Together, these UPS and KPFM measurements provided compelling proof that molecular dipole alignment can spatially modulate the electronic structure of perovskite films at the nanoscale. Polarization-sensitive infrared spectroscopy and piezoresponse force microscopy (PFM) further validated the uniform molecular alignment, while temperature-dependent photoluminescence (PL) and time-resolved PL measurements revealed notable suppression of non-radiative recombination and reduced exciton binding energy due to enhanced dielectric screening. As a result of these synergistic effects, the dipole-coordinated perovskite devices achieved a high V_{OC} ~1.20 V, extended carrier diffusion lengths (~1.7 μm), and an impressive PCE of 24.63%, along with excellent operational stability over 1000 hours. This study underscores the importance of molecular-scale dipole engineering as a scalable, non-invasive, and intrinsically stable route to tune energy levels and elevate both performance and durability in next-generation perovskite photovoltaics. In a notable advancement for interface engineering in perovskite photovoltaics, Wang *et al.* introduced a dipole-tuning strategy at the electron–transport interface to reduce voltage loss and improve device performance in both single-junction and monolithic tandem PSCs.[205] By designing and incorporating dipolar organic interlayers specifically, piperidinium bromide (PpBr) and morpholinium bromide (MLBr) between the perovskite absorber and the fullerene (C$_{60}$) ETL, the study demonstrated how targeted molecular engineering could modulate interfacial energy-level alignment, minimize recombination losses, and contribute to improved photovoltaic performance and long-term device stability. This approach leveraged the intrinsic dipole moments of small organic cations (3.7 D for PpBr and 5.9 D for MLBr) to generate internal electric fields that shift the vacuum energy level and conduction band offset at the ETL interface as is illustrated in Fig. 40.

Detailed insights into the energetic modulation induced by the dipole layers were obtained using UPS. For pristine perovskite films, the VBM and vacuum level (E_{vac}) served as benchmarks. Upon deposition of PpBr, a modest upward shift of ~0.12 eV in E_{vac} and ~0.10 eV in VBM was observed. MLBr, with a higher dipole moment, induced larger shifts (~0.20 eV and ~0.15 eV, respectively). These systematic shifts in the vacuum level are a direct consequence of the surface dipole introduced by the interlayers, as the net dipole moment perpendicular to the interface modifies the surface potential *via* the Helmholtz equation:

$$\Delta V = \frac{\mu N}{\varepsilon_0 \varepsilon_r} \quad (9)$$

where μ is the molecular dipole moment, N is the surface density of dipoles, and ε_r is the local relative permittivity. This energetic modulation reduced the energy offset between the
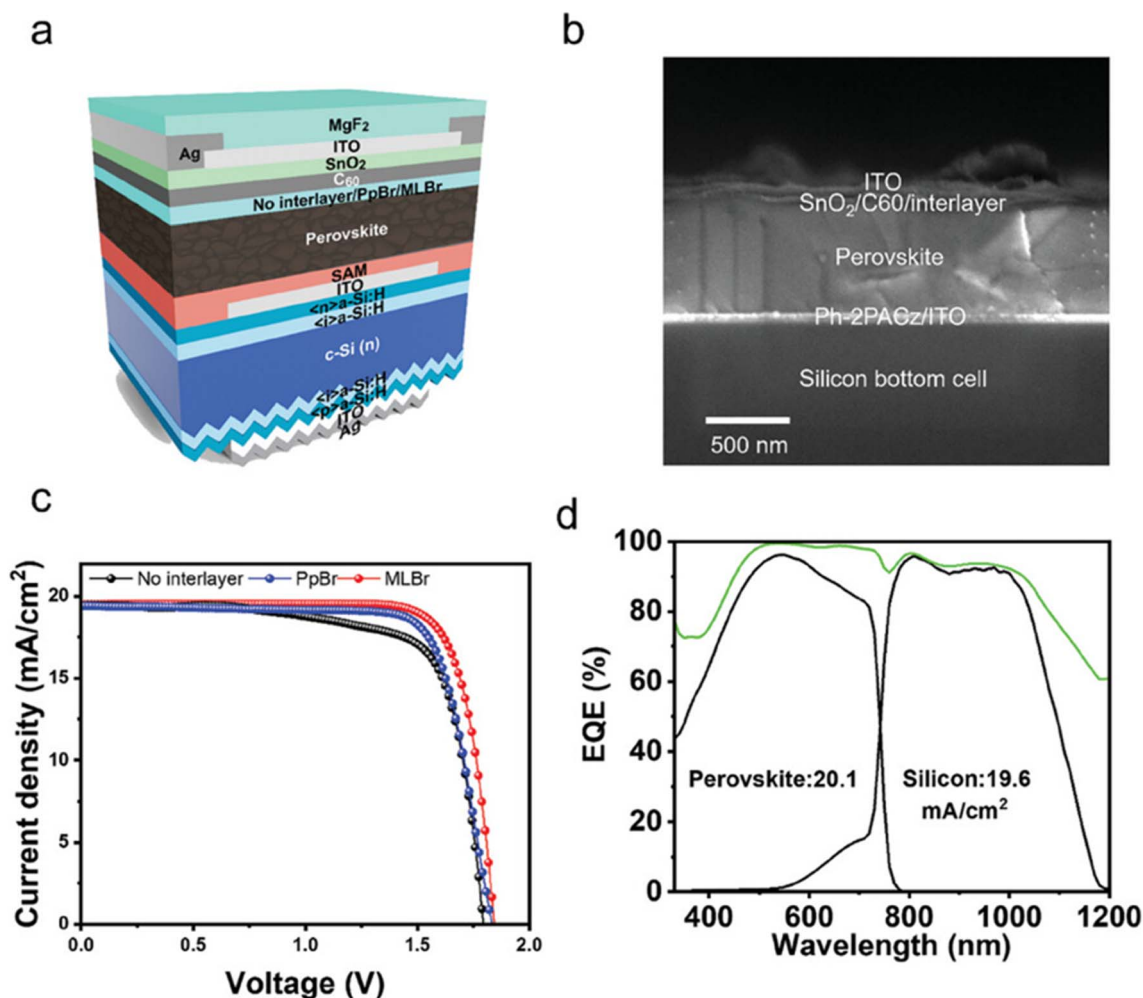
Fig. 41 Device performance of perovskite–silicon tandems incorporating a dipole interlayer. (a) Schematic of the tandem cell architecture. (b) Cross-sectional SEM image of a representative MLBr-based tandem. (c) J–V characteristics of top-performing devices with and without the dipole interlayer. (d) EQE and reflectance spectra of the champion tandem featuring an MLBr interlayer. Reproduced with permission from ref. 205, Copyright 2024 Wiley-VCH GmbH.

perovskite CB and the LUMO level of C_{60}, facilitating more efficient electron extraction and minimizing interfacial energetic barriers.

Complementary X-ray photoelectron spectroscopy (XPS) and QFLS analyses further supported the dual functionality of the dipolar interlayers: not only did they tune energy levels, but they also chemically passivated surface traps *via* ionic interactions between the interlayer's functional groups (*e.g.*, Br^-) and undercoordinated Pb^{2+} at the perovskite interface. This resulted in reduced trap-assisted recombination, as evidenced by enhanced steady-state PL and prolonged carrier lifetimes. The devices incorporating MLBr, in particular, exhibited the highest QFLS values, indicating minimal voltage loss. The most notable outcome of this interfacial dipole engineering was its successful translation into two-terminal perovskite/silicon TSCs, marking the first report of such an interlayer being deployed at the electron–transport interface in a monolithic tandem architecture. The tandem devices with MLBr interlayers achieved a certified PCE of 28.8% (Fig. 41) among the highest reported for

this configuration while also demonstrating remarkable thermal-cycling stability, retaining 97% of their initial efficiency after 400 IEC-standard thermal cycles. This performance not only reflects improved charge transport and reduced non-radiative losses but also underscores the long-term stability conferred by molecular-level interface passivation and energy level alignment.

In conclusion, the work by Wang *et al.*[205] established dipole-oriented interlayer engineering as a powerful and versatile strategy for enhancing both the performance and stability of PSCs and, critically, extends its applicability to the more demanding architecture of monolithic tandem devices. By uniting principles of molecular dipole physics, interfacial energetics, and device-scale implementation, this study opens new avenues for rational interface design in high-efficiency, durable perovskite photovoltaics.

5.3.1 Critical analysis of dipole-tailored interlayers in perovskite solar cells. A critical evaluation of dipole-tailored interlayers highlights how molecular dipole orientation,

Table 4 Critical comparison of varied dipole tailored interlayers for perovskite interface modification

Parameter	Fluorinated aromatics	Methoxy/amino substituted aromatics	Halogenated aromatics	Zwitterionic interlayers	Planar π-conjugated dipoles
Head/anchor group	Phosphonic acid and carboxylate	Phosphonic acid and amines	Phosphonic acid and carboxylate	Ionic head groups; tethered alkyl/aryl tails	Phosphonic acid, fullerene, and pyridine
Dipole effect & energy alignment	Strong downward/upward dipole tuning; significant WF shift	Moderate upward dipole; favourable hole extraction and V_{OC}	Strong dipole shifts; halogen polarizability improves energy alignment	Large, tunable dipole depending on cation–anion separation	Moderate but stable dipole; strong π–π alignment with perovskite bands
Trap passivation strength	Moderate to strong; enhanced by electrostatic Pb^{2+} interactions	Strong; electron-donating groups enhance Pb–π orbital interactions	Strong; halogen–metal interactions mimic halide passivation	Strong ionic passivation of defects and grain boundaries	Very strong; extended π-systems enhance orbital overlap
Packing density & surface coverage	Dense packing; fluorination promotes hydrophobic surfaces	High packing density; polar groups improve wettability	Moderate; bulky cores require optimization	Variable; depends on chain length	High; ordered monolayers with π–π stacking
Processing compatibility	Solution-processable; compatible with vacuum deposition	Excellent solution compatibility	Generally, solution-compatible; some steric packing issues	Compatible with solution and vapor deposition	Good process compatibility; guides perovskite growth
Stability under stress	High photostability and moisture resistance; dipole relaxation possible	Good thermal and light stability; moderate humidity resistance	High chemical and thermal stability; bromination reduces photooxidation	Moderate; ionic migration under bias may occur	Excellent thermal and photostability; rigid cores resist reorientation
Performance trade-offs	Strong dipole tuning and moisture stability; risk of overcompensation causing energetic disorder	Balanced band alignment and passivation; reduced long-term hydrophobicity	Strong dipole + passivation synergy; limited by steric hindrance	Strong dipole tuning and defect healing; risk of ion migration and hysteresis	Stable band alignment, excellent passivation, and ordered growth; weaker dipole tuning compared to fluorinated analogues

magnitude, and structural rigidity govern their role in tuning interface energetics, suppressing non-radiative recombination, and enhancing long-term device stability.

5.3.1.1 Energy-level alignment and dipole effects. Dipole-tailored interlayers are specifically designed to introduce a permanent dipole moment at the perovskite/charge transport interface, enabling controlled vacuum-level shifts that reduce interfacial energy offsets. The dipole orientation is decisive: interlayers with upward-oriented dipoles at the perovskite/HTL interface raise the work function and improve valence band alignment, thereby enhancing hole extraction and increasing V_{OC}. Conversely, downward-oriented dipoles at the ETL/perovskite interface lower the work function, minimizing barriers for electron transfer. The dipole magnitude, however, must be carefully optimized. Excessively strong dipoles can cause interfacial band bending or induce mid-gap states that counteract passivation benefits, whereas moderate, uniformly oriented dipoles facilitate balanced charge transfer. Molecular design strategies such as electron-donating ($-OCH_3$ and $-NH_2$) or electron-withdrawing ($-CF_3$ and $-CN$, halogens) substituents modulate the dipole strength *via* inductive and resonance effects. Rigid π-conjugated backbones stabilize the dipole orientation and prevent reorientation under thermal or illumination stress, while flexible aliphatic linkers often yield reduced packing density and less predictable vacuum-level shifts.

5.3.1.2 Interfacial trap passivation. Beyond dipole modulation, dipole-tailored interlayers also contribute to defect passivation through functional anchoring groups and $\pi-\pi$ interactions. Common anchoring chemistries include phosphonic acids, carboxylates, and fullerene derivatives, which bind to undercoordinated Pb^{2+} or halide vacancies at the perovskite surface, thereby reducing trap-assisted recombination. Conjugated dipole molecules provide additional orbital overlap with Pb 6p and halide np states, stabilizing shallow defects and delocalizing charge carriers. Fluorinated dipole interlayers, in particular, enhance electrostatic passivation by interacting with positively charged Pb^{2+} centers, while simultaneously increasing hydrophobicity and resisting ionic migration. Similarly, halogenated dipole backbones (*e.g.*, brominated aromatics) exploit halogen–metal interactions to mimic halide compensation, strengthening passivation while tuning dipole orientation. However, bulky dipole substituents may compromise molecular ordering, leading to non-uniform trap passivation across the surface. Thus, the effectiveness of these interlayers hinges on the synergistic contribution of chemical anchoring, electrostatic tuning, and conjugated orbital interactions.

5.3.1.3 Surface coverage, morphology, and wettability. The degree of molecular packing and interlayer coverage strongly influences dipole uniformity and perovskite film growth. Compact, highly ordered dipole layers minimize pinholes and energetic inhomogeneities, ensuring consistent charge extraction across the interface. Polar substituents (*e.g.*, $-OCH_3$ and $-CF_3$) improve surface wettability and facilitate uniform perovskite nucleation, whereas hydrophobic tails enhance moisture resistance but may hinder initial film adhesion. Rigid dipole interlayers with planar π-systems promote lateral molecular ordering,

guiding uniform crystallization of the perovskite overlayer and reducing grain boundary defects. In contrast, flexible dipole linkers or sterically bulky substituents disrupt packing density and introduce local energetic disorder. Therefore, balancing dipole strength with molecular ordering is critical to achieving reproducible surface coverage and defect-free morphology.

5.3.1.4 Operational stability. The stability of dipole interlayers under illumination, heat, and moisture stress varies with molecular rigidity, substituent chemistry, and anchoring strength. Rigid aromatic dipole backbones exhibit superior thermal and photostability, as their extended π-conjugation minimizes structural reorientation. Fluorinated or halogenated interlayers resist photooxidation and inhibit bond cleavage pathways, preserving dipole orientation under prolonged stress. Anchoring groups with multidentate coordination (*e.g.*, tridentate phosphonic acids) ensures strong, irreversible binding to oxide or perovskite surfaces, while weaker linkers (*e.g.*, amines or carboxylates) are more prone to desorption, especially in humid environments. Nevertheless, dipole-tailored interlayers remain vulnerable to dipole relaxation over time, where the interfacial dipole gradually diminishes due to molecular reorientation, reducing long-term energy-level alignment benefits. Strategies such as rigidifying the backbone, introducing electron-withdrawing substituents, and combining dipole effects with chemical passivation have been shown to prolong interfacial dipole retention and device operational lifetime.

5.3.1.5 Performance trade-offs. As with SAM molecules, the performance of dipole-tailored interlayers reflects a compromise between energy-level tuning, passivation, morphology control, and stability. Molecules with strong electron-withdrawing substituents (*e.g.*, fluorinated aromatics) provide significant vacuum-level shifts and moisture stability, but risk dipole overcompensation and increased energetic disorder. Conversely, dipole interlayers with moderate electron-donating groups (*e.g.*, methoxy- or amino-substituted aromatics) achieve balanced band alignment and trap passivation but may exhibit reduced moisture resistance. Planar conjugated dipole interlayers deliver excellent film ordering and operational stability, whereas bulky or flexible dipole moieties often compromise packing uniformity. Collectively, these comparisons highlight that the rational design of dipole-tailored interlayers requires a holistic approach optimizing dipole strength and orientation while ensuring chemical passivation, ordered packing, and environmental robustness. Ultimately, dipole-tailored interlayers present an elegant yet complex strategy to fine-tune interfacial energetics, but their practical deployment in scalable devices demands careful balancing of efficiency, stability, and processing compatibility (Table 4).

6. Challenges and future direction

The emergence of SAMs and dipole-tailored interfacial modifiers as tools for fine-tuning device interfaces represents a paradigm shift in the design of next-generation photovoltaic technologies. These molecular interface strategies offer exceptional control over interfacial energetics, surface wettability,

chemical passivation, and ion-selective transport pathways. However, despite their conceptual elegance and functional versatility, the practical translation of these methods into commercial platforms faces two formidable bottlenecks: (i) lack of scalable and compatible deposition techniques and (ii) insufficient long-term stability under dynamic electrochemical operating conditions. A comprehensive understanding of the physicochemical underpinnings of these challenges is essential for rational strategy development.

6.1. Scalability constraints

The molecular precision and bottom-up assembly characteristics that make SAMs attractive at the lab scale also pose inherent limitations when translating to large-area devices.

● Deposition uniformity: achieving pinhole-free, conformal, and homogeneous SAM coverage over large substrates (>100 cm^2) is inherently challenging due to solution-based deposition techniques (*e.g.*, dip-coating, spin-coating, and vapor-phase methods) that are highly sensitive to surface cleanliness, roughness, and environmental conditions (humidity and temperature). In roll-to-roll or slot-die processing scenarios, maintaining nanometer-thick control and long-range molecular ordering of SAMs becomes increasingly difficult, which can lead to interfacial heterogeneities, shunt pathways, or incomplete dipole formation.

● Interfacial compatibility in tandems: in tandem architectures (*e.g.*, perovskite–silicon and perovskite–perovskite), the bottom subcell's top electrode must simultaneously serve as the growth substrate for the top subcell, demanding that SAMs fulfill multiple, sometimes conflicting roles like conductivity, transparency, wettability, and thermal resilience. Many SAMs designed for single-junction PSCs are not optimized for such multifunctionality, limiting their utility in stacked configurations.

● Throughput and process integration: industrially viable integration requires SAMs and dipole interlayers to be compatible with high-throughput manufacturing. However, their deposition often involves prolonged immersion or solvent exchange steps that are not directly transferrable to vapor-phase or in-line coating methods. The synthesis of dipolar molecules with precise functional groups (*e.g.*, phosphonic acids, thiols, and carboxylic acids) also adds complexity and cost to scale-up.

6.2. Thermal and chemical stability

Interface engineering strategies must ensure long-term operational stability under realistic conditions such as thermal load, light soaking, and ambient exposure. SAMs and dipolar layers, being organic and often mono- or few-molecular layers thick, are inherently vulnerable to chemical and thermal degradation.

● Thermal decomposition and desorption: SAMs anchored *via* thiol, silane, or phosphonic acid head groups may desorb or undergo bond cleavage at elevated temperatures (>85 °C), particularly in a vacuum or under prolonged illumination. This compromises interfacial dipole alignment and surface passivation. For tandem devices, where the thermal budget during top

cell processing can exceed 100–120 °C, conventional SAMs may not survive.

● Moisture and oxygen sensitivity: the hydrophilicity of certain SAMs (*e.g.*, carboxylic acid terminated) can lead to water ingress and localized degradation of the underlying perovskite or transport layer. Similarly, oxidation of dipolar molecules may alter their electronic dipole, thereby shifting interfacial energy levels over time. While fluorinated or alkylated tail groups improve moisture resistance, they often reduce charge transport or alter wettability unfavorably for subsequent layer deposition.

● Interface reconstruction: over operational timescales, particularly under bias and illumination, dynamic interfacial phenomena such as ion migration (*e.g.*, MA$^+$ and I$^-$) and chemical interactions with dipolar species can lead to interfacial reconstruction, reorientation of dipoles, or trap formation. This is particularly relevant in inverted (p–i–n) architectures where SAMs are often employed at the hole transport interface.

6.3. Electronic and dipolar stability

● Dipole drift and degradation: dipole layers whether formed *via* molecular assemblies or ionic additives are assumed to produce static band bending. However, under operational stress (illumination and electric field), dipolar alignment can degrade or reorient, leading to fluctuations in built-in potential and V_{OC}. Quantitative evidence of dipole stability across extended timescales is still sparse.

● Energy level pinning and interface states: SAM-induced dipoles modify work functions primarily through Helmholtz layer formation. However, imperfect or incomplete SAMs can introduce interface states that lead to Fermi level pinning, counteracting the desired energetic alignment and enhancing non-radiative recombination. Such effects become even more pronounced in multi-junction devices where cumulative interface quality is critical.

6.4. Future directions

To address these limitations and unlock the full potential of SAM and dipole interface engineering, several strategic directions are recommended (Table 5):

● Design of multifunctional and crosslinkable SAMs: development of SAMs with dual or even triple functionalities (*e.g.*, dipole alignment, passivation, and hydrophobic protection) and enhanced thermal robustness (*e.g.*, aromatic phosphonic acids and siloxane crosslinkers) can improve long-term interface stability. Chemically crosslinkable SAMs may allow covalent binding to both the substrate and overlaying layers, enhancing mechanical and thermal endurance.

● Vapor-phase and scalable deposition approaches: implementing molecular layer deposition (MLD), initiated chemical vapor deposition (iCVD), or atomic layer compatible SAM deposition techniques can offer better control over thickness, coverage, and scalability. These methods can help bridge the gap between laboratory-scale deposition and industrial roll-to-roll processing.

● *In situ* characterization and degradation tracking: development of *operando* spectroscopic and microscopic tools (*e.g.*,

Table 5 Scientific drivers and interface engineering challenges in designing next-generation TSCs

Aspect	Key challenges	Scientific rationale	Future directions
Substrate compatibility	Anchoring group–substrate specificity; poor adhesion on heterogeneous surfaces	Chemisorption depends on surface functional groups; non-uniformity disrupts SAM formation	Develop universal anchoring groups (e.g., boronic acids and zwitterions); improve pre-treatment methods
Surface topology	Defect formation on rough/porous electrodes	Multiscale roughness and capillarity hinder uniform monolayer formation	Engineer hierarchical SAMs or hybrid layers compatible with high-surface-area electrodes
Deposition scalability	Low-throughput techniques (immersion and LB transfer); poor reproducibility	Slow assembly kinetics; solvent effects; multilayer formation	Use scalable methods like spray/slot-die coating; develop rapid, field-assisted or electrochemically induced assembly
Molecular orientation & dipole alignment	Random dipole orientation leads to reduced or cancelled net effects	Requires tilt control and dipole density regulation for effective energy level tuning	Design self-orienting molecules; utilize supramolecular or liquid crystal ordering; apply templating surfaces
Chemical stability	Degradation under combined environmental and operational stress, solvents, and radicals	Head group or backbone cleavage; nucleophilic/electrochemical attack	Use redox-inert anchors (phosphonates), π-conjugated backbones, and cross-linkable tail groups
Mechanical robustness	Delamination and cracking on volume-changing electrodes	Thin, brittle SAMs cannot accommodate strain during cycling	Develop flexible, adaptive interfacial layers; embed SAMs within polymer or inorganic overcoats
Functionality retention	Loss of the dipole effect due to reorientation or breakdown	Dynamic cycling alters alignment or introduces defects	Stabilize dipole orientation via interlocking moieties or interfacial confinement
Characterization limitations	Lack of real-time insight into SAM behaviour during cycling	Conventional methods miss orientation, degradation, or ionic permeability	Employ in situ/operando tools (e.g., EC-XPS, VSFG, and EC-AFM) for monitoring
Computational prediction	Trial-and-error in molecule selection	Complex surface–molecule interactions not easily generalizable	Use DFT, MD, and ML models to predict anchoring, dipole effects, and stability under redox conditions
Integration into devices	Incompatibility with commercial processes or multi-layer architectures	SAM fragility and poor adhesion to active materials or SEI layers	Create hybrid molecular–inorganic or polymeric interfacial constructs; study lifecycle effects

Kelvin probe force microscopy and ambient photoemission spectroscopy) can help monitor dipole alignment, SAM integrity, and interfacial energetics in real time under bias and light exposure.

• Interface engineering in all-vacuum processed tandems: for vacuum-based tandem fabrication, integrating thermally stable dipolar molecules or polymeric interlayers compatible with vacuum sublimation steps (e.g., fluorinated carbazole derivatives) is critical. This requires co-optimization of interface chemistry and the deposition process.

• Hybrid interface strategies: synergistic combinations of SAMs with inorganic dipolar oxides (e.g., MoO_x and NiO_x) or 2D materials (e.g., graphene oxide and h-BN) may offer a pathway to combine molecular-level control with mechanical and thermal robustness. Such hybrid interfaces can be particularly useful in multi-junction architectures where interfacial engineering requirements vary across subcells.

• Standardization and lifespan modelling: finally, systematic aging studies and standardized degradation protocols (e.g., ISOS protocols) must be applied to evaluate SAM and dipolar interface performance in realistic operating environments. Incorporating such degradation data into predictive lifetime models will be essential for reliable commercial deployment.

7. Conclusions

The evolution of PSCs from laboratory curiosities to contenders in the global energy portfolio has been driven not only by advances in bulk materials but also by a growing recognition of the critical role played by interfaces. In this light, self-assembled monolayers (SAMs) and dipole-tailored interlayers have emerged as powerful molecular tools, offering a level of interfacial precision that conventional deposition strategies cannot match. Their ability to tune energy levels, passivate surface traps, and modulate wettability at the nanoscale represents a conceptual shift in device design one that places the interface at the heart of photovoltaic optimization. Yet, this promise is accompanied by a sobering set of practical challenges. SAMs, by virtue of their monolayer nature and reliance on specific anchoring chemistries, are exquisitely sensitive to substrate conditions, thermal budgets, and ambient degradation pathways. Their precise molecular ordering, which confers many of their electronic advantages, also renders them fragile as they are susceptible to desorption, reorientation, or chemical breakdown under real-world operating conditions. Dipole-tailored interlayers, while somewhat more adaptable in form (e.g., ionic additives and molecular layers), are equally vulnerable to temporal instabilities, with dipole drift, environmental

reactivity, and interface reconstruction acting as persistent bottlenecks.

This duality between molecular elegance and engineering fragility defines the present state of SAM and dipole-based interface engineering. Their integration into tandem perovskite architectures, in particular, magnifies these challenges. Tandem devices impose stricter demands: higher processing temperatures, cumulative mechanical stress, and complex interlayer compatibility between the subcells. Here, the interface must not only align energy bands but also remain electrically benign, thermally stable, chemically inert, and physically uniform across large areas all the while preserving manufacturability. However, it is in these very constraints that the next phase of innovation may arise. The path forward likely lies not in abandoning molecular interface strategies, but in reimagining them – moving from static, passive interlayers to dynamic, multifunctional systems. For SAMs, this might involve the development of covalently grafted or metal-chelating architectures that resist desorption and offer thermal resilience, even during top-cell processing. For dipolar interlayers, the future may lie in stimuli-responsive molecules, capable of self-correcting alignment under operational fields, or in molecular systems that can adaptively tune their dipole moments in response to device stressors. Moreover, the integration of data-driven design principles leveraging machine learning, high-throughput computational screening, and *in situ* spectroscopic diagnostics offers a new lens through which these materials can be engineered. Instead of laboriously trialing molecules one at a time, future research could map vast chemical spaces for interface modifiers that are not only electronically ideal, but also synthetically accessible, environmentally robust, and industrially scalable. Another promising avenue is the convergence of molecular and inorganic interface strategies. Hybrid interlayers that combine the specificity of SAMs with the robustness of 2D materials or the conformality of atomic layer deposition (ALD) coatings could offer the best of both worlds. Such hybridized architectures may allow for interfacial environments that are not only energetically optimized but also mechanically and chemically buffered paving the way for the kind of long-lived, high-efficiency tandem device needed for commercial viability.

In a broader context, the field must come to terms with the reality that interface engineering is not a "layer-by-layer" addition, but a systems-level challenge. The performance of an interfacial layer is inextricably linked to everything that comes before and after it like deposition methods, perovskite crystallization, adjacent transport layers, and even encapsulation strategies. As such, future work on SAMs and dipole interlayers must transcend material formulation and be embedded within holistic device engineering frameworks. In sum, SAMs and dipolar layers stand at a crossroad. Their track record in enhancing single-junction devices has been substantial; their potential in enabling the next generation of tandem photovoltaics is profound. But fulfilling this promise will require not incremental tweaking, but radical rethinking of their chemistry, their function, and their role within the device stack. It will also demand deeper collaboration between synthetic chemists, device physicists, and process engineers each bringing their perspective to the complex, multidimensional problem of interfacial design. If such convergence can be achieved, SAMs and dipolar layers may cease to be mere interfacial modifiers and instead become the molecular architects of a scalable solar future.

Conflicts of interest

There are no conflicts to declare.

Data availability

No primary research results, software or code have been included, and no new data were generated or analysed as part of this review.

Acknowledgements

References

1 M. Z. Jacobson, M. A. Delucchi, Z. A. F. Bauer, S. C. Goodman, W. E. Chapman, M. A. Cameron, C. Bozonnat, L. Chobadi, H. A. Clonts, P. Enevoldsen, J. R. Erwin, S. N. Fobi, O. K. Goldstrom, E. M. Hennessy, J. Liu, J. Lo, C. B. Meyer, S. B. Morris, K. R. Moy, P. L. O'Neill, I. Petkov, S. Redfern, R. Schucker, M. A. Sontag, J. Wang, E. Weiner and A. S. Yachanin, *Joule*, 2017, **1**, 108–121.

2 J. Zhao, A. Wang and M. A. Green, *Prog. Photovoltaics Res. Appl.*, 1999, **7**, 471–474.

3 M. A. Green, *Prog. Photovoltaics Res. Appl.*, 2009, **17**, 183–189.

4 G. Wang, Q. Su, H. Tang, H. Wu, H. Lin, C. Han, T. Wang, C. Xue, J. Lu, L. Fang, Z. Li, X. Xu and P. Gao, *Nat. Commun.*, 2024, **15**, 8931.

5 H. Wu, F. Ye, M. Yang, F. Luo, X. Tang, Q. Tang, H. Qiu, Z. Huang, G. Wang, Z. Sun, H. Lin, J. Wei, Y. Li, X. Tian, J. Zhang, L. Xie, X. Deng, T. Yuan, M. Yu, Y. Liu, P. Li, H. Chen, S. Zhou, Q. Xu, P. Li, J. Duan, J. Chen, C. Li, S. Yin, B. Liu, C. Sun, Q. Su, Y. Wang, H. Deng, T. Xie, P. Gao, Q. Kang, Y. Zhang, H. Yan, N. Yuan, F. Peng, Y. Yuan, X. Ru, B. He, L. Chen, J. Wang, J. Lu, M. Qu, C. Xue, J. Ding, L. Fang, Z. Li and X. Xu, *Nature*, 2024, **635**, 604–609.

6 W. Shockley and H. J. Queisser, *J. Appl. Phys.*, 1961, **32**, 510–519.

7 R. M. Swanson, in *Conference Record of the Thirty-first IEEE Photovoltaic Specialists Conference*, 2005, pp. 889–894.

8 S. De Wolf, J. Holovsky, S. J. Moon, P. Löper, B. Niesen, M. Ledinsky, F. J. Haug, J. H. Yum and C. Ballif, *J. Phys. Chem. Lett.*, 2014, **5**, 1035–1039.

9 A. Richter, S. W. Glunz, F. Werner, J. Schmidt and A. Cuevas, *Phys. Rev. B: Condens. Matter Mater. Phys.*, 2012, **86**, 165202.

10 A. Richter, M. Hermle and S. W. Glunz, *IEEE J. Photovoltaics*, 2013, **3**, 1184–1191.

11 H. Li and W. Zhang, *Chem. Rev.*, 2020, **120**, 9835–9950.

12 M. Taguchi, A. Yano, S. Tohoda, K. Matsuyama, Y. Nakamura, T. Nishiwaki, K. Fujita and E. Maruyama, *IEEE J. Photovoltaics*, 2014, **4**, 96–99.

13 Q. Chen, L. Zhou, J. Zhang, D. Chen, W. Zhu, H. Xi, J. Zhang, C. Zhang and Y. Hao, *Nanomaterials*, 2024, **14**(2), 202.

14 M. A. Green, E. D. Dunlop, M. Yoshita, N. Kopidakis, K. Bothe, G. Siefer and X. Hao, *Prog. Photovoltaics Res. Appl.*, 2024, **32**, 3–13.

15 S. D. Stranks, G. E. Eperon, G. Grancini, C. Menelaou, M. J. P. Alcocer, T. Leijtens, L. M. Herz, A. Petrozza and H. J. Snaith, *Science*, 2013, **342**, 341–344.

16 L. M. Pazos-Outón, M. Szumilo, R. Lamboll, J. M. Richter, M. Crespo-Quesada, M. Abdi-Jalebi, H. J. Beeson, M. Vrućinić, M. Alsari, H. J. Snaith, B. Ehrler, R. H. Friend and F. Deschler, *Science*, 2016, **351**, 1430–1433.

17 E. Edri, S. Kirmayer, S. Mukhopadhyay, K. Gartsman, G. Hodes and D. Cahen, *Nat. Commun.*, 2014, **5**, 3461.

18 P. Schulz, *ACS Energy Lett.*, 2018, **3**, 1287–1293.

19 C. Jacoboni, C. Canali, G. Ottaviani and A. Alberigi Quaranta, *Solid State Electron*, 1977, **20**, 77–89.

20 A. Kojima, K. Teshima, Y. Shirai and T. Miyasaka, *J. Am. Chem. Soc.*, 2009, **131**, 6050–6051.

21 J.-H. Im, C.-R. Lee, J.-W. Lee, S.-W. Park and N.-G. Park, *Nanoscale*, 2011, **3**, 4088–4093.

22 M. M. Lee, J. Teuscher, T. Miyasaka, T. N. Murakami and H. J. Snaith, *Science*, 2012, **338**, 643–647.

23 B. Wang, X. Xiao and T. Chen, *Nanoscale*, 2014, **6**, 12287–12297.

24 P. Löper, S.-J. Moon, S. Martín de Nicolas, B. Niesen, M. Ledinsky, S. Nicolay, J. Bailat, J.-H. Yum, S. De Wolf and C. Ballif, *Phys. Chem. Chem. Phys.*, 2015, **17**, 1619–1629.

25 C. D. Bailie, M. G. Christoforo, J. P. Mailoa, A. R. Bowring, E. L. Unger, W. H. Nguyen, J. Burschka, N. Pellet, J. Z. Lee, M. Grätzel, R. Noufi, T. Buonassisi, A. Salleo and M. D. McGehee, *Energy Environ. Sci.*, 2015, **8**, 956–963.

26 J. P. Mailoa, C. D. Bailie, E. C. Johlin, E. T. Hoke, A. J. Akey, W. H. Nguyen, M. D. McGehee and T. Buonassisi, *Appl. Phys. Lett.*, 2015, **106**(12), 121105.

27 S. Albrecht, M. Saliba, J. P. Correa Baena, F. Lang, L. Kegelmann, M. Mews, L. Steier, A. Abate, J. Rappich, L. Korte, R. Schlatmann, M. K. Nazeeruddin, A. Hagfeldt, M. Grätzel and B. Rech, *Energy Environ. Sci.*, 2016, **9**, 81–88.

28 J. Werner, C.-H. Weng, A. Walter, L. Fesquet, J. P. Seif, S. De Wolf, B. Niesen and C. Ballif, *J. Phys. Chem. Lett.*, 2016, **7**, 161–166.

29 J. Werner, L. Barraud, A. Walter, M. Bräuninger, F. Sahli, D. Sacchetto, N. Tétreault, B. Paviet-Salomon, S.-J. Moon, C. Allebé, M. Despeisse, S. Nicolay, S. De Wolf, B. Niesen and C. Ballif, *ACS Energy Lett.*, 2016, **1**, 474–480.

30 A. W. Y. Ho-Baillie, J. Zheng, M. A. Mahmud, F.-J. Ma, D. R. McKenzie and M. A. Green, *Appl. Phys. Rev.*, 2021, **8**, 41307.

31 G. E. Eperon, M. T. Hörantner and H. J. Snaith, *Nat. Rev. Chem.*, 2017, **1**, 95.

32 R. Prasanna, A. Gold-Parker, T. Leijtens, B. Conings, A. Babayigit, H.-G. Boyen, M. F. Toney and M. D. McGehee, *J. Am. Chem. Soc.*, 2017, **139**, 11117–11124.

33 A. Amat, E. Mosconi, E. Ronca, C. Quarti, P. Umari, M. K. Nazeeruddin, M. Grätzel and F. De Angelis, *Nano Lett.*, 2014, **14**, 3608–3616.

34 M. G. Goesten and R. Hoffmann, *J. Am. Chem. Soc.*, 2018, **140**, 12996–13010.

35 R. G. Niemann, L. Gouda, J. Hu, S. Tirosh, R. Gottesman, P. J. Cameron and A. Zaban, *J. Mater. Chem. A*, 2016, **4**, 17819–17827.

36 D. P. McMeekin, G. Sadoughi, W. Rehman, G. E. Eperon, M. Saliba, M. T. Hörantner, A. Haghighirad, N. Sakai, L. Korte, B. Rech, M. B. Johnston, L. M. Herz and H. J. Snaith, *Science*, 2016, **351**, 151–155.

37 E. L. Unger, L. Kegelmann, K. Suchan, D. Sörell, L. Korte and S. Albrecht, *J. Mater. Chem. A*, 2017, **5**, 11401–11409.

38 C. M. Wolff, P. Caprioglio, M. Stolterfoht and D. Neher, *Adv. Mater.*, 2019, **31**, 1902762.

39 L. Krückemeier, U. Rau, M. Stolterfoht and T. Kirchartz, *Adv. Energy Mater.*, 2020, **10**, 1902573.

40 R. Prasanna, T. Leijtens, S. P. Dunfield, J. A. Raiford, E. J. Wolf, S. A. Swifter, J. Werner, G. E. Eperon, C. de Paula, A. F. Palmstrom, C. C. Boyd, M. F. A. M. van Hest, S. F. Bent, G. Teeter, J. J. Berry and M. D. McGehee, *Nat. Energy*, 2019, **4**, 939–947.

41 Y. Lin, B. Chen, F. Zhao, X. Zheng, Y. Deng, Y. Shao, Y. Fang, Y. Bai, C. Wang and J. Huang, *Adv. Mater.*, 2017, **29**, 1700607.

42 Y. Wu, D. Yan, J. Peng, T. Duong, Y. Wan, S. P. Phang, H. Shen, N. Wu, C. Barugkin, X. Fu, S. Surve, D. Grant, D. Walter, T. P. White, K. R. Catchpole and K. J. Weber, *Energy Environ. Sci.*, 2017, **10**, 2472–2479.

43 R. Fan, N. Zhou, L. Zhang, R. Yang, Y. Meng, L. Li, T. Guo, Y. Chen, Z. Xu, G. Zheng, Y. Huang, L. Li, L. Qin, X. Qiu, Q. Chen and H. Zhou, *Sol. RRL*, 2017, **1**, 1700149.

44 A. Al-Ashouri, E. Köhnen, B. Li, A. Magomedov, H. Hempel, P. Caprioglio, J. A. Márquez, A. B. Morales Vilches, E. Kasparavicius, J. A. Smith, N. Phung, D. Menzel, M. Grischek, L. Kegelmann, D. Skroblin, C. Gollwitzer, T. Malinauskas, M. Jošt, G. Matič, B. Rech, R. Schlatmann, M. Topič, L. Korte, A. Abate, B. Stannowski, D. Neher, M. Stolterfoht, T. Unold, V. Getautis and S. Albrecht, *Science*, 2020, **370**, 1300–1309.

45 B. Chen, Z. Yu, K. Liu, X. Zheng, Y. Liu, J. Shi, D. Spronk, P. N. Rudd, Z. Holman and J. Huang, *Joule*, 2019, **3**, 177–190.

46 H. Shen, S. T. Omelchenko, D. A. Jacobs, S. Yalamanchili, Y. Wan, D. Yan, P. Phang, T. Duong, Y. Wu, Y. Yin, C. Samundsett, J. Peng, N. Wu, T. P. White, G. G. Andersson, N. S. Lewis and K. R. Catchpole, *Sci. Adv.*, 2025, **4**, eaau9711.

47 J. Zheng, C. F. J. Lau, H. Mehrvarz, F.-J. Ma, Y. Jiang, X. Deng, A. Soeriyadi, J. Kim, M. Zhang, L. Hu, X. Cui, D. S. Lee, J. Bing, Y. Cho, C. Chen, M. A. Green, S. Huang and A. W. Y. Ho-Baillie, *Energy Environ. Sci.*, 2018, **11**, 2432–2443.

48 K. A. Bush, A. F. Palmstrom, Z. J. Yu, M. Boccard, R. Cheacharoen, J. P. Mailoa, D. P. McMeekin, R. L. Z. Hoye, C. D. Bailie, T. Leijtens, I. M. Peters, M. C. Minichetti, N. Rolston, R. Prasanna, S. Sofia, D. Harwood, W. Ma, F. Moghadam, H. J. Snaith, T. Buonassisi, Z. C. Holman, S. F. Bent and M. D. McGehee, *Nat. Energy*, 2017, **2**, 17009.

49 K. A. Bush, S. Manzoor, K. Frohna, Z. J. Yu, J. A. Raiford, A. F. Palmstrom, H.-P. Wang, R. Prasanna, S. F. Bent, Z. C. Holman and M. D. McGehee, *ACS Energy Lett.*, 2018, **3**, 2173–2180.

50 C. U. Kim, J. C. Yu, E. D. Jung, I. Y. Choi, W. Park, H. Lee, I. Kim, D.-K. Lee, K. K. Hong, M. H. Song and K. J. Choi, *Nano Energy*, 2019, **60**, 213–221.

51 G. Nogay, F. Sahli, J. Werner, R. Monnard, M. Boccard, M. Despeisse, F.-J. Haug, Q. Jeangros, A. Ingenito and C. Ballif, *ACS Energy Lett.*, 2019, **4**, 844–845.

52 L. Mazzarella, Y.-H. Lin, S. Kirner, A. B. Morales-Vilches, L. Korte, S. Albrecht, E. Crossland, B. Stannowski, C. Case, H. J. Snaith and R. Schlatmann, *Adv. Energy Mater.*, 2019, **9**, 1803241.

53 Y. Hou, E. Aydin, M. De Bastiani, C. Xiao, F. H. Isikgor, D.-J. Xue, B. Chen, H. Chen, B. Bahrami, A. H. Chowdhury, A. Johnston, S.-W. Baek, Z. Huang, M. Wei, Y. Dong, J. Troughton, R. Jalmood, A. J. Mirabelli, T. G. Allen, E. Van Kerschaver, M. I. Saidaminov, D. Baran, Q. Qiao, K. Zhu, S. De Wolf and E. H. Sargent, *Science*, 2020, **367**, 1135–1140.

54 T. S. Sherkar, C. Momblona, L. Gil-Escrig, J. Ávila, M. Sessolo, H. J. Bolink and L. J. A. Koster, *ACS Energy Lett.*, 2017, **2**, 1214–1222.

55 G.-W. Kim and A. Petrozza, *Adv. Energy Mater.*, 2020, **10**, 2001959.

56 C. Zhao, H. Zhang, A. Krishna, J. Xu and J. Yao, *Adv. Opt. Mater.*, 2024, **12**, 2301949.

57 Q. Wang, Q. Dong, T. Li, A. Gruverman and J. Huang, *Adv. Mater.*, 2016, **28**, 6734–6739.

58 P. Caprioglio, M. Stolterfoht, C. M. Wolff, T. Unold, B. Rech, S. Albrecht and D. Neher, *Adv. Energy Mater.*, 2019, **9**, 1901631.

59 P. V. Kamat, *ACS Energy Lett.*, 2018, **3**, 28–29.

60 R. Brendel and R. Peibst, *IEEE J. Photovoltaics*, 2016, **6**, 1413–1420.

61 J. Werner, B. Niesen and C. Ballif, *Adv. Mater. Interfaces*, 2018, **5**, 1700731.

62 M. Stolterfoht, P. Caprioglio, C. M. Wolff, J. A. Márquez, J. Nordmann, S. Zhang, D. Rothhardt, U. Hörmann, Y. Amir, A. Redinger, L. Kegelmann, F. Zu, S. Albrecht, N. Koch, T. Kirchartz, M. Saliba, T. Unold and D. Neher, *Energy Environ. Sci.*, 2019, **12**, 2778–2788.

63 K. Choi, J. Lee, H. Il Kim, C. W. Park, G.-W. Kim, H. Choi, S. Park, S. A. Park and T. Park, *Energy Environ. Sci.*, 2018, **11**, 3238–3247.

64 S. Shao and M. A. Loi, *Adv. Mater. Interfaces*, 2020, **7**, 1901469.

65 J. Xia, M. Sohail and M. K. Nazeeruddin, *Adv. Mater.*, 2023, **35**, 2211324.

66 P. Schulz, D. Cahen and A. Kahn, *Chem. Rev.*, 2019, **119**, 3349–3417.

67 C. Ran, J. Xu, W. Gao, C. Huang and S. Dou, *Chem. Soc. Rev.*, 2018, **47**, 4581–4610.

68 W.-J. Yin, T. Shi and Y. Yan, *Appl. Phys. Lett.*, 2014, **104**, 63903.

69 J. Wang, G. Jin, Q. Zhen, C. He and Y. Duan, *Adv. Mater. Interfaces*, 2021, **8**, 2002078.

70 H. Ishii, K. Sugiyama, E. Ito and K. Seki, *Adv. Mater.*, 1999, **11**, 605–625.

71 D. Cahen and A. Kahn, *Adv. Mater.*, 2003, **15**, 271–277.

72 A. Kahn, *Mater. Horizons*, 2016, **3**, 7–10.

73 A. Kahn, *Mater. Horizons*, 2016, **3**, 7–10.

74 J. Shi, X. Xu, D. Li and Q. Meng, *Small*, 2015, **11**, 2472–2486.

75 N. F. Mott, *Math. Proc. Cambridge Philos. Soc.*, 1938, **34**, 568–572.

76 W. Schottky, *Naturwissenschaften*, 1938, **26**, 843.

77 R. L. Anderson, *IBM J. Res. Dev.*, 1960, **4**, 283–287.

78 P. Schulz, E. Edri, S. Kirmayer, G. Hodes, D. Cahen and A. Kahn, *Energy Environ. Sci.*, 2014, **7**, 1377–1381.

79 Z. Zhou, S. Pang, Z. Liu, H. Xu and G. Cui, *J. Mater. Chem. A*, 2015, **3**, 19205–19217.

80 T. C. Sum, S. Chen, G. Xing, X. Liu and B. Wu, *Nanotechnology*, 2015, **26**, 342001.

81 S. Zhang, F. Ren, Z. Sun, X. Liu, Z. Tan, W. Liu, R. Chen, Z. Liu and W. Chen, *Small Methods*, 2024, **8**, 2301223.

82 F. H. Isikgor, S. Zhumagali, L. V. T. Merino, M. De Bastiani, I. McCulloch and S. De Wolf, *Nat. Rev. Mater.*, 2023, **8**, 89–108.

83 Y. Li, H. Xie, E. L. Lim, A. Hagfeldt and D. Bi, *Adv. Energy Mater.*, 2022, **12**, 2102730.

84 H. Lu, A. Krishna, S. M. Zakeeruddin, M. Grätzel and A. Hagfeldt, *iScience*, 2020, **23**(8), 101359.

85 Z. Guo, Z. Wu, Y. Chen, S. Wang and W. Huang, *J. Mater. Chem. C*, 2022, **10**, 13611–13645.

86 S. Wafee, B. H. Liu and C.-C. Leu, *Mater. Today Energy*, 2021, **22**, 100847.

87 M. Vasilopoulou, A. Fakharuddin, A. G. Coutsolelos, P. Falaras, P. Argitis, A. R. b. M. Yusoff and M. K. Nazeeruddin, *Chem. Soc. Rev.*, 2020, **49**, 4496–4526.

88 L. K. Ono and Y. Qi, *J. Phys. Chem. Lett.*, 2016, **7**, 4764–4794.

89 Y. Yu, J. Xia and Y. Liang, *AIP Adv.*, 2022, **12**, 55307.

90 Y. Li, Y. Zhao, Q. Chen, Y. Yang, Y. Liu, Z. Hong, Z. Liu, Y.-T. Hsieh, L. Meng, Y. Li and Y. Yang, *J. Am. Chem. Soc.*, 2015, **137**, 15540–15547.

91 W. Yan, W. Yang, K. Zhang, H. Yu, Y. Yang, H. Fan, Y. Qi and H. Xin, *ACS Omega*, 2022, **7**, 32383–32392.

92 W. Zhang, Q.-S. Li and Z.-S. Li, *Appl. Surf. Sci.*, 2021, **563**, 150267.

93 Q. Chen, H. Zhou, T.-B. Song, S. Luo, Z. Hong, H.-S. Duan, L. Dou, Y. Liu and Y. Yang, *Nano Lett.*, 2014, **14**, 4158–4163.

94 S.-H. Turren-Cruz, A. Hagfeldt and M. Saliba, *Science*, 2018, **362**, 449–453.

95 M. Saliba, T. Matsui, K. Domanski, J.-Y. Seo, A. Ummadisingu, S. M. Zakeeruddin, J.-P. Correa-Baena, W. R. Tress, A. Abate, A. Hagfeldt and M. Grätzel, *Science*, 2016, **354**, 206–209.

96 D. Bi, W. Tress, M. I. Dar, P. Gao, J. Luo, C. Renevier, K. Schenk, A. Abate, F. Giordano, J.-P. Correa Baena, J.-D. Decoppet, S. M. Zakeeruddin, M. K. Nazeeruddin, M. Grätzel and A. Hagfeldt, *Sci. Adv.*, 2016, **2**, e1501170.

97 F. Wang, W. Geng, Y. Zhou, H.-H. Fang, C.-J. Tong, M. A. Loi, L.-M. Liu and N. Zhao, *Adv. Mater.*, 2016, **28**, 9986–9992.

98 P. Caprioglio, D. S. Cruz, S. Caicedo-Dávila, F. Zu, A. A. Sutanto, F. Peña-Camargo, L. Kegelmann, D. Meggiolaro, L. Gregori, C. M. Wolff, B. Stiller, L. Perdigón-Toro, H. Köbler, B. Li, E. Gutierrez-Partida, I. Lauermann, A. Abate, N. Koch, F. De Angelis, B. Rech, G. Grancini, D. Abou-Ras, M. K. Nazeeruddin, M. Stolterfoht, S. Albrecht, M. Antonietti and D. Neher, *Energy Environ. Sci.*, 2021, **14**, 4508–4522.

99 N. K. Noel, A. Abate, S. D. Stranks, E. S. Parrott, V. M. Burlakov, A. Goriely and H. J. Snaith, *ACS Nano*, 2014, **8**, 9815–9821.

100 M. Yavari, M. Mazloum-Ardakani, S. Gholipour, M. M. Tavakoli, N. Taghavinia, A. Hagfeldt and W. Tress, *ACS Omega*, 2018, **3**, 5038–5043.

101 D. W. deQuilettes, S. Koch, S. Burke, R. K. Paranji, A. J. Shropshire, M. E. Ziffer and D. S. Ginger, *ACS Energy Lett.*, 2016, **1**, 438–444.

102 Y. Lin, L. Shen, J. Dai, Y. Deng, Y. Wu, Y. Bai, X. Zheng, J. Wang, Y. Fang, H. Wei, W. Ma, X. C. Zeng, X. Zhan and J. Huang, *Adv. Mater.*, 2017, **29**, 1604545.

103 C. Li, X. Wang, E. Bi, F. Jiang, S. M. Park, Y. Li, L. Chen, Z. Wang, L. Zeng, H. Chen, Y. Liu, C. R. Grice, A. Abudulimu, J. Chung, Y. Xian, T. Zhu, H. Lai, B. Chen, R. J. Ellingson, F. Fu, D. S. Ginger, Z. Song, E. H. Sargent and Y. Yan, *Science*, 2023, **379**, 690–694.

104 J. Kim and W. Jo, *Nano Convergence*, 2024, **11**, 57.

105 A. Singha, A. Paul, N. Gaur, H. S. Bilkhu, A. Arya, V. Bhalerao, S. Mallick, K. R. Balasubramaniam and D. Kabra, *Small*, 2025, 2502659.

106 H. Wang, L. Wang, T. Niu, W. Shang, X. Zhang, Z. Wan, X. Chen, W. Zhu, K. Wang, S. F. Liu and C. Zhang, *ACS Appl. Energy Mater.*, 2024, **7**, 8163–8172.

107 M. T. Hoang, Y. Yang, W. H. Chiu, Y. Yu, N. D. Pham, P. Moonie, A. Koplick, G. Tulloch, W. Martens and H. Wang, *Small Methods*, 2024, **8**, 2300431.

108 T. Luo, G. Ye, X. Chen, H. Wu, W. Zhang and H. Chang, *ACS Appl. Mater. Interfaces*, 2022, **14**, 42093–42101.

109 E. H. Jung, B. Chen, K. Bertens, M. Vafaie, S. Teale, A. Proppe, Y. Hou, T. Zhu, C. Zheng and E. H. Sargent, *ACS Energy Lett.*, 2020, **5**, 2796–2801.

110 H. Kim, K. Choi, G. W. Yoon, D. Kim, D. H. Lee, Y. Choi, H. S. Jung, S. Song and T. Park, *Adv. Energy Mater.*, 2024, **14**, 2401263.

111 M. Zhang, C. Peng, M. Zhu, W. Yan, H. Jiang, G. Nan, M. Li and Z. Zhou, *ACS Sustain. Chem. Eng.*, 2024, **12**, 3790–3799.

112 J.-H. Kim, Y. R. Kim, B. Park, S. Hong, I.-W. Hwang, J. Kim, S. Kwon, G. Kim, H. Kim and K. Lee, *Small*, 2021, **17**, 2005608.

113 S. Lee, J. H. Park, B. R. Lee, E. D. Jung, J. C. Yu, D. Di Nuzzo, R. H. Friend and M. H. Song, *J. Phys. Chem. Lett.*, 2017, **8**, 1784–1792.

114 M. J. Jeong, C. S. Moon, S. Lee, J. M. Im, M. Y. Woo, J. H. Lee, H. Cho, S. W. Jeon and J. H. Noh, *Joule*, 2023, **7**, 112–127.

115 T. Bu, J. Li, F. Zheng, W. Chen, X. Wen, Z. Ku, Y. Peng, J. Zhong, Y.-B. Cheng and F. Huang, *Nat. Commun.*, 2018, **9**, 4609.

116 R. He, Y. Wu, Z. Li, Y. Wang, W. Zhu, A. Tong, X. Chen, W. Pan, W. Sun and J. Wu, *Surf. Interfaces*, 2024, **48**, 104274.

117 J. Chen, H. Dong, J. Li, X. Zhu, J. Xu, F. Pan, R. Xu, J. Xi, B. Jiao, X. Hou, K. Wei NG, S.-P. Wang and Z. Wu, *ACS Energy Lett.*, 2022, **7**, 3685–3694.

118 T. Nie, Z. Fang, J. Ding and S. Liu, *Device*, 2024, **2**, 100498.

119 Y. Yang, R. Chen, J. Wu, Z. Dai, C. Luo, Z. Fang, S. Wan, L. Chao, Z. Liu and H. Wang, *Angew. Chemie Int. Ed.*, 2024, **63**, e202409689.

120 M. Du, S. Zhao, L. Duan, Y. Cao, H. Wang, Y. Sun, L. Wang, X. Zhu, J. Feng, L. Liu, X. Jiang, Q. Dong, Y. Shi, K. Wang and S. Liu, *Joule*, 2022, **6**, 1931–1943.

121 X. Lian, J. Chen, S. Shan, G. Wu and H. Chen, *ACS Appl. Mater. Interfaces*, 2020, **12**, 46340–46347.

122 T. Guo, Z. Fang, Z. Zhang, Z. Deng, R. Zhao, J. Zhang, M. Shang, X. Liu, Z. Hu, Y. Zhu and L. Han, *J. Energy Chem.*, 2022, **69**, 211–220.

123 A. R. M. Alghamdi, M. Yanagida, Y. Shirai, G. G. Andersson and K. Miyano, *ACS Omega*, 2022, **7**, 12147–12157.

124 A. Ulman, *Chem. Rev.*, 1996, **96**, 1533–1554.

125 F. Ali, C. Roldán-Carmona, M. Sohail and M. K. Nazeeruddin, *Adv. Energy Mater.*, 2020, **10**, 2002989.

126 S. A. DiBenedetto, A. Facchetti, M. A. Ratner and T. J. Marks, *Adv. Mater.*, 2009, **21**, 1407–1433.

127 A. Abrusci, S. D. Stranks, P. Docampo, H.-L. Yip, A. K.-Y. Jen and H. J. Snaith, *Nano Lett.*, 2013, **13**, 3124–3128.

128 K. Wojciechowski, S. D. Stranks, A. Abate, G. Sadoughi, A. Sadhanala, N. Kopidakis, G. Rumbles, C.-Z. Li, R. H. Friend, A. K.-Y. Jen and H. J. Snaith, *ACS Nano*, 2014, **8**, 12701–12709.

129 A. Magomedov, A. Al-Ashouri, E. Kasparavičius, S. Strazdaite, G. Niaura, M. Jošt, T. Malinauskas, S. Albrecht and V. Getautis, *Adv. Energy Mater.*, 2018, **8**, 1801892.

130 A. Al-Ashouri, A. Magomedov, M. Roß, M. Jošt, M. Talaikis, G. Chistiakova, T. Bertram, J. A. Márquez, E. Köhnen, E. Kasparavičius, S. Levcenco, L. Gil-Escrig, C. J. Hages, R. Schlatmann, B. Rech, T. Malinauskas, T. Unold, C. A. Kaufmann, L. Korte, G. Niaura, V. Getautis and S. Albrecht, *Energy Environ. Sci.*, 2019, **12**, 3356–3369.

131 J. M. Ramón, J. G. Sánchez, M. Más-Montoya, W. Li, E. Martínez-Ferrero, E. Palomares and D. Curiel, *Small*, 2025, 2500067.

132 Q. Chen, K. Sun, L. R. Franco, J. Wu, L. Öhrström, X. Liu, M. Gumbo, M. S. Ozório, C. M. Araujo, G. Zhang, A. Johansson, E. Moons, M. Fahlman, D. Yu, Y. Wang and E. Wang, *Adv. Sci.*, 2025, **12**, e2410277.

133 Z. Ren, Z. Cui, X. Shi, L. Wang, Y. Dou, F. Wang, H. Lin, H. Yan and S. Chen, *Joule*, 2023, **7**, 2894–2904.

134 S. M. Sze and K. K. Ng, *Physics of Semiconductor Devices*, 2006, 77–133.

135 S. M. Sze, K. Kwok, *Physics of Semiconductor Devices*, 2006, 134–196.

136 R. T. Tung, *Appl. Phys. Rev.*, 2014, **1**, 11304.

137 E. H. Rhoderick and R. H. Williams, *Metal-Semiconductor Contacts*, Clarendon Press, 1988.

138 Z. Zhang and J. T. J. Yates, *Chem. Rev.*, 2012, **112**, 5520–5551.

139 T. Abu-Husein, S. Schuster, D. A. Egger, M. Kind, T. Santowski, A. Wiesner, R. Chiechi, E. Zojer, A. Terfort and M. Zharnikov, *Adv. Funct. Mater.*, 2015, **25**, 3943–3957.

140 H. Vázquez, Y. J. Dappe, J. Ortega and F. Flores, *J. Chem. Phys.*, 2007, **126**, 144703.

141 H. Vázquez, W. Gao, F. Flores and A. Kahn, *Phys. Rev. B: Condens. Matter Mater. Phys.*, 2005, **71**, 41306.

142 H. Vázquez, F. Flores and A. Kahn, *Org. Electron.*, 2007, **8**, 241–248.

143 A. Vilan and D. Cahen, *Chem. Rev.*, 2017, **117**, 4624–4666.

144 H. C. Card and E. H. Rhoderick, *J. Phys. D. Appl. Phys.*, 1971, **4**, 1589.

145 A. M. Cowley and S. M. Sze, *J. Appl. Phys.*, 1965, **36**, 3212–3220.

146 L. Brillson, *Surf. Sci. Rep.*, 1982, **2**, 123–326.

147 J. Tersoff, *Phys. Rev. Lett.*, 1984, **52**, 465–468.

148 M. Jošt, L. Kegelmann, L. Korte and S. Albrecht, *Adv. Energy Mater.*, 2020, **10**, 1904102.

149 A. Rajagopal, K. Yao and A. K.-Y. Jen, *Adv. Mater.*, 2018, **30**, 1800455.

150 S. A. U. Hasan, M. A. Zahid, S. Park and J. Yi, *Sol. RRL*, 2024, **8**, 2300967.

151 K. Artuk, D. Turkay, M. D. Mensi, J. A. Steele, D. A. Jacobs, M. Othman, X. Yu Chin, S.-J. Moon, A. N. Tiwari, A. Hessler-Wyser, Q. Jeangros, C. Ballif and C. M. Wolff, *Adv. Mater.*, 2024, **36**, 2311745.

152 D. Khan, G. Qu, I. Muhammad, Z. Tang and Z.-X. Xu, *Adv. Energy Mater.*, 2023, **13**, 2302124.

153 C. O. Ramírez Quiroz, G. D. Spyropoulos, M. Salvador, L. M. Roch, M. Berlinghof, J. Darío Perea, K. Forberich, L.-I. Dion-Bertrand, N. J. Schrenker, A. Classen, N. Gasparini, G. Chistiakova, M. Mews, L. Korte, B. Rech, N. Li, F. Hauke, E. Spiecker, T. Ameri, S. Albrecht, G. Abellán, S. León, T. Unruh, A. Hirsch, A. Aspuru-Guzik and C. J. Brabec, *Adv. Funct. Mater.*, 2019, **29**, 1901476.

154 Y. Cheng and L. Ding, *SusMat*, 2021, **1**, 324–344.

155 J. Suo, B. Yang, D. Bogachuk, G. Boschloo and A. Hagfeldt, *Adv. Energy Mater.*, 2025, **15**, 2400205.

156 Y. Ma, J. Gong, P. Zeng and M. Liu, *Nano-Micro Lett.*, 2023, **15**, 173.

157 Z. Yi, X. Li, Y. Xiong, G. Shen, W. Zhang, Y. Huang, Q. Jiang, X. R. Ng, Y. Luo, J. Zheng, W. L. Leong, F. Fu, T. Bu and J. Yang, *Interdiscip. Mater.*, 2024, **3**, 203–244.

158 Q. Chen, C. Wang, Y. Li and L. Chen, *J. Am. Chem. Soc.*, 2020, **142**, 18281–18292.

159 F. Sadegh, E. Akman, D. Prochowicz, M. M. Tavakoli, P. Yadav and S. Akin, *ACS Appl. Mater. Interfaces*, 2022, **14**, 38631–38641.

160 D. Yeo, J. Shin, D. Kim, J. Y. Jaung and I. H. Jung, *Nanomaterials*, 2024, **14**(2), 175.

161 J. Zhang, Y. Sun and H. Yu, *Chem. Eng. J.*, 2022, **431**, 133948.

162 D. Akın Kara, K. Kara, G. Oylumluoglu, M. Z. Yigit, M. Can, J. J. Kim, E. K. Burnett, D. L. Gonzalez Arellano, S. Buyukcelebi, F. Ozel, O. Usluer, A. L. Briseno and M. Kus, *ACS Appl. Mater. Interfaces*, 2018, **10**, 30000–30007.

163 S. Y. Kim, S. J. Cho, S. E. Byeon, X. He and H. J. Yoon, *Adv. Energy Mater.*, 2020, **10**, 2002606.

164 K. Dong, G. Yang, M. Wang, J. Bian, L. Zhu, F. Zhang, S. Yu, S. Liu, J.-D. Xiao, X. Guo and X. Jiang, *ChemSusChem*, 2024, **17**, e202301497.

165 K. Choi, H. Choi, J. Min, T. Kim, D. Kim, S. Y. Son, G.-W. Kim, J. Choi and T. Park, *Sol. RRL*, 2020, **4**, 1900251.

166 A. Natan, L. Kronik, H. Haick and R. T. Tung, *Adv. Mater.*, 2007, **19**, 4103–4117.

167 O. L. A. Monti, *J. Phys. Chem. Lett.*, 2012, **3**, 2342–2351.

168 S. M. Sze and K. K. Ng, *Physics of Semiconductor Devices*, 2006, 5–7.

169 A. Vilan, J. Ghabboun and D. Cahen, *J. Phys. Chem. B*, 2003, **107**, 6360–6376.

170 J. Thiesbrummel, F. Peña-Camargo, K. O. Brinkmann, E. Gutierrez-Partida, F. Yang, J. Warby, S. Albrecht, D. Neher, T. Riedl, H. J. Snaith, M. Stolterfoht and F. Lang, *Adv. Energy Mater.*, 2023, **13**, 2202674.

171 H. Lai, J. Luo, Y. Zwirner, S. Olthof, A. Wieczorek, F. Ye, Q. Jeangros, X. Yin, F. Akhundova, T. Ma, R. He, R. K. Kothandaraman, X. Chin, E. Gilshtein, A. Müller, C. Wang, J. Thiesbrummel, S. Siol, J. M. Prieto, T. Unold, M. Stolterfoht, C. Chen, A. N. Tiwari, D. Zhao and F. Fu, *Adv. Energy Mater.*, 2022, **12**, 2202438.

172 L. Li, Y. Wang, X. Wang, R. Lin, X. Luo, Z. Liu, K. Zhou, S. Xiong, Q. Bao, G. Chen, Y. Tian, Y. Deng, K. Xiao, J. Wu, M. I. Saidaminov, H. Lin, C.-Q. Ma, Z. Zhao, Y. Wu, L. Zhang and H. Tan, *Nat. Energy*, 2022, **7**, 708–717.

173 W. Wang, X. Liu, J. Wang, C. Chen, J. Yu, D. Zhao and W. Tang, *Adv. Energy Mater.*, 2023, **13**, 2300694.

174 R. He, W. Wang, Z. Yi, F. Lang, C. Chen, J. Luo, J. Zhu, J. Thiesbrummel, S. Shah, K. Wei, Y. Luo, C. Wang, H. Lai, H. Huang, J. Zhou, B. Zou, X. Yin, S. Ren, X. Hao, L. Wu, J. Zhang, J. Zhang, M. Stolterfoht, F. Fu, W. Tang and D. Zhao, *Nature*, 2023, **618**, 80–86.

175 Q. Jiang, J. Tong, R. A. Scheidt, X. Wang, A. E. Louks, Y. Xian, R. Tirawat, A. F. Palmstrom, M. P. Hautzinger, S. P. Harvey, S. Johnston, L. T. Schelhas, B. W. Larson, E. L. Warren, M. C. Beard, J. J. Berry, Y. Yan and K. Zhu, *Science*, 2022, **378**, 1295–1300.

176 H. Chen, A. Maxwell, C. Li, S. Teale, B. Chen, T. Zhu, E. Ugur, G. Harrison, L. Grater, J. Wang, Z. Wang, L. Zeng, S. M. Park, L. Chen, P. Serles, R. A. Awni, B. Subedi, X. Zheng, C. Xiao, N. J. Podraza, T. Filleter, C. Liu, Y. Yang, J. M. Luther, S. De Wolf, M. G. Kanatzidis, Y. Yan and E. H. Sargent, *Nature*, 2023, **613**, 676–681.

177 Y. Ou, H. Huang, H. Shi, Z. Li, Z. Chen, M. Mateen, Z. Lu, D. Chi and S. Huang, *Chem. Eng. J.*, 2023, **469**, 143860.

178 F. H. Isikgor, F. Furlan, J. Liu, E. Ugur, M. K. Eswaran, A. S. Subbiah, E. Yengel, M. De Bastiani, G. T. Harrison, S. Zhumagali, C. T. Howells, E. Aydin, M. Wang, N. Gasparini, T. G. Allen, A. ur Rehman, E. Van Kerschaver, D. Baran, I. McCulloch, T. D. Anthopoulos, U. Schwingenschlögl, F. Laquai and S. De Wolf, *Joule*, 2021, **5**, 1566–1586.

179 L. Zheng, Y. Xuan, J. Wang, S. Bao, X. Liu and K. Zhang, *J. Mater. Chem. A*, 2022, **10**, 7251–7262.

180 Z. Ying, Z. Yang, J. Zheng, H. Wei, L. Chen, C. Xiao, J. Sun, C. Shou, G. Qin, J. Sheng, Y. Zeng, B. Yan, X. Yang and J. Ye, *Joule*, 2022, **6**, 2644–2661.

181 R. Mishima, M. Hino, M. Kanematsu, K. Kishimoto, H. Ishibashi, K. Konishi, S. Okamoto, T. Irie, T. Fujimoto, W. Yoshida, H. Uzu, D. Adachi and K. Yamamoto, *Appl. Phys. Express*, 2022, **15**, 76503.

182 G. Wang, J. Zheng, W. Duan, J. Yang, M. A. Mahmud, Q. Lian, S. Tang, C. Liao, J. Bing, J. Yi, T. L. Leung, X. Cui, H. Chen, F. Jiang, Y. Huang, A. Lambertz, M. Jankovec, M. Topič, S. Bremner, Y.-Z. Zhang, C. Cheng, K. Ding and A. Ho-Baillie, *Joule*, 2023, **7**, 2583–2594.

183 Z. Liu, C. Zhu, H. Luo, W. Kong, X. Luo, J. Wu, C. Ding, Y. Chen, Y. Wang, J. Wen, Y. Gao and H. Tan, *Adv. Energy Mater.*, 2023, **13**, 2203230.

184 X. Y. Chin, D. Turkay, J. A. Steele, S. Tabean, S. Eswara, M. Mensi, P. Fiala, C. M. Wolff, A. Paracchino, K. Artuk, D. Jacobs, Q. Guesnay, F. Sahli, G. Andreatta, M. Boccard, Q. Jeangros and C. Ballif, *Science*, 2023, **381**, 59–63.

185 S. Mariotti, E. Köhnen, F. Scheler, K. Sveinbjörnsson, L. Zimmermann, M. Piot, F. Yang, B. Li, J. Warby, A. Musiienko, D. Menzel, F. Lang, S. Keßler, I. Levine, D. Mantione, A. Al-Ashouri, M. S. Härtel, K. Xu, A. Cruz, J. Kurpiers, P. Wagner, H. Köbler, J. Li, A. Magomedov, D. Mecerreyes, E. Unger, A. Abate, M. Stolterfoht, B. Stannowski, R. Schlatmann, L. Korte and S. Albrecht, *Science*, 2023, **381**, 63–69.

186 NREL, Best Research-Cell Efficiency Chart, https://www2.nrel.gov/pv/cell-efficiency.

187 E. Bellini, Longi claims 33.9% efficiency for perovskite-silicon tandem solar cell, https://www.pv-magazine.com/2025/01/06/jinkosolar-claims-33-84-efficiency-for-perovskite-silicon-tandem-solar-cell/.

188 A. Harter, K. Artuk, F. Mathies, O. Karalis, H. Hempel, A. Al-Ashouri, S. Albrecht, R. Schlatmann, C. Ballif, B. Stannowski and C. M. Wolff, *ACS Appl. Mater. Interfaces*, 2024, **16**, 62817–62826.

189 B. P. Kore, O. Er-raji, O. Fischer, A. Callies, O. Schultz-Wittmann, P. S. C. Schulze, M. Bivour, S. De Wolf, S. W. Glunz and J. Borchert, *Energy Environ. Sci.*, 2025, **18**, 354–366.

190 S. Zhang, J. Wang, N. Kalasariya, P. Dally, C. Deger, I. Yavuz, A. Razzaq, B. Vishal, A. Prasetio, D. S. Utomo, O. Karalis, H. Hempel, V. Hnapovskyi, Q. Liu, M. Babics, A. A. Said, A. Pininti, M. Stolterfoht and S. De Wolf, *ACS Energy Lett.*, 2024, **9**, 4633–4644.

191 O. Er-Raji, S. Lange, C. E. Hartwig, A. Prasetio, M. Bivour, M. Hermle, M. Turek, S. De Wolf, S. W. Glunz, J. Borchert and P. S. C. Schulze, *Small Methods*, 2025, 2401758.

192 A. P. Hinckley and A. J. Muscat, *Langmuir*, 2020, **36**, 2563–2573.

193 T. Wu, M. Zhang, X. Gao, H. Shen, X. Liu, Z. Li, J. Xu and X. Hao, *ACS Nano*, 2025, **19**, 24508–24535.

194 S. Huang, C. Liang and Z. Lin, *ACS Appl. Mater. Interfaces*, 2024, **16**, 64424–64446.

195 W. Li, E. Martínez-Ferrero and E. Palomares, *Mater. Chem. Front.*, 2024, **8**, 681–699.

196 M. Azam, T. Du, Z. Wan, H. Zhao, H. Zeng, R. Wei, C. J. Brabec, J. Luo and C. Jia, *Energy Environ. Sci.*, 2024, **17**, 6974–7016.

197 J.-H. Lee, J. Kim, G. Kim, D. Shin, S. Y. Jeong, J. Lee, S. Hong, J. W. Choi, C.-L. Lee, H. Kim, Y. Yi and K. Lee, *Energy Environ. Sci.*, 2018, **11**, 1742–1751.

198 Y. Yang, C. Liu, Y. Ding, Z. Arain, S. Wang, X. Liu, T. Hayat, A. Alsaedi and S. Dai, *ACS Appl. Mater. Interfaces*, 2019, **11**, 34964–34972.

199 W.-H. Lee, C.-Y. Chen, C.-S. Li, S.-Y. Hsiao, W.-L. Tsai, M.-J. Huang, C.-H. Cheng, C.-I. Wu and H.-W. Lin, *Nano Energy*, 2017, **38**, 66–71.

200 K.-G. Lim, S. Ahn and T.-W. Lee, *J. Mater. Chem. C*, 2018, **6**, 2915–2924.

201 G. Heimel, L. Romaner, E. Zojer and J.-L. Bredas, *Acc. Chem. Res.*, 2008, **41**, 721–729.

202 K.-G. Lim, S. M. Park, H. Y. Woo and T.-W. Lee, *ChemSusChem*, 2015, **8**, 3062–3068.

203 J. Heo, J. A. Prayogo, S. W. Lee, H. Park, S. Muthu, J. Hong, H. Kim, Y.-H. Kim, D. R. Whang, D. W. Chang and H. J. Park, *Small*, 2024, **20**, 2404784.

204 Y. Wu, B. Chang, L. Wang, H. Li, L. Pan, Z. Liu and L. Yin, *Adv. Mater.*, 2023, **35**, e2300174.

205 G. Wang, W. Duan, Q. Lian, M. A. Mahmud, T. L. Leung, C. Liao, J. Bing, C. Bailey, J. Yi, R. Tao, J. Yang, X. Cui, S. Nie, Y. Zhu, A. Lambertz, M. Jankovec, M. Topič, D. R. McCamey, S. Bremner, Z. Hameiri, K. Ding, D. Mckenzie, J. Zheng and A. Ho-Baillie, *Adv. Energy Mater.*, 2024, **14**, 2401029.